

ALMA-IMF XVII - Census and lifetime of high-mass prestellar cores in 14 massive protoclusters

M. Valeille-Manet¹, S. Bontemps¹, T. Csengeri¹, T. Nony^{2,3}, F. Motte⁴, A. M. Stutz^{5,17}, A. Gusdorf^{6,7}, A. Ginsburg⁸, R. Galván-Madrid², P. Sanhueza^{12,13}, M. Bonfand⁹, N. Brouillet¹, P. Dell'Ova^{6,7}, F. Louvet⁴, N. Cunningham^{4,10}, M. Fernández-López¹¹, F. Herpin¹, F. Wyrowski¹⁵, R. H. Álvarez-Gutiérrez⁵, M. Armante^{6,7}, A. E. Guzmán¹⁴, N. Kessler¹, A. Koley⁵, J. Salinas⁵, T. Yoo⁸, L. Bronfman¹⁶, and N. Le Nestour⁴

(Affiliations can be found after the references)

Received ...; accepted ...

ABSTRACT

Context. High-mass prestellar cores are extremely rare. Indeed, the search for such objects has until recently been hampered by small sample sizes, leading to large ambiguities in their lifetimes and hence the conditions in the cores in which high mass stars ($\geq 8 M_{\odot}$) form.

Aims. Here we leverage the large sample (~ 580 cores) detected in the ALMA-IMF survey to identify both protostellar and prestellar cores to estimate their relative lifetimes.

Methods. We use CO and SiO outflows to identify protostellar cores. We present a new automated method based on aperture line emission and background subtraction to systematically detect outflows associated with each of the 141 most massive cores. Massive cores which are not driving an outflow in either tracer are identified as prestellar. After careful scrutiny of the sample, we derive statistical lifetime estimates for the prestellar phase.

Results. Our automated method allows for efficient detection of CO and SiO outflows and has a similar performance efficiency as more cumbersome classical techniques. We identify 30 likely prestellar cores with $M \geq 8 M_{\odot}$, of which 12 have core masses $M \geq 16 M_{\odot}$. The latter contains the best candidates for high-mass star precursors. Moreover, most of these 12 are located inside the crowded central regions of the protoclusters, where most high-mass stars are expected to form. Using the relative ratios of prestellar to protostellar cores, and assuming a high-mass protostellar lifetime of 300 kyr, we derive a prestellar core lifetime of 120 kyr to 240 kyr for cores with masses $8 M_{\odot} < M < 16 M_{\odot}$. For $30 M_{\odot} < M < 55 M_{\odot}$, lifetimes range from 50 kyr to 100 kyr. The spread in timescales reflects different assumptions for scenarios for the mass reservoir evolution. These timescales are remarkably long compared to the 4 kyr to 15 kyr free-fall time of the cores. Hence, we suggest that high mass cores live ~ 10 to 30 free-fall times, with a tentative trend of a slight decrease with core mass. Such large ratios suggest that the collapse of massive cores is slowed down by non-thermal support of turbulent, magnetic or rotational origin at or below the observed scale.

Key words. stars: formation – stars: massive – stars: prestellar cores – stars: protostellar cores – ISM: outflows – ISM: clouds

1. Introduction

Understanding star formation strongly relies on unveiling the youngest stages of the evolution from molecular gas to young stars, i.e. the stages of the so-called protostars and pre-collapse or prestellar cores (e.g. Lada & Adams 1992; Andre et al. 2000 and references therein). These stages still carry the imprint of the physical properties at the onset of collapse and of the prevailing physical processes leading to the birth of a new star. For low-mass star formation, a fairly good census of all protostars and prestellar cores has been obtained with a series of infrared (IR) space telescopes, such as IRAS, ISO, Spitzer and Herschel leading to a view with a sequence of different observational stages led by clear physical processes.

Low-mass ($M < 8 M_{\odot}$) prestellar cores (hereafter PSCs) are believed to originate from quasi-static contractions of dense cores and clumps, well described by Bonnor-Ebert spheres, and leading to a gravitational collapse when gravity cannot be contained by the other supports, i.e. thermal, magnetic and turbulent pressures. In nearby molecular clouds, the properties of low-mass PSCs have been widely studied leading to a picture, namely the gravo-turbulent scenario (Padoan & Nordlund 2002), of a probable slow contraction of low density clump to high density cores over ~ 1 Myr (e.g. Jessop & Ward-Thompson 2000; Könyves et al. 2015). The typical thermal Jeans masses are also

found to correspond well to the stellar masses suggesting no additional support to thermal pressure is required to account for low-mass star masses.

In contrast the steps to form high-mass stars ($M > 8 M_{\odot}$) are much less understood. From the observational point of view this is due to the rarity of high-mass stars and the need to search for high-mass protostellar objects at large galactic distances (typically at a distance $d > 2$ kpc; Motte et al. 2018a). From the theoretical point of view, the modeling and simulations have difficulties in accounting for the full complexity of the required physics to explain the highest stellar masses, which certainly have to involve magnetic fields, turbulence and radiative energy at the same time and over decades of different scales in molecular clouds (e.g. Tan et al. 2014; Stutz & Gould 2016; Commerçon et al. 2022). Low-mass PSCs are easy to study and can be convincingly seen as the reservoir of mass to form stars (Motte et al. 1998; Launhardt et al. 2013; Könyves et al. 2015; Furlan et al. 2016) possibly formed by thermal Jeans instability in dense filaments and clumps, following the so-called core-fed scenario. In contrast, the reservoirs to form high-mass stars are much elusive and seem too massive to be explained by simple thermal Jeans fragmentation, certainly requiring magnetic and turbulent supports to keep possible the core-fed scenario. Continuously driven turbulence could increase the local Jeans masses enough

to explain high-mass reservoirs (McKee & Tan 2003). The global gravitational potential well of dense clumps (> 0.1 pc scale) could also lead to a competition for accretion from the large infall rates (Bonnell et al. 2001). The reservoir of mass to form high-mass stars could therefore mostly reside at clump scales with powerful convergence of gas down to protostellar scales in a so-called clump-fed scenario (Peretto et al. 2013; Csengeri et al. 2011; Duarte-Cabral et al. 2013; Peretto et al. 2020). It is unclear which exact physical processes are regulating or dominating the evolution of these massive cradles, and at which scale(s) a fragmentation process might yield small scale concentrations of mass that we would call "cores". Hence it remains unclear if high mass reservoirs can be pinpointed observationally as well-identified objects distinct from their surroundings (Motte et al. 2007; Tigé et al. 2017; Sanhueza et al. 2019; Morii et al. 2023).

Observationally the protoclusters are very dynamical in nature (Schneider et al. 2010; Peretto et al. 2013; Avison et al. 2021; Álvarez-Gutiérrez et al. 2024) and the dense high-mass clumps do not have the required level of turbulence to explain high-mass Jeans fragmentation (e.g. Csengeri et al. 2011). In order to explain the very rare occurrence of high-mass PSCs, Motte et al. (2018a) proposed a scenario in which protostellar cores and their parental clumps simultaneously grow in mass and accrete gas from their surroundings without any high-mass reservoir formed at early stage. The top-heavy core mass functions recently observed in the ALMA-IMF protoclusters (Motte et al. 2018b; Pouteau et al. 2022; Louvet et al. 2024) and its proposed evolution (Pouteau et al. 2023; Nony et al. 2023; Armante et al. 2024) could reflect this effect of progressive increase of core mass from the prestellar to the protostellar phase.

To understand the precise origin of high-mass stars, it is most vital to find very good examples of high-mass PSCs, and to study their physical properties. Such high-mass PSCs are, however, extremely rare as recognised early on by Motte et al. (2007) (see also Motte et al. 2018a for a review). So far only a few candidates for high mass prestellar cores have been found as compact cores that are both massive enough (at least above $16 M_{\odot}$) and without any outflow detection (i.e., likely tracing no protostellar activity, see below):

- CygX-N53-MM2 discovered in Duarte-Cabral et al. (2013) among nine other high-mass protostellar cores which does not show any strong sign of CO outflow but which is also situated on the side of a strong protostellar outflow from the nearby CygX-N53-MM1 protostellar core.
- G11.11-P6-SMA1 found in Wang et al. (2014) which is relieved of any outflow emission.
- W43-MM1 #6 discovered in Nony et al. (2018) which does not drive any strong outflow (it is close to a strong outflow driving high-mass protostar W43-MM1 #3) but has an interesting and unusual weak emission of complex organic molecules pointing to the presence of some warm gas inside it (between 20 and 90K; Molet et al. 2019).
- C2c1a in the Dragon cloud from Barnes et al. (2023) which is a core not driving any CO outflow but which might not be massive enough to be in the high mass regime. The relatively high-mass in Barnes et al. (2023) is due to an adopted very low temperature close to 9 K (from NH_3 gas temperature estimate) and a favorable dust opacity (see Sect. 5.3).

Some additional candidates in the past have been discarded since then: cores G11.92-0.61-MM2 of Cyganowski et al. (2014) and C1S of Tan et al. (2013) have been found to be protostellar in nature after follow up observations (Cyganowski et al. 2022 and

Tan et al. 2016 respectively). Some recent studies have searched for high-mass prestellar cores but without success most probably due to low statistics in the sample of high-mass cores (e.g. Louvet et al. 2019 and Morii et al. 2023 for the ALMA program ASHES). It is thus vital to observe some more significant samples of high-mass PSCs.

ALMA-IMF is the largest ALMA survey for high-mass protostellar objects in the relatively nearby high-mass protoclusters of the Galaxy (see Motte et al. 2022 for an overview). As suggested by Sanhueza et al. (2019), if high-mass prestellar cores exist they are most likely to be found in more massive and possibly more evolved environments than clumps in so-called IR Dark Clouds (IRDC). Xu et al. (2024) also observed that starless cores become more massive in evolved clumps such as protoclusters. ALMA-IMF survey allows us thus for the first time to search for high-mass prestellar cores in such environments with unprecedented statistics.

At disk and protostar scale (few hundreds of au, see e.g. Commerçon et al. 2022), there is evidence that low and high-mass star accretion and ejection rely on the same mechanism of the magneto-centrifugal accretion-ejection process (Blandford & Payne 1982; Ferreira et al. 2006) with a magnetic regulation of the angular momentum in the inner parts of the accretion disk (see Matsushita et al. 2017; Kölligan & Kuiper 2018; Csengeri et al. 2018; Olguin et al. 2023 for high-mass protostars). Accretion onto protostars is possible only if angular momentum in excess is driven away by ejecting part of the accretion flow through a magnetised jet and wind in the polar directions. Ejection of angular momentum allows the main accretion flows to spiral down onto the inner protostar in the equatorial plane. Since protostars are embedded inside their collapsing envelope and in surrounding dense clumps and filaments, jets and winds have to strongly interact with the surroundings. These interactions lead to a large amount of entrained gas in a roughly momentum conserved manner easily seen in CO line wings since CO is the most abundant observable species in cold dense gas. CO outflows are thus the best tracers of accretion for protostellar objects of all masses. This strong link between CO outflows and accretion onto protostars was first recognized observationally by Bontemps et al. (1996) for low-mass protostars. In addition to CO, SiO is a great tracer of shocks (see e.g. GUSDORF et al. 2008) and can help to identify outflows especially in very crowded regions where the confusion of CO can be important. These outflows can therefore be used to recognize accretion in cold cores to differentiate between prestellar cores (potential infall or slow contraction but no central accretion on a protostar) and protostellar objects (accretion on the central protostar). Here we use the CO and SiO outflow diagnostics as a signpost of protostellar accretion in the ALMA-IMF cores. Despite the above described arguments pointing to the expected and observed strong link between the protostellar status defined as actively accreting stellar embryos and the detection of CO/SiO outflows, we may consider possibilities that some truly protostellar cores may lack detectable such outflows. We discuss these possibilities in Sect. 7.8.

After presenting the dataset in Sect. 2, we describe the CO and SiO outflow automated method to detect in a homogeneous way the outflows associated with the detected protostars of the ALMA-IMF fields in Sect. 3. We then show that, as expected, most of the detected cores are driving outflows (Sect. 4). However, we identify a number of clearly young high-mass cores without outflow, making them excellent candidates to be high-mass PSCs. These sources are described in Sect. 4. We define high-mass PSCs and present the robust sample of high-mass PSC candidates in Sect. 5. Their rarity is discussed in Sect. 6. In

Sect. 7, we then discuss this result in the context of the expected evolution of a high-mass protostar, deriving a strongly improved lifetime for PSCs for the high-mass regime which can be used to discuss first implications on the way high-mass stars may form.

2. Observations and data reduction

The data used for this paper are part of the large program ALMA-IMF¹ (#2017.1.01355.L, PIs: Motte, Ginsburg, Louvet, Sanhueza), which targets 15 massive protoclusters located at distances from 2 to 5.5 kpc. Motte et al. (2022) (ALMA-IMF Paper I) describe in detail the ALMA-IMF large program, its objectives and first results. In short, the targets were selected from the ATLASGAL survey carried out with the APEX telescope (Csengeri et al. 2014), from which Csengeri et al. (2017) identified the 200 sub-millimeter brightest star forming clumps covering different evolutionary stages. We used the Atacama Large Millimeter/submillimeter Array (ALMA) interferometer to image these regions in two frequency bands : Band 3 (B3; ~91-106 GHz) and Band 6 (B6; ~216-234 GHz) as described in Motte et al. (2022). Table 1 lists the main characteristics of each protocluster, such as their name and central positions, V_{LSR} , distance from the Sun, evolutionary stage from Motte et al. (2022), the synthesized beam of the continuum maps in arc seconds, and the corresponding physical scale in astronomical unit (au), as well as the synthesized beam in arc seconds of the line datacubes used.

Details of the data reduction process is described in Ginsburg et al. (2022) (ALMA-IMF Paper II) that presents the continuum maps at 1.3 mm and 3 mm for the 15 protoclusters. We use here the catalogs of continuum sources from Louvet et al. (2024) that were obtained with the source extraction algorithm getsf (Men'shchikov 2021). We use the source catalogs extracted from the cleanest continuum maps smoothed to a common physical resolution of 2700 au that corresponds to the poorest resolution of the sample. Sources potentially contaminated by free-free emission were removed from this catalog based on spectral index estimations (see Galván-Madrid et al. sub. and Louvet et al. 2024 for details). In short, the cleanest continuum maps are obtained by using only line free channels to estimate the continuum. The smoothing was done in order to obtain the same spatial resolution of 2700 au in Band 6 for all the targeted regions. This provides us a sample with a total of 580 gravitationally bound cores on the same linear scale (cores are considered as bounded for $M_{\text{BE}}/M_{\text{core}} < 2$ in Louvet et al. 2024). We identify the sources based on the core name from Louvet et al. (2024), and the core numbering per each protocluster.

We also make use of the spectral line datacubes from ALMA-IMF, in particular the CO (J=2–1), the SiO (J=5–4), and the DCN (J=3–2) transitions. While the CO and SiO lines are used to trace protostellar outflows, DCN is used to estimate a V_{LSR} for each source individually, similarly as done by Cunningham et al. (2023). The data reduction of the line cubes is presented in detail in Cunningham et al. (2023). We use the spectral line datacubes with the "JvM" correction (Jorsater & van Moorsel 1995) of the residual flux scale. The continuum is subtracted from the datacubes using the STATCONT procedure (Sánchez-Monge et al. 2018). The SiO (J=5–4) line is covered in our Band 6 setup and spectral window 1 together with the DCN (J=3–2) line. The CO (J=2–1) transition is also in our Band 6 setup and the spectral window 5. We use data only from the ALMA 12 m array configurations. The beam sizes of the

linecubes used here are comparable to the continuum ones with a difference up to 35% depending on the region. The synthesized beam sizes and sensitivity of the linecubes is described in Cunningham et al. (2023). We summarize the observing parameters for the spectral line datacubes used here in Table 2.

As described in Cunningham et al. (2023), due to bright and extended CO emission in some regions, we masked channels around their V_{LSR} to avoid cleaning divergences in this spectral window. The G351.77 protocluster still presents strong sidelobes at high velocities in the CO datacube, preventing us from studying the protostellar outflows in this region, overall leaving us with the remaining 14 protoclusters of ALMA-IMF.

Nony et al. (2020) and Nony et al. (2023) used the same CO transition as we use here to distinguish pre- and protostellar cores in the W43 protoclusters. Towner et al. (2024) used the SiO (J=5–4) transition of ALMA-IMF to search for shocked gas potentially associated with outflows although with no attempt to associate them to their driving sources. Armante et al. (2024) studied the evolved protocluster, G012.80, from ALMA-IMF and they also classified pre- and protostellar cores using the same CO and SiO transitions. A comparison of these studies and our work is presented in Sect. 4.3.

3. A systematic method to detect proto-stellar outflows

Our goal here is to classify cores from ALMA-IMF into protostellar or prestellar cores. To do so, we make use of the CO (J=2–1) and SiO (J=5–4) lines to perform a systematic search for high-velocity emission. Such emission is likely to correspond to directly ejected and gas entrained by ejected material due to protostellar accretion, and can be thus efficiently used to identify protostellar sources.

3.1. Detection of high velocity excess emission: On-Off spectra

We develop an automatic method to systematically identify protostellar outflows by looking for high-velocity excess emission in the CO and SiO spectra. For this purpose, we use the ellipse corresponding to the extracted continuum source, where the major and minor axes of the ellipse are defined as the FWHM of the fitted 2D Gaussian major and minor axes. We then take the mean of the spectra within this region. We use this spectrum as an On source measurement, and compute an Off source measurement, using an annulus between 2.5 and 3.5 × the FWHM of the on-source ellipse. In this annulus we exclude pixels belonging to another continuum source. See example in Fig. 1 and in App. A. With this method, our aim is to measure emission from the ejected and entrained gas from the relatively close vicinity of the source itself. By subtracting the Off measurement from the On, we can search for high-velocity residual emission in the immediate vicinity of the protostellar core, as first introduced by Bontemps et al. (1996) and explained in detail in Duarte-Cabral et al. (2013). This method relies on the principle that any ejection events should accelerate a significant amount of gas inside the core itself so that an excess of outflowing gas on the core (On spectrum) should be detected compared to the average surrounding (Off spectrum).

We compute this differential spectra for all sources with $M > 8 M_{\odot}$ where we used a conservative temperature estimate of 20 K (see Sect. 4.1) from the catalog of Louvet et al. (2024).

¹ <https://www.almaimf.com> : ALMA transforms our view of the origin of stellar masses

Table 1. Overview of the ALMA-IMF protocluster clouds, their evolutionary stage and angular resolution.

Protocluster cloud name ¹	RA ¹ [ICRS (J2000)]	Dec ¹	V _{LSR} ² [km s ⁻¹]	d ¹ [kpc]	M _{cloud} ¹ × 10 ³ M _⊙	Evolutionary stage ³	ν _{1.3mm} ⁴ [GHz]	θ ⁵ ["]	θ _{spw1} ^{ave 6} ["]	θ _{spw5} ^{ave 7} ["]
G008.67	18:06:21.12	-21:37:16.7	+35.0	3.4	3.1	I	228.732	0.79	0.80	0.76
G010.62	18:10:28.84	-19:55:48.3	-2.7	4.95	6.7	E	229.268	0.55	0.60	0.54
G012.80	18:14:13.37	-17:55:45.2	+36.1	2.4	4.6	E	229.080	1.13	1.07	1.00
G327.29	15:53:08.13	-54:37:08.6	-45.0	2.5	5.1	Y	229.507	1.08	0.78	0.73
G328.25	15:57:59.68	-53:58:00.2	-43.4	2.5	2.5	Y	227.575	1.08	0.66	0.61
G333.60	16:22:09.36	-50:05:58.9	-47.8	4.2	12.0	E	229.062	0.64	0.71	0.65
G337.92	16:41:10.62	-47:08:02.9	-39.6	2.7	2.5	Y	227.503	1.00	0.73	0.68
G338.93	16:40:34.42	-45:41:40.6	-61.1	3.9	7.1	Y	229.226	0.69	0.72	0.67
G351.77	17:26:42.62	-36:09:20.5	-3.9	2.0	2.5	I	227.991	1.35	0.95	0.88
G353.41	17:30:26.28	-34:41:49.7	-17.6	2.0	2.5	I	229.431	1.35	0.97	0.90
W43-MM1	18:47:47.00	-01:54:26.0	+97.4	5.5	13.4	Y	229.680	0.49	0.55	0.50
W43-MM2	18:47:36.61	-02:00:51.1	+91.0	5.5	11.6	Y	227.597	0.49	0.56	0.56
W43-MM3	18:47:41.46	-02:00:27.6	+93.0	5.5	5.2	I	228.931	0.49	0.61	0.58
W51-E	19:23:44.18	+14:30:29.5	+55.2	5.4	32.7	I	228.918	0.50	0.4	0.46
W51-IRS2	19:23:39.81	+14:31:03.5	+61.4	5.4	20.6	E	228.530	0.50	0.62	0.55

¹ Protocluster name, central position used for the ALMA-IMF observations. Distances and masses are taken from Motte et al. (2022) and references therein.

² Velocity relative to the local standard of rest extracted from Cunningham et al. (2023).

³ Classification of the ALMA-IMF protocluster clouds: Young (Y), Intermediate (I), and Evolved (E) (see Section 4.1 by Motte et al. (2022)).

⁴ Central frequencies of observations in Band 6 extracted from Louvet et al. (2024)

⁵ Angular resolution in Band 6 extracted from Louvet et al. (2024)

⁶ Angular resolution in spw1 Band 6 (217.150 GHz, which includes the SiO(5–4) and DCN(3–2) lines) define as $\theta_{ave} = \sqrt{\theta_{maj} \times \theta_{min}}$ and extracted from Cunningham et al. (2023)

⁷ Angular resolution in spw5 Band 6 (230.530 GHz, which includes the CO(2–1) line) extracted from Cunningham et al. (2023)

Table 2. Spectral lines used and their spectral resolution.

Line	Frequency [GHz]	ALMA Band	Spectral window	Cube bandwidth [MHz]	Resolution [kHz] [km s ⁻¹]
SiO(5-4)	217.105	B6	SPW 1	234	244 0.34
DCN(3-2)	217.238	B6	SPW 1	234	244 0.34
CO(2-1)	230.538	B6	SPW 5	974	468 1.27

ALMA-IMF targets several of the most active star forming regions of the Galaxy, and therefore we have several complex areas where many cores and outflows overlap. Therefore, to complement our analysis based on differential spectra, we also produced maps of molecular outflows using moment zero maps to study their spatial distribution, as presented in Sect. 3.5.

We show in Fig. 1 the cores #3, #27 and #30 of the W43-MM2 region as an example. The CO(2–1) On-Off spectrum of core #3 shows an excess emission at velocities offset from the source V_{LSR} corresponding to line wings. This example demonstrates that core #3 exhibits an excess in high-velocity emission up to ±75 km s⁻¹, corresponding to outflowing and ejected gas, and thus can be classified as a protostellar core. On the opposite, the On-Off spectra of cores #27 and #30 do not show any sign of outflow. The SiO(5–4) spectra of these three cores are shown in App. A. From now on all the SiO spectra shown are smoothed by a factor of two in spectral resolution purely for visual clarity, but the analysis has been carried out using the full spectral resolution. The corresponding spectra of each PSC candidate identified in this paper are shown in App. E.

3.2. Noise estimates

The noise distribution of the ALMA-IMF datacubes exhibits some spatial and spectral variations. Spatial variations of the noise distribution for other transitions in the ALMA-IMF has been discussed for example in Bonfand et al. (2024). The CO(J=2–1) datacube is particular in this context, because channels close to the source V_{LSR} exhibit a higher noise mostly due to side-lobes from missing short spacings.

In order to be able to estimate the significance of CO and SiO emission individually in each velocity channels we have estimated the emission noise using the spatial variation of emission in both for the CO and the SiO lines. For that, we measured the dispersion of the emission for each channel among randomly located On-Off positions. To do so, we first mask all the pixels from the cores of the ALMA-IMF catalog and the noisy edges of the datacubes. We then compute the On-Off spectrum for randomly placed 150 sources with convolved FWHM sizes between 3000 and 5500 au, a random position angle and eccentricity between 0 and 0.8 for each (see Fig. B.1 in App. B). For each channel, we then extract the mean and standard deviation among the 150 On-Off positions. We use this standard deviation as the noise in each channel (i.e. RMS per channel, see Fig. 2). Placing 150

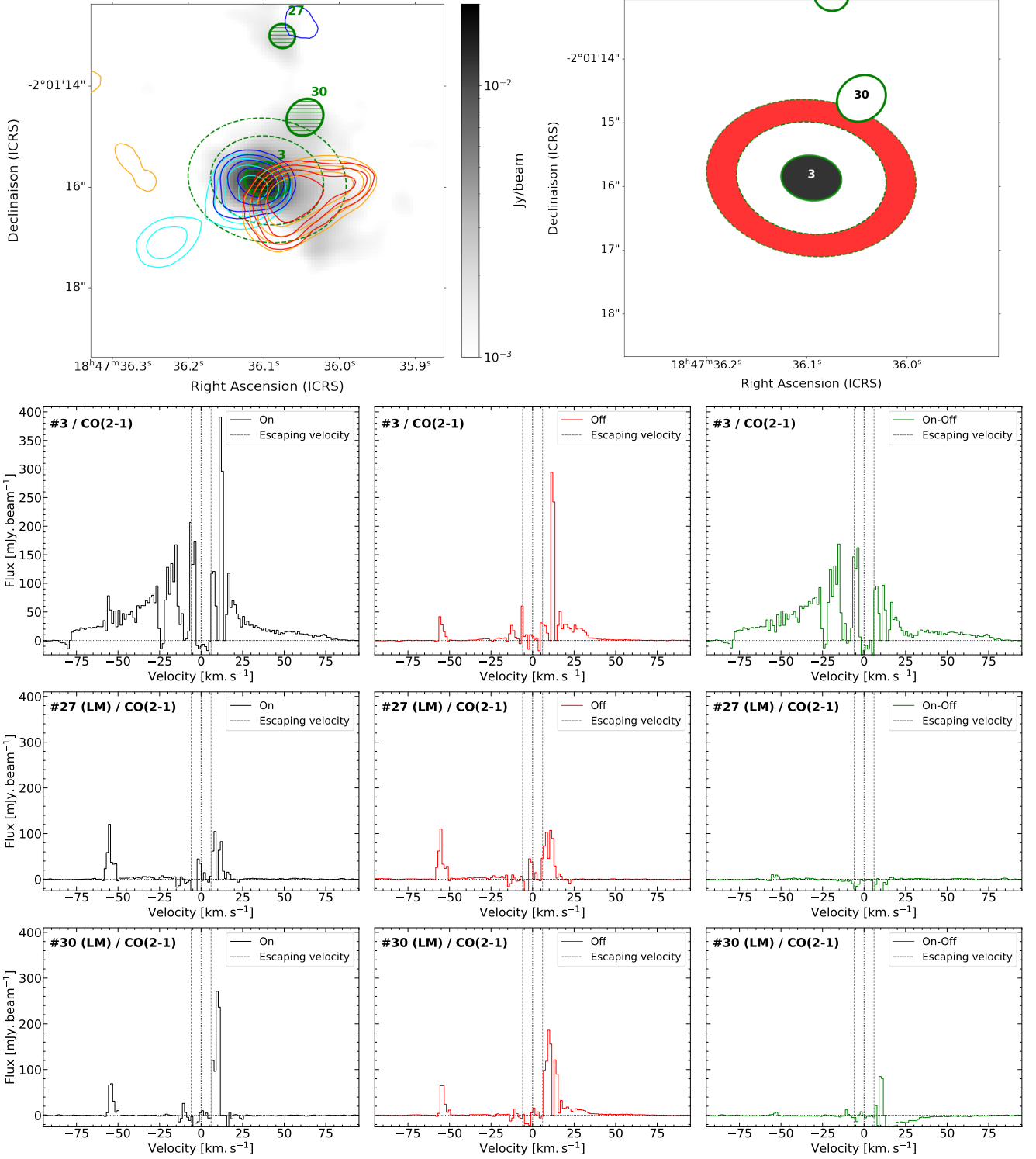


Fig. 1. Overview of the outflow detection procedure using the On-Off spectra presented in Sect. 3.1. **Top Left:** Zoom on the continuum core #3 overlaid on the 1.3mm dust continuum map of W43-MM2 (in grey scale). The green ellipses correspond to the FWHM of the extracted source sizes to the continuum emission by getsf. Colored CO (2-1) contours are 10, 20, 40 and 80 in units of σ , with $\sigma = 14.3, 12.6, 10.8, 9.0$ mJy beam⁻¹ km s⁻¹ for cyan, blue, orange and red contours respectively. The corresponding velocity ranges are ± 15 –23 km s⁻¹ for cyan and orange, -31 –42 km s⁻¹ for blue and $+31$ –50 km s⁻¹ for red. These velocities have been centered the V_{LSR} of the core (see text). **Top Right:** Example of the On (black ellipse) and Off (red annulus) spectra computation used to estimate the core-averaged background-subtracted spectra, here for core #3. **Bottom :** Resulting CO(2-1) On (black), Off (red), and On-Off (green) spectra for cores #3, #27 and #30. Core #3 shows clear line wings, representative of its bipolar outflow that can be analysed in its On-Off spectra. The black and red spectra are computed in the black ellipse and red annulus of the top right panel. The grey dashed lines correspond to the escaping velocity (i.e. the velocity to escape the gravitational orbit) presented in Sect. 3.4. The spectra of cores #27 and #30 are extracted with the same method. These core do not show any sign of outflow, as expected for core #30 when looking at the map in the top panel, while the On-Off spectrum of core #27 do not present any blue line wing.

On-Off random locations allows to account for the spatial variations of the datacube, while doing it for every channel account for the spectral variations.

As an example, we show the noise estimation in Fig. 2 for the W43-MM2 region for two channels (top panel, one with bright and one with weak mean CO emission), and then the noise spectra extracted for both CO and SiO datacubes (middle and bottom panels). The noise spectrum recovers well the fluctuations of emission in the cube (shown on the right y-axis) when we compare the noise over the channels with the mean spectrum of the original datacube (i.e. without masked areas). In Fig. 2 we show our velocity axis centered on the V_{LSR} of the region. We find that the noise is increasing where the CO emission is bright, i.e. close to the source V_{LSR} , and between 25 and 55 km s^{-1} for W43-MM2 where there is a significant foreground CO emission (foreground cloud on the line of sight; see [Nony et al. 2023](#), [Nguyen-Luong et al. 2017](#)). The noise is globally decreasing for velocities largely offsetted from CO emission at the V_{LSR} , confirming the interest to estimate such a precise noise variation along the velocity channels. In Fig. 2, bottom panel, we see that the typical noise spectrum (for W43-MM2) for SiO is much more uniform than for CO. The mean and standard deviation of the derived noise levels in each of the 14 ALMA-IMF regions, for B6 spw1 and B6 spw5, are shown in Fig. B.2 in App. B.

3.3. V_{LSR} estimation of dust cores

In order to define the velocity ranges corresponding to our definition of high-velocity emission, we need precise and systematic estimates of the V_{LSR} of each dust core. As shown in [Cunningham et al. \(2023\)](#), the typical dispersion of the V_{LSR} for individual sources within our protoclusters can be as high as 12 km s^{-1} , meaning that the determination of the V_{LSR} of individual cores is important to well define the velocity range sufficiently offset from the source V_{LSR} .

Using the same approach as in [Cunningham et al. \(2023\)](#), we perform here an independent estimate of the V_{LSR} of each dense core using the DCN ($J=3-2$) transition. We extract the On-Off spectrum of the DCN line towards each core in the same fashion as discussed above, and as in [Cunningham et al. \(2023\)](#), then fit a single component 1D Gaussian. We consider a line detected if the fit has a FWHM larger than the spectral resolution and the measured area is greater than 5σ . We estimate σ by using the noise spectrum presented in Fig. 2 on the channels of the fit area. For a discussion on the noise estimation we refer to Sect. 3.2. If these criteria are not met, we perform the same fitting using the On spectrum. Finally, if none of the fits are good, we use the mean V_{LSR} of each region, as the value for the individual core, estimated with the DCN measurements on the cores where the fits can be performed. The DCN ($J=3-2$) spectra and the respective fit for every prestellar core candidate is provided in App. E. Our V_{LSR} estimates are in agreement with the estimates of [Cunningham et al. \(2023\)](#) for sources that are classified as exhibiting a single component DCN emission. Compared to the analysis shown in [Cunningham et al. \(2023\)](#), here we go a step further by fitting also the On spectra. From the sample of 141 cores presented in Sect. 4.4, we get 136 individual V_{LSR} , among which 116 are also in [Cunningham et al. \(2023\)](#), from the fit of 106 On-Off and 30 On spectra, while the region V_{LSR} is used for the 5 cores without a good DCN detection.

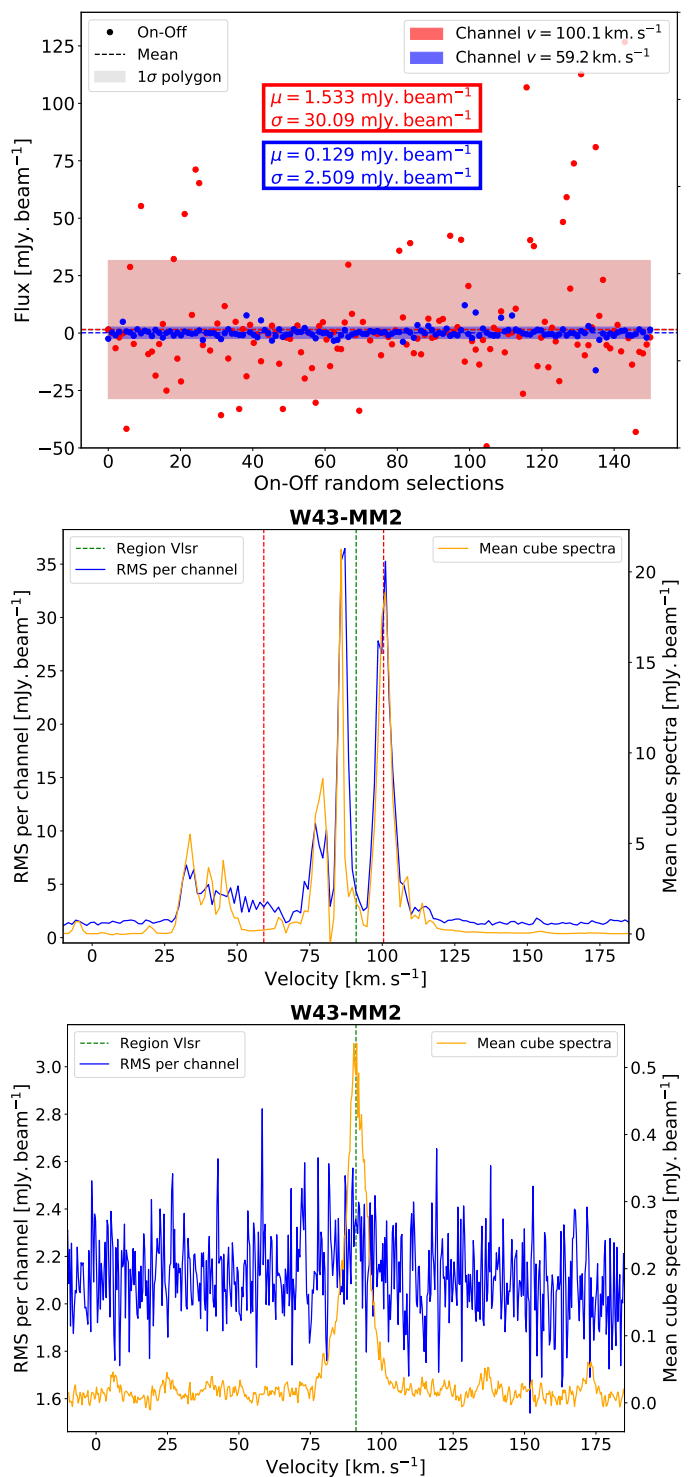


Fig. 2. Top : Dispersion of the 150 On-Off random selections fluxes in the CO datacube of the region W43-MM2 for channels at velocities of 59.2 km s^{-1} and 100.1 km s^{-1} . The mean (μ) and standard deviation (σ), which is assumed for the noise in a respective channel, are indicated in the panel. **Middle :** Noise spectra of the CO datacube of the region W43-MM2 (in blue, left y axis) overlaid with its mean cube spectra (in orange, right y axis). The mean cube spectra is computed by averaging the fluxes of all the pixels (except the ones of the edges) at every channel. The green dotted line is centered on the V_{LSR} of the region. The two channels represented in the top panel are spotted with the red dashed lines. **Bottom :** Same as above for the SiO datacube.

3.4. Identification of outflow emission

From our analysis above, we obtain a spectrum representing the CO and SiO emission for each dust core. As a next step we analyse these spectra to search for emission at high velocities compared to the source V_{LSR} . We define the velocity range to search for gas that can escape the core gravitational potential by computing the escape velocity for a core mass of $M = 50 M_{\odot}$ and a radius r of 3000 au as $V_{\text{esc}} = \sqrt{\frac{2GM}{r}}$, where G is the gravitational constant. We obtain an escape velocity of 5.4 km s^{-1} which is then used to define the velocity limits to identify outflowing gas. Since the CO emission from the protocluster is usually broader than this limit we actually adopt a slightly larger value of $> \pm 6 \text{ km s}^{-1}$ around the V_{LSR} to search for possible significant outflowing gas emission. This threshold in velocity offset is used systematically for all cores². We consider emission as significant in two steps: if at least two consecutive channels exceed 5σ (sigma computed with the RMS per channel presented in Sect. 3.2), then the emission is directly considered as significant; if this first criteria is not reached but the sum of the emission in five consecutive channels or less exceed the 5σ threshold (sigma still computed with the RMS per channel, taking into account the variations per channel), it is also considered as significant emission. These criteria are considered for both CO and SiO lines, however significant emission in the high-velocity part in one of the two lines is considered sufficient to be considered as an outflow.

The method described above is the first step of our detection procedure. In the case of crowded regions, outflows from nearby protostars can deposit some momentum on the detected cores, therefore it is necessary to also visually check the spatial distribution of outflowing gas to support our systematic outflow detection method (see next section). For this we have also automatically produced moment zero maps of outflows in both CO and SiO.

3.5. Molecular outflow maps

To complement the On-Off method presented above, we compute moment zero maps of the blue- and red-shifted wings of the CO (2-1) and SiO (5-4) lines, that are then compared to the continuum map and the position of continuum cores. The visual inspection of maps of high velocity lobes is the usual method to recognise outflows and their driving sources which are placed at the center of the usual bipolar configuration of molecular outflows (see e.g. Armante et al. 2024, Nony et al. 2023, Avison et al. 2021, Nony et al. 2020, Li et al. 2020, Cunningham et al. 2016, Duarte-Cabral et al. 2013). Here the velocity ranges of integration are chosen as the best compromise to cover the full CO and SiO emission in the line wings. We try to avoid a too strong contamination from the broad CO emission of the region, while keeping the same velocity ranges (compared to V_{LSR}) for the 14 ALMA-IMF protoclusters. We then choose as a reference to have low and high velocity contours at velocity offsets with respect to the V_{LSR} at $\pm 15\text{--}30 \text{ km s}^{-1}$ and $\pm 30\text{--}50 \text{ km s}^{-1}$ for CO, and $\pm 10\text{--}25 \text{ km s}^{-1}$ and $\pm 25\text{--}50 \text{ km s}^{-1}$ for SiO. These ranges can slightly change depending on the region to avoid some possible strong CO foreground or background cloud contamination. Figure 3 shows the example for the W43-MM2 region with the CO and SiO molecular outflow maps on the left

² The same threshold of 6 km s^{-1} has been adopted in order to stay systematic and for simplicity. For cores with lower masses than $50 M_{\odot}$, this velocity threshold could be smaller.

and right panel, respectively. Some CO contamination is, however, still present in the outflow map, shown by the north blue-shifted low-velocity emission (cyan contours) and the south-east blue-shifted high-velocity emission (blue contours). This emission is not collimated and not associated with a continuum core, therefore it is not considered as outflow emission. The CO and SiO outflow maps of each high-mass PSC candidate identified from this work (see Sect. 4.1 below) are presented in Appendix E with the corresponding velocity range plotted on the spectra and the characteristics for each map in the caption. The noise for each velocity range to represent the contours is obtained from the noise estimation presented in Sect. 3.2.

4. Results and analysis

4.1. High-mass cores in ALMA-IMF

We estimate the core masses using the classical formula modified to correct from optically thick emission as in Pouteau et al. (2022) (see their appendix B), which converts the integrated flux ($S_{1.3\text{mm}}^{\text{int}}$) and peak flux ($S_{1.3\text{mm}}^{\text{peak}}$) at 1.3 mm into a mass :

$$M_{\text{source}} = -\Omega_{\text{beam}}^{1.3\text{mm}} \frac{d^2}{\kappa_{1.3\text{mm}}} \frac{S_{1.3\text{mm}}^{\text{int}}}{S_{1.3\text{mm}}^{\text{peak}}} \ln \left(1 - \frac{S_{1.3\text{mm}}^{\text{peak}}}{\Omega_{\text{beam}}^{1.3\text{mm}} B(T_d, \nu)} \right) \quad (1)$$

where $\Omega_{\text{beam}}^{1.3\text{mm}}$ is the solid angle of the beam at 1.3mm, d is the distance between the region and the Sun, $\kappa_{1.3\text{mm}}$ is the dust opacity defined by $\kappa_{1.3\text{mm}} = 0.1(\nu/1000 \text{ GHz})^{\beta} \text{ cm}^2 \text{ g}^{-1}$ which encompasses a gas-to-dust ratio of 100, at the central frequency ν of the observations in the Band 6 of each region, with $\beta = 1.5$ chosen to be the same as in Louvet et al. (2024) and Pouteau et al. (2022), which is the typical opacity index for cold and dense gas at the core scale (Andre et al. 1993, Ossenkopf & Henning 1994). $B(T_d, \nu)$ is the Planck function at the frequency ν and dust temperature T_d .

To cover most of the potential precursors of high-mass stars, we perform the systematic outflow detection on all cores above $8 M_{\odot}$ using a dust temperature of 20 K. This temperature could be in practice lower for PSCs without internal source as the cooling times are short at such high densities (shorter than free-fall times for an isothermal collapse; see for instance Commerçon et al. 2022 and references therein), and could be as low as 10-15 K as observed in recent claims for high-mass PSCs such as in Mai et al. (2024), Barnes et al. (2023), Morii et al. (2023), or Sanhueza et al. (2017) in which they used NH_3 or rotational diagram of CH_3OH lines to derive gas temperatures. At a temperature of 15/10 K, our proposed threshold would then correspond to 12/16 M_{\odot} . A total of 141 cores were found above this threshold. The final adopted dust temperatures are further discussed object by object in Sect. 4.5 below.

4.2. Systematic detection of outflows

We use both the On-Off spectra (step 1) and the outflow lobe maps in CO and in SiO (step 2) described above in Sect. 3 to search for outflows associated with the 141 cores from ALMA-IMF with $M > 8 M_{\odot}$.

Our primary and first criterium to decide whether a core is driving an outflow is based on the detection of a significant emission in the high velocity ranges in CO and/or in SiO in the On-Off spectrum towards the core. As a second step then we use the outflow lobe maps to check whether a possible significant detection of an excess (compared to the surroundings as measured in

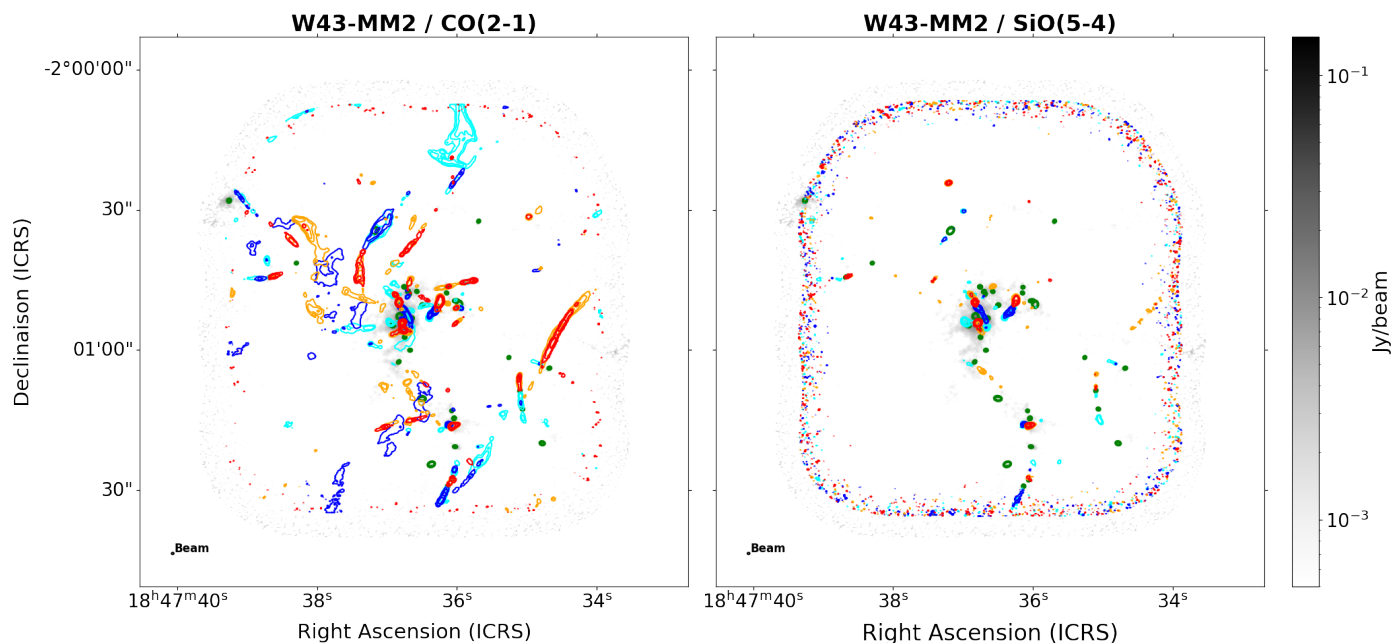


Fig. 3. CO (left) and SiO (right) molecular outflows map of the W43-MM2 region overlaid on the 1.3mm dust continuum map (in grey scale). The green ellipses represent the FWHM of the continuum cores convolved by the beam size. Moment 0 contours of the blue-shifted wings are overlaid on the continuum map at low velocity in cyan and high velocity in blue. Moment 0 contours of the red-shifted wings are overlaid on the continuum map at low velocity in orange and high velocity in red. CO and SiO contours are 10, 20, 40, and 80 in units of σ , with $\sigma = 18.9, 11.0, 18.1, 6.4$ mJy beam $^{-1}$ km s $^{-1}$ for CO, and $\sigma = 4.4, 5.7, 4.5, 5.7$ mJy beam $^{-1}$ km s $^{-1}$ for SiO, for cyan, blue, orange and red contours respectively. The corresponding velocity ranges are ± 15 – 30 km s $^{-1}$ and ± 30 – 45 km s $^{-1}$ for CO and ± 10 – 25 km s $^{-1}$ and ± 25 – 50 km s $^{-1}$ for SiO.

the Off spectrum) of outflowing gas towards the core could not be due to a nearby outflow (from another source). This would deposit some detectable momentum onto the targeted core. This happens often in the crowded regions like the ALMA-IMF central clumps. When such a clear nearby interacting outflow is present we consider to revise the On-Off result leading to a possible non detection of an outflow despite a significant excess on the source. This second criterion is slightly more subjective since it is based on the visual inspection of the maps but is necessary to reject clear cases of a significant influence of nearby outflows.

In practice to select potential prestellar core candidates not driving an outflow we adopt the following two steps:

- The CO and SiO spectra show no excess above 5σ in the blue- or red-shifted high-velocity ranges as defined in Sect. 3.5 ;
- If an excess is detected in the On-Off spectra onto the source, there is a nearby outflow driven by another source which convincingly explain this excess.

In Fig. 4 we show an example of a prestellar core and a prestellar source using both CO and SiO spectra and maps. These sources are representative of the simplest cases where there is no outflow confusion. The left panel shows the prestellar core #1 of the G328.25 region, known to be a hot core precursor (Csengeri et al. 2019; Bouscasse et al. 2022), where both the CO and SiO spectra show line wings representative of its bipolar outflow (e.g. Csengeri et al. 2018), clearly driven by the central source. The right panel confirms the prestellar nature of the core #6 of W43-MM1 as proposed by Nony et al. (2018). Neither the CO, nor the SiO spectra exhibit emission in the line wings, and no outflow is driven from the core shown in the CO and SiO maps.

As expected, a large number of the 141 targeted cores are found to drive outflows. However, 42 of these cores are found with no significant sign of outflowing activity, which are then

considered to be PSC candidates. The CO and SiO outflow maps of the 12 most massive of these 42 PSC candidates are displayed in Fig. 5. In the different panels of Fig. 5, centered on these 12 high-mass PSCs, we see a number of cores associated with outflow lobes qualifying them as protostellar cores. On the other hand, at the center of these maps we see each PSC candidate that we propose showing no sign of outflow driven by these cores.

We note that outflows mostly in the plane of the sky could be missed when searching for outflowing gas at velocities projected on the line of sight larger than 6 km s $^{-1}$. For a typical maximum, de-projected velocity of the outflow of 50 km s $^{-1}$ (see typical outflows in Fig. 5), and assuming uniform distributions of the opening angles of the outflow from 0 to 30° and of the inclination angles between 0 and 90° , we obtain a fraction of non detectable (above 6 km/s) outflows of 0.0175 (1.75 %). This fraction represents less than one missed outflow among the 42 PSC candidates. Even with more extreme values with the maximum velocity at 30 km s $^{-1}$ and the maximum opening at 20° the fraction of missed outflows stays relatively low at 7.35 %, leading to typically 3 (1) missed outflows among the 42 PSC candidates (12 HM PSC candidates) respectively.

Finally we note that in crowded regions, where the confusion between outflow lobes is large, at least in projection, the adopted methodology may result in some PSCs being miss-classified as protostellar cores. It is difficult to evaluate to which extent this happens but we argue that the On-Off approach is the only systematic and homogeneous way to identify the most probable driving sources.

4.3. Comparison with previous ALMA-IMF outflow results

Nony et al. (2020) and Nony et al. (2023) previously used the CO (J=2–1) outflow lobe maps to visually identify outflows in the W43-MM1, W43-MM2 and W43-MM3 regions. These works

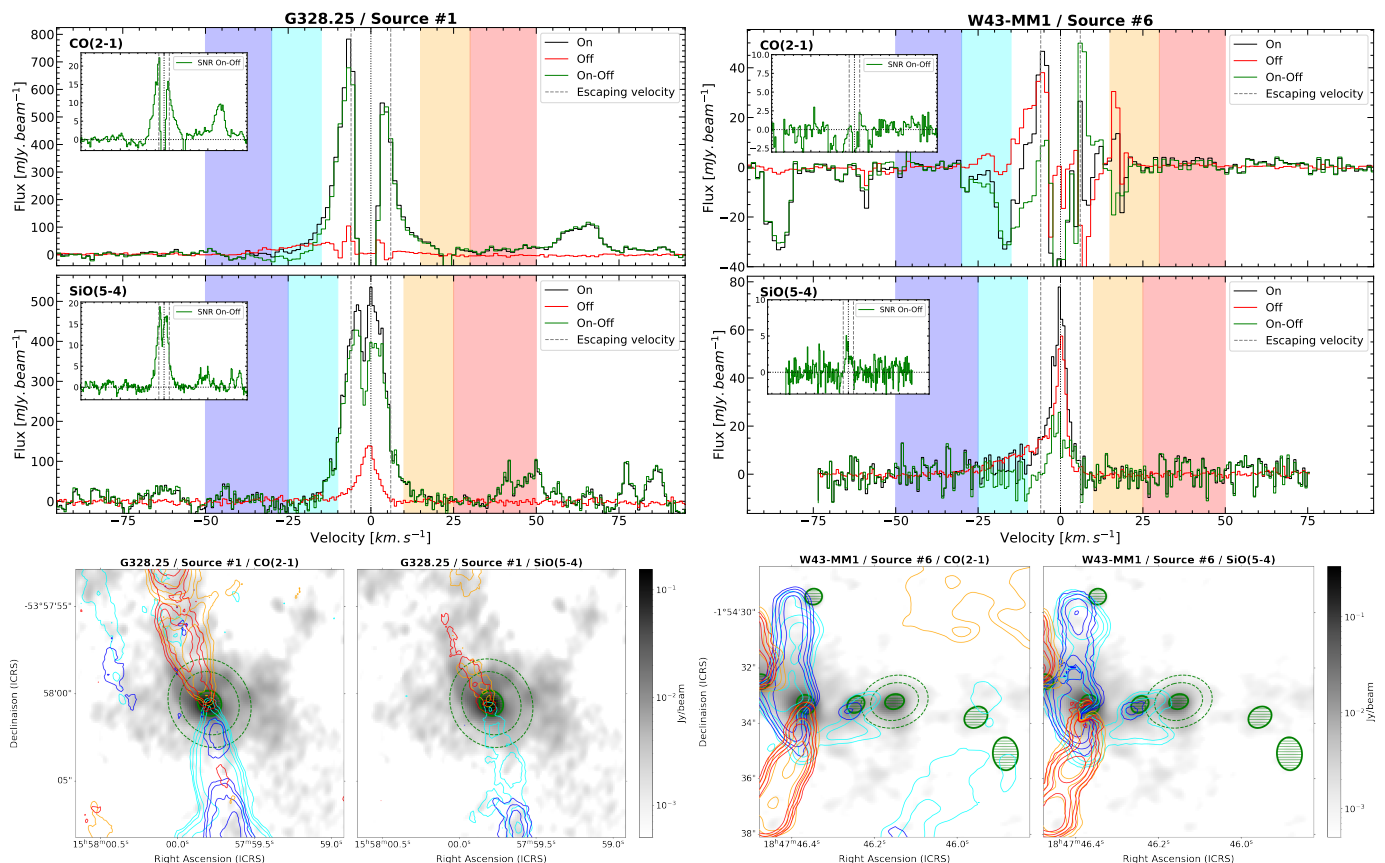


Fig. 4. **Top Left:** CO and SiO spectra of the protostellar source #1 of the G328.25 region. On, Off, and On-Off spectra are the black, red, and green spectra respectively. The small subplots on the top left of each spectra are the SNR for On and On-Off spectra, revealing the significant part of each one. The colored spaces on the spectra are the velocities ranges used to make molecular outflows maps. **Bottom Left:** Zoom on the #1 of the G328.25 region driving a bipolar outflow. Contours colors correspond to the same as in figure 3. CO and SiO contours are 5, 10, 20, and 40 in units of σ , with $\sigma = 60.1, 60.4, 61.9, 62.7$ mJy beam $^{-1}$ km s $^{-1}$ for CO, and $\sigma = 38.9, 49.0, 38.1, 49.6$ mJy beam $^{-1}$ km s $^{-1}$ for SiO, for cyan, blue, orange and red contours respectively. **Top Right:** Same as top left panel but for the prestellar source #6 of the W43-MM1 region. **Bottom Right:** Same as the bottom left panel but for the prestellar source #6 of the W43-MM1 region. CO and SiO contours are 10, 20, 40, and 80 in units of σ , with $\sigma = 32.6, 18.6, 49.5, 15.3$ mJy beam $^{-1}$ km s $^{-1}$ for CO, and $\sigma = 6.4, 7.4, 7.3, 7.2$ mJy beam $^{-1}$ km s $^{-1}$ for SiO, for cyan, blue, orange and red contours respectively.

were based on careful and relatively time consuming investigation of the outflow maps and cubes.

The comparison with our present results is therefore extremely interesting to validate the method since the data are the same (ALMA-IMF dataset). We see that our more automated method based on the On-Off spectra gives exactly the same identification of outflows for 26 protostellar common sources with Nony et al. (2020) and Nony et al. (2023). We see discrepancies in the identification of outflows for one core that we classify here as protostellar and for three out of 11 cores which we here consider as not driving any outflow. We classify W43-MM1 source #20³ as protostellar due to a detection in the red-shifted wing in the On-Off spectrum and its associated lobe, while Nony et al. (2020) classified it as prestellar. Among the three other sources, two (W43-MM1 #30 and W43-MM2 #9)⁴ do not have any significant emission at high velocities in their On-Off spectrum and their outflow maps show no sufficient evidence of association with the surrounding lobes to validate an outflow from these cores. W43-MM1 #30 was indeed labeled as tentative in Nony

et al. (2020). W43-MM2#2⁵ has no significant emission at high velocities in the On-Off spectrum in CO, but has a possible weak extend in high velocities (up to $\sim \pm 10$ km s $^{-1}$) in SiO, at the limit of the significance (4.8 and 2.5σ in the blue and red parts respectively). In Nony et al. (2023) this source is an outflow source due to some weak red lobes in CO. But these lobes are weak and are situated at relatively large distance from the core making very uncertain the association of these lobes with the core. Altogether, we therefore can conclude that our automated fast method is validated against the more classical approach of Nony et al. (2020, 2023) for 36 out 38 cores (95 %) in W43 with a disagreement for only two sources, W43-MM1 #20 and W43-MM2 #2.

Towner et al. (2024) used the SiO (J=5–4) line to search for emission that could be associated with jet and outflow activity, independent of the core positions towards all ALMA-IMF fields. In that work however there was no attempt to associate the detected high velocity lobes with the cores, making it difficult to compare with the results presented here. However, we perform a visual comparison between our SiO lobes with the catalog of SiO lobes in Towner et al. (2024). We recover $\sim 80\%$ of the SiO structures find in Towner et al. (2024). The remaining 20% lobes

³ This core is labeled as #37 in Nony et al. (2020) and Nony et al. (2023)

⁴ They correspond to sources #14 in Nony et al. (2020) and #15 in Nony et al. (2023) respectively.

⁵ It corresponds to source #6 in Nony et al. (2023).

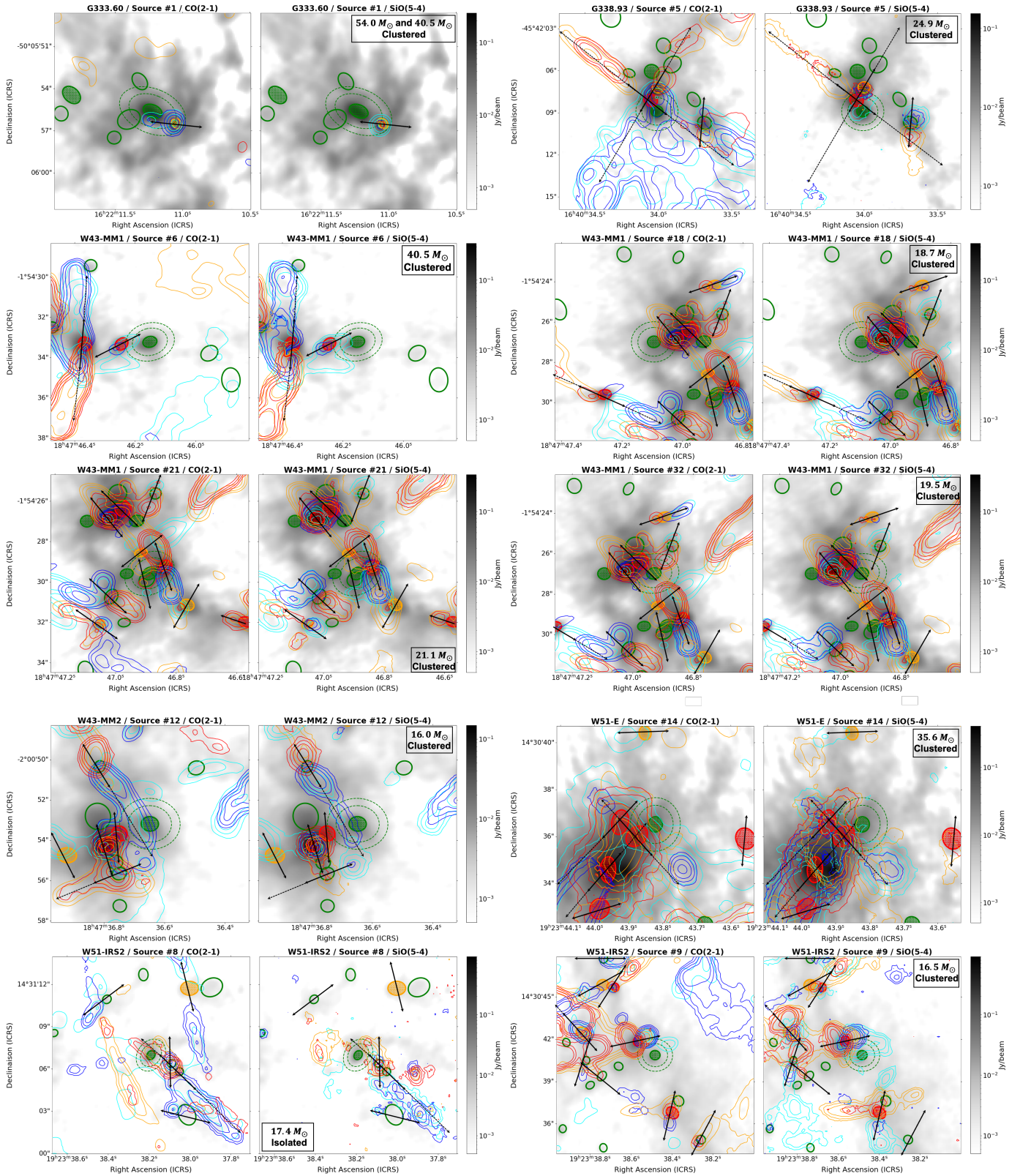


Fig. 5. CO(2-1) and SiO(5-4) molecular outflow maps centered on the 12 most massive PSC candidates, represented as the center green ellipse with an annulus in each panel (cores #1A and #1B of G333.60 are displayed as one core here, see Sect. 4.4). Ellipses in red are cores classified as protostellar (due to an association with an outflow) with a mass greater than $8 M_{\odot}$, and ellipses in orange are protostellar cores with a mass between 4 and $8 M_{\odot}$. Filled green ellipses are other PSC candidates (i.e. with $M > 8 M_{\odot}$ at 20 K) while the empty green ellipses are low mass cores which have not been analysed here. Moment 0 contours of the blue-shifted wings are overlaid on the continuum map at low velocity in cyan and high velocity in blue. Moment 0 contours of the red-shifted wings are overlaid on the continuum map at low velocity in orange and high velocity in red. Arrows represent the direction of the outflows driven by the protostars. The mass and the location of the candidate (i.e. classified as clustered or as isolated, see Sect. 5.3 for the details of the classification) are presented in each SiO map. Parameters of each map can be found in Appendix E.

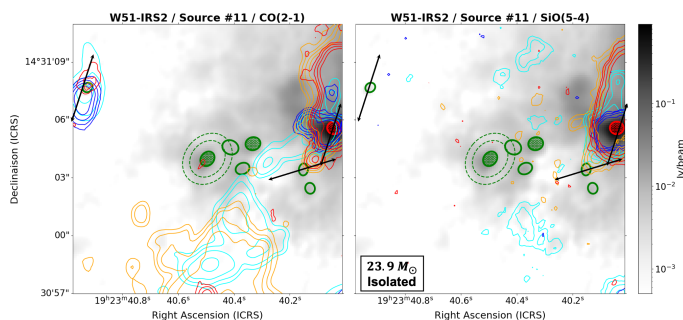


Fig. 5. continued.

do not affect our classification since none are directly associated with the cores in consideration here.

Finally, [Armante et al. \(2024\)](#) classified pre- and protostellar cores using the same CO and SiO lines as this study. Above our mass threshold, we have the same identification for four protostellar cores and one prestellar. For core #6⁶ in G012.80 however, there is a difference in the identification of outflows. [Armante et al. \(2024\)](#) classified it as prestellar, while we classify it as protostellar due to a red excess detection in the On-Off spectrum, and blue and red lobes centered on the core in the outflow lobe maps. [Armante et al. \(2024\)](#) rejected it as protostellar due to the lack of SiO lobes centered on the core, leading to the difference of classification. Overall we have an agreement on five out of six cores ($\sim 80\%$).

4.4. The complete list of PSC candidates

To arrive to the 141 cores above $8 M_{\odot}$ (using a temperature of 20 K) presented in the previous sections, that we classified into pre and protostellar cores, we have performed an additional verification to scrutinize and hence verify the continuum emission of these cores and verify that they are indeed compact individual cores.

We use the results of the GExt2D algorithm that is based on the 2D second derivative of the continuum map to check the presence of strong local curvature peak for each core. Also since the [Louvet et al. \(2024\)](#) catalog, used in this work, is actually based on images smoothed to a homogeneous physical scale of 2700 au, we may have signs of sub-fragmentation when investigating the original ALMA-IMF images and the 2D second derivative maps at the native resolution. We remove any cores that do not show either a strong local curvature or that have indications of multiple peaks in the second derivative map. In this later case, sources that lead to fragments below the $8 M_{\odot}$ cut-off are removed. On the other hand, some sources could appear as multiple at the native resolution, but each fragment can still be massive enough to stay in our list of cores. This is the case for the G333 #1 source, which corresponds to the most massive core of the complete list of PSCs with $148 M_{\odot}$ at 20 K. Figure 6 shows the second derivative map produced by GExt2D revealing that this core splits into two continuum peaks. From the ratio of flux density measurements towards both peaks at the native resolution, we estimate the fraction of the total mass distributed in both cores which are presented in Table 3. In the final complete list of PSC candidates, we have therefore split G333 #1 into

G333 #1A (North-East core) and #1B (South-West core) adding a candidate in the list.⁷

We also verify that the PSC candidates we recognize are not associated with a hot core which would point to a strong central heating source. We checked into the 76 hot core catalog of [Bonfand et al. \(2024\)](#), and found that only one of our PSC candidates (W43-MM1 #30) seem to spatially coincide with a methyl formate peak. However in [Bonfand et al. \(2024\)](#) this peak is weak (weakest methyl formate peak of the W43-MM1 hot core catalog), and could actually correspond to a spatial contamination from the extended hot core/methyl formate emission which is observed in this part of the W43 region. We also note that none of our PSC candidates in the W43 regions have been classified as hot cores in the [Brouillet et al. \(2022\)](#) study.

Our final catalog contains 42 individual PSC candidates and 99 individual protostellar cores candidates, above the threshold of $M > 8 M_{\odot}$ at 20 K. The PSC candidates are presented in Table 3 along with their physical properties we discuss in the following section.

Except the eight PSC candidates in common with the W43 study of [Nony et al. \(2023\)](#) and the one in common with the G012.80 study of [Armante et al. \(2024\)](#), the other PSC candidates from the sample of 42 cores presented here are newly found PSCs. Among these 8 PSCs in the W43 regions that are in common to our study, core #6 from W43-MM1 is one of our most massive candidates and was discovered in [Nony et al. \(2018\)](#). Core #12 from W43-MM2 and core #21 from W43-MM1 were also presented as possible high-mass prestellar cores in [Nony et al. \(2023\)](#) (labeled as core #22 and #134). The five other cores were under $16 M_{\odot}$ and not proposed to be high-mass PSC candidates in [Nony et al. \(2023\)](#).

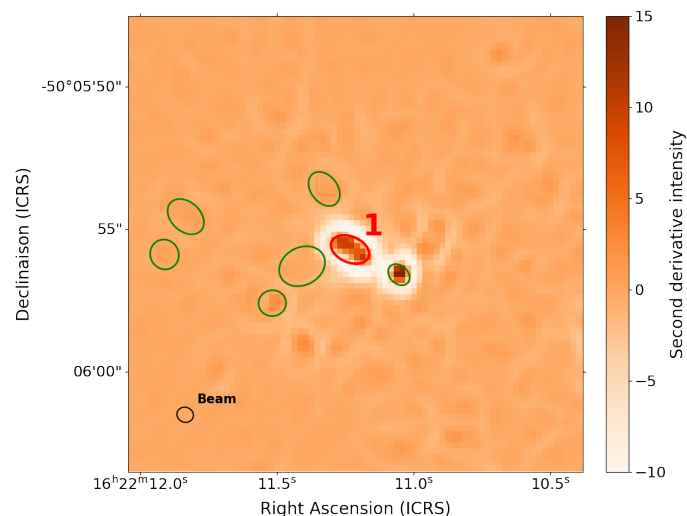


Fig. 6. Second derivative map of G333.60 with a zoom on core #1. The beam of the smoothed continuum map of G333.60 is shown in bottom left.

4.5. Basic properties of the PSC candidates

Table 3 presents the list of 42 candidates above $8 M_{\odot}$ at 20 K, together with the name of the host region, their number, their

⁷ Their respective sizes are taken from the GExt2D catalog which will be published on CDS with the catalogs of [Louvet et al. \(2024\)](#). Cores #1A and #1B correspond to cores #9 and #7 in the GExt2D catalog of the G333.60 protocluster.

⁶ This core is labeled as core #5 in [Armante et al. \(2024\)](#).

right ascension and declination coordinates (ICRS), the range of mass and the size of the core as well as the corresponding average density and free-fall time.

The dust temperatures to adopt to estimate the masses from dust emission are difficult to establish for such distant regions for which the FIR data required to observe the peak of the spectral energy distribution of dust emission have too low spatial resolution to resolve individual cores. As argued in Sect. 4.1 in such dense cores the cooling times are low pointing to possible low temperatures most probably below 20 K (see also [Bhandare et al. 2018](#)). On the other hand, the observed regions are filled by warm gas and dust due to high-mass star feedbacks as shown in the dust temperatures obtained with PPMAP in [Dell’Ova et al. \(2024\)](#) using Herschel data and derived down to 2.5'' scale (i.e. between 2 and 5 times larger than the typical core size). These PPMAP temperatures are obtained from the low resolution Herschel maps with beam sizes between 12'' and 18'' at 160 and 250 μm by a guided (bayesian) method using also the high resolution 1.3mm ALMA-IMF images. The PPMAP dust temperatures are estimated by averaging over the pixels of each source in the "non-corrected" dust temperature maps of [Dell’Ova et al. \(2024\)](#). We use these 2.5'' scale temperatures to derive a maximum dust temperature for each core and adopt 20 K as a conservative lowest temperature. Using these as upper and lower limits in temperature, we obtain lower and upper limits in mass, giving a possible range of mass for each PSC candidate. In Table 3 we have listed the corresponding range of masses for each core and give an adopted central mass taken at the middle of this uncertainty range. We use these lower and upper masses to extract a symmetric error on the density and free-fall time computations (see below).

Similarly we propose to adjust the dust temperatures to be adopted in the following to best estimate the masses of the protostellar cores. We propose to also adopt the PPMAP temperatures from [Dell’Ova et al. \(2024\)](#) but using the 70 μm corrected ones such as in [Louvet et al. \(2024\)](#) and which are best suitable for internally heated sources such as high-mass protostellar cores.

Using these best estimate dust temperatures for both PSCs and protostellar cores we thus finally get a reduced number of cores above 8 M_{\odot} with 30 PSCs and 52 protostellar cores⁸ from the full sample of 42 PSCs and 99 protostellar cores originally analyzed for outflows in the previous sections. These 82 cores (30 PSCs and 52 protostellar cores) are then going to be the ones further discussed in following sections. The spectra and molecular outflows maps for each 30 PSC candidates not shown in Fig. 5 are shown in Appendix E. We also display in appendix F the location of the PSC candidates and protostellar cores identified in each protocluster.

To calculate the volume density n_{H_2} , we use as a radius the 1.3mm continuum deconvolved size $\text{FWHM}_{1.3\text{mm}}^{\text{dec}}$ as: $\text{FWHM}_{1.3\text{mm}}^{\text{dec}} \simeq \sqrt{a_{1.3\text{mm}} \times b_{1.3\text{mm}} - \Theta_{\text{beam}}^2} \times d$, with $a_{1.3\text{mm}}$ and $b_{1.3\text{mm}}$ the major and minor FWHM axes of the core, Θ_{beam} the geometric mean of the beam FWHM of the smoothed continuum map, and d the distance of the region. As in [Pouteau et al. \(2022\)](#), we fix a minimum deconvolved size at half the beam FWHM. We compute the H_2 volume density as:

$$n_{\text{H}_2} = \frac{M_{\text{source}}}{\frac{4}{3}\pi \mu m_{\text{H}} (\text{FWHM}_{1.3\text{mm}}^{\text{dec}})^3} \quad (2)$$

⁸ The full list of protostellar cores down to $\sim 4 M_{\odot}$ using the PPMAP temperature is presented in appendix C.

with M_{source} the mass of the source, $\mu = 2.8$ the mean molecular weight of interstellar gas, and m_{H} the mass of the hydrogen atom. Using the average volume density, we compute the free-fall time of each core as:

$$t_{\text{ff}} = \left(\frac{3\pi}{32G\rho_0} \right)^{1/2} \simeq 10^4 \text{ yr} \left(\frac{n_{\text{H}_2}}{10^7 \text{ cm}^{-3}} \right)^{-1/2} \quad (3)$$

with G the gravitational constant, ρ_0 and n_{H_2} the volumetric mass and volume density of the core, respectively.

We also classify the PSC candidates according to their environmental conditions. We define an environment as clustered if the PSC has two or more high-mass ($M > 8 M_{\odot}$) cores within a radius of 0.15 pc, and as isolated if they have less than two neighbouring high-mass cores. This criterion was chosen to take into account both crowded environment and mass. We present in Table 4 the ranges in mass, size, volume density, and free-fall time of the 30 PSC candidates with $M > 8 M_{\odot}$, for the three different hypothesis (average mass, mass at 20 K, and mass using the PPMAP dust temperature). The minimum, mean, and maximum of each value are presented in each column. The range of free-fall times, between $\sim 2 \times 10^3$ yr and $\sim 2 \times 10^4$ yr, is in agreement with previous studies on massive starless cores (e.g. [Kong et al. 2017](#), [Duarte-Cabral et al. 2013](#)). We have roughly as many clustered PSC candidates as isolated ones when including all the cores (17 clustered and 13 isolated), but 10 of the 12 most massive ones are found in clustered regions (see Fig. 5), which is expected as most of the mass is located in these crowded clumps of the protoclusters.

From all the 14 protoclusters studied, only G328.25 does not host any PSC candidate above 8 M_{\odot} using a dust temperature of 20 K. Core #22 in W51-IRS2 identified as PSC candidate is also covered by the W51-E field (identified as core #20). We keep this object in W51-IRS2 as the signal to noise ratio in this region is higher. We have a large number of PSC candidates in the W51-IRS2 region with ten cores, followed by the W43-MM1 region with seven of them. In between, we have the G333.60 region with five candidates, G338.93 with four, G008.67, W43-MM2 and W51-E with three candidates each, and G337.92 with two candidates. Finally, the G010.62, G012.80, G327.29, G353.41, and W43-MM3 regions host only one candidate each.

5. A new sample of high-mass PSC candidates

5.1. High-Mass PSCs defined as massive cores not hosting yet any highly accreting protostars

It is difficult and uncertain to decide which observed mass reservoirs are going to truly form high-mass stars (larger than 8 M_{\odot}). Here we adopt a mass threshold of 16 M_{\odot} corresponding to a core to star efficiency ϵ_{cse} of 50 % to form a final 8 M_{\odot} star. In Table 3 (in bold font), using our adopted mass estimate, we find that 12 candidates then qualify as high-mass and we propose that they represent the robust sample of high-mass PSC candidates to be considered below for discussion. The rest of the 30 candidates will be labeled as PSC candidates in the following.

The most probable driver for high-mass star formation is the high level of dynamical (convergent) motions at the scale of dense clumps ([Schneider et al. 2010](#); [Galván-Madrid et al. 2010](#); [Peretto et al. 2013](#); [Álvarez-Gutiérrez et al. 2024](#); see also references in [Motte et al. 2018a](#)). These convergent flows should lead to large infall rates at core scales and then to large final accretion rates of the newly formed high-mass protostars. In order to form a 30 M_{\odot} protostar in 0.3 Myr, the accretion rate has to be of the

Table 3. List and properties of the sample of prestellar core (PSC) candidates.

Region	Source	RA [deg]	DEC [deg]	Mass [range] ¹ [M _⊙]	FWHM ^{dec} [au]	n_{H_2} ² [$\times 10^6 \text{ cm}^{-3}$]	t_{ff} ² [kyr]	Location ³
G008.67	#4	271.580761	-21.6237093	7.8 [6.6 – 8.9]	3870	4.1 ± 0.6	15.7 ± 1.2	C
G008.67	#7	271.5800126	-21.6251966	13.7 [11.2 – 16.2]	2780	19.3 ± 3.5	7.2 ± 0.7	C
G008.67	#10	271.5774356	-21.6271193	7.4 [5.9 – 8.9]	4120	3.2 ± 0.6	17.7 ± 1.8	I
G010.62	#4	272.6216933	-19.9291438	11.7 [8.7 – 14.7]	1840	56.7 ± 14.6	4.2 ± 0.6	I
G012.80	#5	273.5482204	-17.9458195	7.4 [6.8 – 8.1]	1450	73.6 ± 6.6	3.7 ± 0.2	I
G327.29	#11	238.2800319	-54.6194279	8.6 [6.6 – 10.6]	3480	6.2 ± 1.4	12.7 ± 1.5	C
G333.60	⁴#1A	245.5468839	-50.0987477	54.0 [35.7 – 72.3]	2640	88.8 ± 30.1	3.4 ± 0.6	C
G333.60	⁴#1B	245.5466503	-50.0988518	40.5 [26.9 – 54.2]	2020	148.8 ± 50.2	2.6 ± 0.5	C
G333.60	#8	245.5282954	-50.1068134	6.7 [5.4 – 8.0]	2510	12.8 ± 2.5	8.8 ± 0.9	C
G333.60	#26	245.535353	-50.1041745	7.0 [4.9 – 9.1]	2310	17.3 ± 5.1	7.6 ± 1.2	I
G333.60	#45	245.549303	-50.0984873	6.4 [4.5 – 8.2]	4370	2.3 ± 0.7	20.8 ± 3.2	C
G337.92	#3	250.2949021	-47.1343006	12.0 [9.2 – 14.8]	2750	17.4 ± 4.1	7.6 ± 0.9	C
G337.92	#5	250.295556	-47.134715	11.2 [8.7 – 13.7]	3450	8.3 ± 1.9	11.0 ± 1.3	C
G338.93	#5	250.1417392	-45.7025004	24.9 [17.4 – 32.4]	1750	140.5 ± 42.4	2.7 ± 0.4	C
G338.93	#7	250.1378537	-45.7040233	10.0 [8.2 – 11.8]	1470	95.4 ± 16.8	3.2 ± 0.3	C
G338.93	#13	250.1423231	-45.6931039	11.1 [9.5 – 12.7]	3090	11.4 ± 1.7	9.4 ± 0.7	I
G338.93	#16	250.1418854	-45.701708	6.5 [4.8 – 8.2]	2930	7.8 ± 2.1	11.3 ± 1.6	C
G353.41	#5	262.6101515	-34.6960014	12.7 [9.9 – 15.6]	2630	21.2 ± 4.7	6.9 ± 0.8	C
W43-MM1	#6	281.9423152	-1.909246	40.5 [37.3 – 43.6]	2030	146.5 ± 11.4	2.6 ± 0.1	I
W43-MM1	#8	281.938703	-1.9102889	8.3 [7.5 – 9.0]	1350	101.6 ± 8.9	3.1 ± 0.1	C
W43-MM1	#14	281.944974	-1.9044595	9.1 [8.4 – 9.7]	1350	111.6 ± 8.2	3.0 ± 0.1	I
W43-MM1	#18	281.9462451	-1.9075171	18.7 [17.9 – 19.4]	1930	78.6 ± 3.0	3.6 ± 0.1	I
W43-MM1	#21	281.9453834	-1.9082357	21.1 [20.3 – 21.9]	2390	46.8 ± 1.7	4.6 ± 0.1	C
W43-MM1	#30	281.9456971	-1.9082389	12.2 [11.8 – 12.6]	1350	150.0 ± 5.4	2.6 ± 0.0	C
W43-MM1	#32	281.9455609	-1.9075139	19.5 [18.8 – 20.1]	2180	56.9 ± 1.9	4.2 ± 0.1	C
W43-MM2	#2	281.9001273	-2.0224281	13.0 [11.7 – 14.3]	2020	47.7 ± 4.8	4.6 ± 0.2	C
W43-MM2	#9	281.9034863	-2.0173945	7.8 [6.7 – 8.8]	2160	23.3 ± 3.3	6.6 ± 0.5	I
W43-MM2	#12	281.9027193	-2.014794	16.0 [14.0 – 18.1]	3390	12.4 ± 1.6	9.0 ± 0.6	I
W43-MM3	#3	281.9207197	-2.0057611	10.8 [9.4 – 12.2]	2420	23.1 ± 3.0	6.6 ± 0.4	C
W51-E	#14	290.9326071	14.510126	35.6 [28.8 – 42.3]	2080	119.7 ± 22.7	2.9 ± 0.3	I
W51-E	#28	290.9319946	14.5089561	7.5 [6.7 – 8.2]	1600	55.1 ± 5.8	4.3 ± 0.2	C
W51-E	#31	290.9288221	14.5159753	9.5 [9.3 – 9.7]	4170	3.9 ± 0.1	15.9 ± 0.2	C
W51-IRS2	#8	290.9091553	14.5185781	17.4 [14.0 – 20.9]	1930	73.4 ± 14.5	3.7 ± 0.4	I
W51-IRS2	#9	290.9103723	14.5113251	16.5 [13.0 – 19.9]	2510	31.5 ± 6.7	5.6 ± 0.6	I
W51-IRS2	#11	290.9187587	14.5177443	23.9 [17.8 – 30.0]	2950	28.2 ± 7.2	6.0 ± 0.8	C
W51-IRS2	#17	290.9245968	14.5197752	11.5 [9.4 – 13.5]	3950	5.6 ± 1.0	13.3 ± 1.2	I
W51-IRS2	#22	290.9255723	14.5112676	7.6 [6.1 – 9.1]	1350	93.5 ± 18.6	3.3 ± 0.3	I
W51-IRS2	#24	290.9114738	14.5186878	7.7 [6.4 – 9.1]	3120	7.7 ± 1.4	11.4 ± 1.0	I
W51-IRS2	#28	290.9052888	14.5184717	10.1 [8.7 – 11.5]	3910	5.1 ± 0.7	14.0 ± 1.0	I
W51-IRS2	#32	290.9069467	14.5064897	9.7 [8.3 – 11.2]	1900	43.0 ± 6.4	4.8 ± 0.4	I
W51-IRS2	#38	290.9262262	14.515357	7.7 [6.1 – 9.4]	1800	40.1 ± 8.6	5.0 ± 0.6	I
W51-IRS2	#42	290.9180791	14.5179626	11.5 [8.7 – 14.2]	2820	15.5 ± 3.7	8.0 ± 1.0	I

Bold font is used to present the robust sample of PSC candidates with $M > 16M_{\odot}$.

¹ Mean masses of the candidates with their range using the non-corrected PPMAP dust temperature (see Dell’Ova et al. 2024) and 20 K as high and lower limits in temperature.

² Volume density and free-fall time (see section 4.5).

³ Location of the source with C meaning clustered and I meaning isolated, based on the criteria described in Sect. 4.5.

⁴ This source contains two continuum peaks that can be seen in the GExt2D second derivative map. We then use the flux density and size of each GExt2D source to compute the masses and densities of the two peaks (see section 4.4).

order of $10^{-4} M_{\odot} \text{ yr}^{-1}$. These large accretion rates are compatible with the global infall rates at the scales of clumps which are directly observed with for instance $2.5 \times 10^{-3} M_{\odot} \text{ yr}^{-1}$ in the SDC335 clump which contains only a few high-mass protostars;

(Peretto et al. 2013; see also Contreras et al. 2018; Redaelli et al. 2022; Olguin et al. 2023). It is also compatible with accretion rates derived from CO outflows for high-mass/intermediate mass protostars (Duarte-Cabral et al. 2013; Maud et al. 2015; Avison

Table 4. Range of the properties of the 30 PSC candidates with $M > 8 M_{\odot}$.

	Mass ¹ [M_{\odot}]	FWHM ^{dec} ¹ [au]	n_{H_2} ¹ [$\times 10^6 \text{cm}^{-3}$]	t_{ff} ¹ [kyr]
Adopted mass	8.3 - 17.5 - 54.0	1350 - 2509 - 4170	3.9 - 54.1 - 150.0	2.6 - 6.3 - 15.9
$M_{20\text{K}}$	9.0 - 20.8 - 72.3	1350 - 2509 - 4170	4.0 - 62.6 - 182.9	2.3 - 5.9 - 15.7
$M_{\text{T}_{\text{PPMAP}}}$	6.6 - 14.2 - 37.3	1350 - 2509 - 4170	3.9 - 45.7 - 144.6	2.6 - 7.0 - 16.1

¹ Each range is presented as minimum - mean - maximum.

et al. 2021). A young high-mass protostar is therefore expected to be a strongly accreting object. High rate accretion has always to be accompanied by similarly high rate ejection (e.g. Cabrit & Bertout 1992; Bontemps et al. 1996; Beuther et al. 2002; Duarte-Cabral et al. 2013; Maud et al. 2015) to allow for angular momentum removal as predicted in the magneto-centrifugal jet/wind processes at disk and protostellar scales (Ferreira et al. 2006; Mignon-Risse et al. 2021; Commerçon et al. 2022). Young highly accreting high-mass protostars should thus all be powerful outflow drivers. In addition since the observed cores are massive and dense, any jets or winds escaping from high-mass protostars should always be revealed as CO outflows entrained inside the cores themselves.

We therefore adopt here for the criterium to recognize an excellent candidate to be a HM PSC that it should be a compact core ($\text{FWHM}^{\text{dec}} < 5000 \text{au}$) massive enough to form a high-mass star ($16 M_{\odot}$) and not driving any CO/SiO outflow, indicating that the core does not host yet any high-mass protostar with a large accretion rate. This definition of an excellent candidate to be a HM PSC may allow for the existence of low-mass protostars in the core with a global (adding all accretion rates of protostars) low accretion rate. This could result in low-mass protostars within these cores being misclassified as prestellar cores. We note that in the view promoted by Motte et al. (2018a), the earliest phases to form high-mass stars would indeed correspond to cores hosting few low-mass protostars competing for mass from the global infall rate. We note, however, that this stage with only low-mass protostars in a high-mass core cannot last for long if the infall is globally large. Indeed, material would accumulate very fast in the protostars, with a large sum of all accretion rates leading to a sum of low-mass ejections which would cumulate as a detectable global outflow from the core (see discussion for the possible effects of fragmentation, case 6 in Sect. 7.8).

We see in Fig. 5 that these 12 high-mass PSCs (cores #1A and #1B of G333.60 are displayed as one core in this figure) are mostly situated in the crowded, central regions of the protoclusters where the confusion between outflows from nearby (also massive) protostars is the highest. This is expected since high-mass stars are believed to form mostly at the center of the densest and most massive clumps where several high-mass stars may form roughly at the same time. Despite this unavoidable confusion, we are confident that we have a robust selection due to our systematic approach. The On-Off spectra are expected to reveal any excess of outflow emission in CO or SiO centered on the source, and thus are expected to provide a reliable mean of detecting outflow emission coincident with the position of the core. We can certainly exclude for all these 12 high-mass cores that they could drive a powerful outflow as expected if they would be strongly accreting objects.

5.2. Other protostellar tracers towards the HM PSC candidates

One of the traditional ways to recognize a protostar is to probe mid-IR emission (typically below $100 \mu\text{m}$) to detect warm dust emission indicative of a significant internal heating inside the collapsing core/envelope. We cannot use the mid-IR probe towards the ALMA-IMF compact cores, since they are not resolved individually in the available Herschel or Spitzer maps (see e.g. Gutermuth et al. 2009; Motte et al. 2010). The spatial resolution of Herschel at $70 \mu\text{m}$ or of Spitzer at $24 \mu\text{m}$ used for instance by Bontemps et al. (2010) in Aquila are of the order of 6 arcsec, i.e. between 5 and 15 times (depending on the distance of our regions) larger than the angular size of the here studied cores. Alternatively, molecular line emission, such as hot-core tracers, could also trace the presence of warm gas in the cores. We have verified that none of our HM PSC candidates are hot cores in Bonfand et al. (2024). A forthcoming paper (Vaille-Manet et al. in prep) will further investigate the molecular emission of the HM PSC candidates. A preliminary analysis show that all cores have chemical properties compatible with cold gas typically between 20 and 25 K with clear sign of CO depletion and detections of N_2H^+ towards the cores.

5.3. Comparison with previous high-mass PSC surveys

We have therefore discovered 12 robust HM PSC candidates above $16 M_{\odot}$ and 18 lower mass PSCs between 8 and $16 M_{\odot}$ (see Table 3) as well as 52 protostellar cores above $8 M_{\odot}$ in the ALMA-IMF fields that we can then discuss further below.

It is important to have discovered and catalogued a significant number of PSCs with potential mass reservoirs massive enough to qualify as high-mass star precursors. The number of candidates appears large compared to what is known in the literature (see below) but still low compared to the total number of cores in the ALMA-IMF sample. The 12 robust candidates of the sample above $16 M_{\odot}$ represent $\sim 2\%$ (12/584) of the total number of cores in Louvet et al. (2024).

To our knowledge, no work has yet reached large enough statistics in high-mass SFRs to investigate well high-mass PSC candidates. First systematic surveys such as Motte et al. (2007) and Bontemps et al. (2010) in Cygnus X could only find a couple of high-mass cores (9 objects at a $\sim 2000 \text{au}$ scale in Bontemps et al. 2010) and only one candidate to be prestellar (CygX-N53-MM2) could be identified among them using CO outflows in Duarte-Cabral et al. (2013). This candidate still stands as a probable intermediate mass PSC with a here revised mass of $9.5 M_{\odot}$ in the average convolved size of 3800au of the ALMA-IMF PSC candidates, using the same dust temperature of 20 K as in their study and our emissivity (see Sect. 4.1 and 4.5). Similarly Tan et al. (2013) led a survey in the first galactic quadrant towards cold IRDCs detected in N_2D^+ , but their best candidate

happened to correspond to two early stage protostellar cores (see Tan et al. 2016). Louvet et al. (2019) did not find any HM PSC candidate in NGC2264 either. In Barnes et al. (2023) one PSC candidate of ~ 2200 au was identified in the dragon cloud (core C2c1a) using 1.3 mm continuum, with a mass of $23 M_{\odot}$. For a direct comparison with the present work, using the dust opacity presented in Sect. 4.1 and a temperature of 20 K, the mass of this PSC candidate would actually be $5.2 M_{\odot}$ (a dust temperature of 10.4 K is used in their study). Wang et al. (2014) used the SMA and similarly found a PSC candidate (G11.11-P6-SMA1) of $28 M_{\odot}$ and ~ 2600 au, which, using our dust emission flux to mass conversion and temperature, would actually have a mass of $7.4 M_{\odot}$ (a dust temperature of 11 K is used in their study). As discussed in Sect. 4.1, these two cores would not make it in our complete list of 42 PSC candidates above $8 M_{\odot}$. Finally, the ALMA project ASHES which mapped massive IR dark clumps did not succeed in finding high-mass PSC candidates with $M > 16 M_{\odot}$ (see Morii et al. 2023). Their most massive cores without outflow have lower masses than $16 M_{\odot}$ and have deconvolved FWHM larger than the core sizes in our sample with an average factor of ~ 5 .

In Fig. 7 we present the distribution of the masses and sizes of the 30 PSC candidates with $M > 8 M_{\odot}$ and added the candidates discussed above from the literature, where we recomputed their mass using our dust emissivity with a dust temperature of 20 K and the temperature used in their studies (see the paragraph above). We clearly see that our new detections are probing for the first time the high mass regime to investigate the initial conditions prevailing to form high-mass stars (i.e. above $8 M_{\odot}$). We note however that among the 12 robust high-mass PSC candidates, only 4 cores have mass reservoirs greater than $30 M_{\odot}$ most probably highlighting the difficulty to find cores in the highest stellar mass regime. Clustered and isolated candidates are displayed as blue and red circle points respectively (see Sect. 4.5 for details on this classification). Protostellar cores with $M > 8 M_{\odot}$ are shown as green triangles. It appears that 10 of the 12 most massive candidates are found in a clustered environment as expected since these crowded regions are the most probable places to form highest mass stars. In contrast, a significant fraction of the cores below $16 M_{\odot}$ are found to be isolated with 11 of the 18 remaining cores having one or no high-mass core neighbor.

6. Are high-mass PSCs really rare?

So far an extremely small number of candidates to be HM PSCs have been recognized in the literature (Sect. 5.3) suggesting that the compact high-mass cores in pre-collapse or at the very beginning of collapse/assembly without high-mass protostellar activity yet are rare and may even not exist at all (see Motte et al. 2018a). We here actually detect some robust HM PSC candidates up to masses of $\sim 50 M_{\odot}$ (between 35 and $70 M_{\odot}$ accounting for the uncertain dust temperature). This indicates that high-mass PSCs exist up to relatively high masses. Since these masses are similar to those observed for the protostellar cores (see green triangles in Fig. 7), it suggests that our ability to probe even larger mass reservoirs might actually be limited by the statistics of cores we could detect in ALMA-IMF.

Investigating the number statistics of prestellar versus protostellar cores, we find about half as many HM PSCs than high-mass protostars above $16 M_{\odot}$ with 12 [9-14]⁹ HM PSCs and 27

high-mass protostars among a total of 39 high-mass cores; i.e. 69% [66-75%] of protostars among these 39 [36-41] cores. This fraction is statistically compatible with the value found by Nony et al. (2023) on the sub-sample obtained only in the three proto-clusters of W43 with a value of $\sim 80\%$ of protostars. We note also that the mass scale of the present work is slightly higher as we use a source catalog on smoothed images at a single physical size beam (for homogeneity reason over all regions). Since in Nony et al. (2023) the fraction of protostars is strongly dependent of the mass, the difference between these fractions is also explained by this shift toward slightly higher masses in the present work.

Typically low-mass star forming regions host significantly more numerous prestellar than protostellar cores. In Aquila, Könyves et al. (2015) found a total of 446 prestellar cores (gravitationally bound cores without $70 \mu\text{m}$ emission) for only 58 protostars, i.e a factor of 8 times more prestellar cores to be compared to the factor ~ 0.5 found here for HM PSCs. The high-mass PSCs are thus indeed significantly rarer than their low-mass counterparts, and are globally extremely rare due to the rarity of high-mass cores, protostars, and stars.

The reason why previous surveys for HM PSCs could not detect almost any good candidates is probably two-fold. First they are indeed very rare, slightly rarer than high-mass protostars (driving the need for large samples of high-mass cores), and second they are mostly clustered with the high-mass protostellar objects in dense clumps making their identification extremely difficult (confusion with the strong outflows from the very nearby high-mass protostars). We see that most of the HM PSCs above $16 M_{\odot}$ are indeed found clustered in the central clumps of the regions (see Fig. 7).

7. Statistical lifetimes of high-mass prestellar cores

The number of PSC candidates can be used to estimate the statistical duration of the prestellar phase to form high-mass stars providing that we can choose a favored protostellar lifetime for high-mass stars.

7.1. Accretion phase and protostellar lifetimes

The lifetime of (high-mass) protostars which should correspond to the main accretion of the final star is not a well determined quantity due to the difficulty to estimate it observationally or theoretically. Statistical estimate of protostellar lifetimes was firstly introduced by Beichman et al. (1986) who studied the embedded young stellar objects (YSOs) in the sample of cores of Myers et al. (1983). Only few papers focused on the lifetime of the massive protostellar phase. Duarte-Cabral et al. (2013) adopted 300 kyr based on the observed trend that the protostellar lifetime for the intermediate/high mass regime is similar to the low-mass value which was debated to range from 200 to 400 kyr, and thanks to indirect estimates of accretion rates using CO outflows. Independently and in the high-mass regime, Mottram et al. (2011) surveyed massive YSOs and compact HII regions at the scale of the galactic plane. Their obtained luminosity distribution were used to compare the number of massive YSOs (high-mass protostars) and of HII regions with the total number of massive stars. This allowed them to estimate statistical lifetimes as a function of the luminosity of the objects (i.e. equivalent to the final mass of the object). At low luminosities (B0.5 stars, lowest masses) the obtained lifetime of 500 kyr represents the total protostellar time. At higher luminosities a part of the compact HII regions can actually be still accreting protostars and should then

⁹ range of number of PSCs above $16 M_{\odot}$ from the range of uncertain mass for PSCs

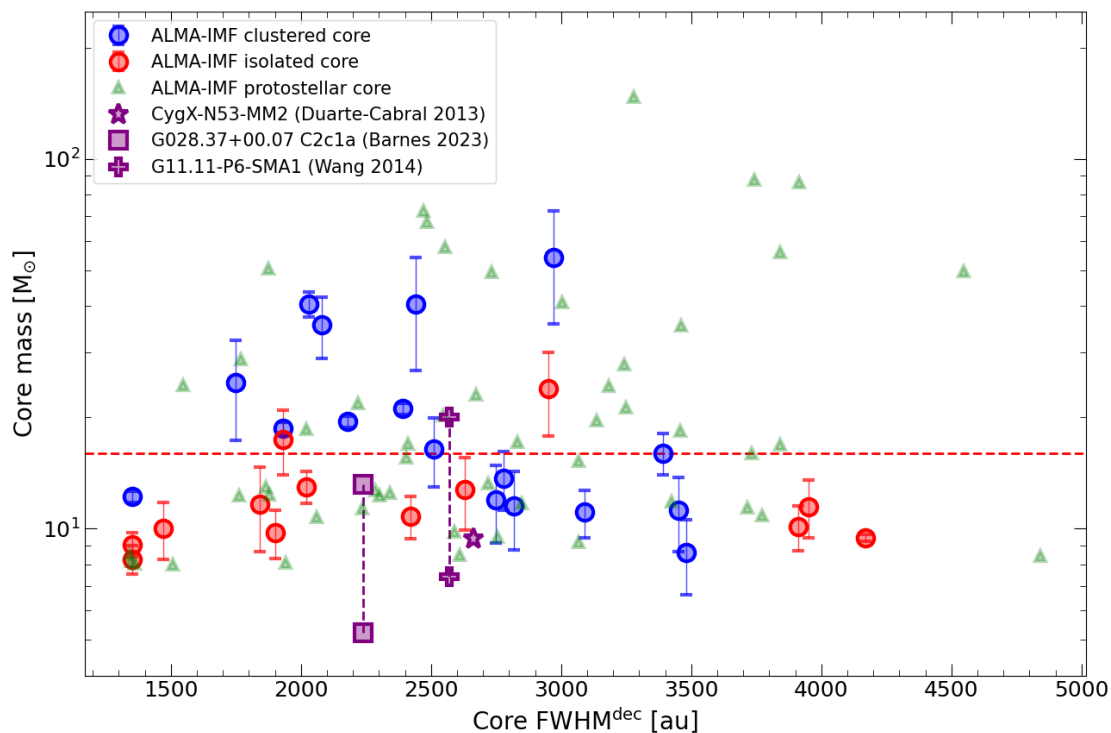


Fig. 7. Mass distribution in function of the size of the total sample of 30 PSC candidates. Blue and red circles correspond to clustered and isolated candidates respectively. Errorbar symbols indicate the whole range of possible mass justified in Sect. 4.5, using 20 K and PPMAP non corrected temperatures as lower and upper limits in temperature. The red dashed line corresponds to the threshold of $16 M_{\odot}$. The markers in purple are the previous high-mass PSC candidates from Duarte-Cabral et al. (2013), Barnes et al. (2023), Wang et al. (2014) using the dust emissivity from the present work, a temperature of 20 K and the temperature used in these studies. The prestellar core from Duarte-Cabral et al. (2013) has only one symbol because a temperature of 20 K was already adopted in their work. Protostellar cores with $M > 8 M_{\odot}$ are shown in green triangles.

be included in the protostellar lifetime (see below in Sect. 7.3). Interestingly enough Nony et al. (2024) in the W49 region found that of the order of one third of the UC HII regions are still dust emission cores and are possibly still protostellar (accreting) objects. Adding massive YSO and one third of the compact HII region lifetimes from Mottram et al. (2011) we then get a lifetime of the order of 200 kyr for O7-O8 final stars. It also suggests that the protostellar lifetime may decrease with mass from 500-600 to 100-200 kyr. In W49, Nony et al. (2024) derived a protostellar lifetime of 140 kyr.

Altogether, accounting for above constrains and uncertainties, we adopt as a baseline a constant protostellar lifetime of 300 ± 100 kyr. At one point of the discussion we will also consider the possibility of a decrease of this time for highest masses that we will adopt from 300 to 100 kyr for final mass from 8 to $\sim 30 M_{\odot}$.

7.2. Mass dependence of the statistical lifetime

Down to a core mass of $8 M_{\odot}$ using our adopted dust temperature (Sect. 4.5 and Tab. 3), we detect a total of 30 PSC candidates. Compared to the total of 52 protostellar (with outflows) cores above $8 M_{\odot}$ which correspond to a statistical time of 0.3 Myr, we then get a global statistical time for PSCs above $8 M_{\odot}$ of ~ 170 kyr. These 30 candidates also provides a statistical basis to investigate possible mass dependencies of the fractions and statistical lifetimes of prestellar cores in the observed mass regime. In Nony et al. (2023) with 8 PSCs (5 above $8 M_{\odot}$ and 3 above $16 M_{\odot}$) in the W43 regions, a trend of a decrease of the fraction of PSCs toward the high-mass regime was observed. We can here go one step further with a larger statistics.

In Fig. 8 left panel we show the histogram of the number of prestellar cores (blue histogram) compared to the number of protostellar cores (red histogram). To compute the masses, PPMAP temperatures are taken for protostellar cores, while we use our best temperature estimates (see Sect. 4.5 and Tab. 3) for the prestellar cores. Assuming a 50 % core to star efficiency (hereafter ϵ_{cse}), we have indicated the corresponding final mass of the stars on the upper x-axis. Between core masses of 8 and $\sim 16 M_{\odot}$ (two first bins) we obtain a relatively similar number of prestellar and of protostellar cores (fraction PSCs/proto close to 1) and with a trend of a decreasing fraction towards high masses. This fraction continues to decrease above $16 M_{\odot}$ to a fraction of PSCs more of the order of 0.5 of the number of protostars. In terms of lifetimes (green points in Fig. 8), this suggests a decrease from ~ 300 kyr to ~ 150 kyr in the highest mass regime which for ϵ_{cse} of 50 % would correspond to final masses of the order of 20-30 M_{\odot} (see upper x-axis of Fig. 8). We note that we do not detect HM PSC candidates in the last bin of mass of Fig. 8 leading to a large uncertainty on the resulting upper limit of lifetime for these highest masses (last green point in the figure).

7.3. Correction for missing UCHII protostars

Some of the bright millimeter cores in the survey have a clear contribution at 3 mm from free-free emission, pointing to the existence of young ionising high-mass protostellar objects, i.e. of so-called Ultra compact HII (UCHII) regions inside the detected cores¹⁰. Some of these free-free contaminated millimeter sources

¹⁰ Free-free contamination could also originate from other mechanisms such as radiojets (Anglada 1996).

are expected to be still accreting. High-mass stars have indeed to still strongly accrete mass while being already an ionising protostar so that they can reach masses well above $10 M_{\odot}$ (Yorke & Sonnhalter 2002; Krumholz et al. 2007; Keto 2007; Tanaka et al. 2016). For the most massive stars, it is even a significant fraction of the protostellar lifetime (accretion phase) which is expected to appear as an UCHII region (Peters et al. 2010). In the Louvet et al. (2024) study, 68 such compact free-free sources are found, i.e. of the order of 10 % of the whole sample of cores. These free-free contaminated cores are either high-mass protostars that are still accreting, or slightly more evolved objects, i.e. main sequence stars with accretion finished with a remaining compact halo of ionised gas (see for instance Nony et al. 2024 in W49). We note that with our outflow detection tool we indeed found some outflows around a few of these bright free-free contaminated compact objects in the survey confirming the protostellar nature of these objects. We even decided to add to our list of high-mass protostars the three least free-free contaminated objects initially excluded from the catalogs of Louvet et al. (2024), those with a spectral index close to two (cores #5 and #9 of W51-E and core #5 of W51-IRS2) and found them indeed associated with an outflow¹¹.

The more massive a star is going to be, the larger is the fraction of its accretion time as an ionising protostar (ultra or hyper compact HII regions, hereafter UCHII regions). These ionising protostars are not included in the sample of cores of Louvet et al. (2024) due to the fact that it is not trivial to evaluate a proper dust emission at 1.3 mm to estimate their envelope masses. They are therefore not accounted for in the red histogram of Fig. 8 and in the PSC lifetime estimate. In order to compensate for these missing high-mass protostars we have estimated for each bins of final stellar masses of Fig. 8 the number of expected UCHII protostars. For that we use the model of protostellar evolution of Hosokawa & Omukai (2009) as expressed in Duarte-Cabral et al. (2013). Assuming a constant accretion rate and a core to star efficiency ϵ_{cse} of 50%, for each final stellar mass bin we can estimate the percentage of lifetime a protostar is going to be ionising as an UCHII region (see appendix D). This leads to a number of free-free contaminated protostars in each bin, as an additional fraction of the number of observed non-ionising protostellar cores (red histogram). The number of these expected ionising protostars are shown as a yellow histogram in Fig. 8. This larger number of protostars in the highest mass bins then decreases the fraction of PSCs in the highest mass regime and decreases the corresponding PSC lifetime.

Adopting this correction we have plotted in Fig. 8 the lifetime values for all mass bins (blue connected points). In addition we show the dispersion in the histograms resulting from the range of possible masses for PSCs (see Tab. 3) as black and brown connected points. Together with the uncertainty bars for each points reflecting the Poisson noise, we then get a view of the evolution of the lifetimes with masses and of the dispersion of the obtained values due to PSC mass uncertainties. A decrease of the lifetime is now visible with the correction while without correction there was a tendency of a flattening (connected green points). In the right panel of Fig. 8 we present the mean PSC lifetime extracted from the three hypotheses of the left panel with its one sigma dispersion. The values in ranges of mass of this mean PSC lifetime and its dispersion are given in Tab. 5. We see that the decrease now goes from approximately 300 kyr in the lowest masses to 100 kyr in the highest mass regime of detected

PSC candidates of 40 to $50 M_{\odot}$ (corresponding to final stellar masses from ~ 5 to $\sim 25 M_{\odot}$ for ϵ_{cse} of 50 %).

7.4. Accounting for the evolution of protostellar core masses

So far we have compared the number of PSCs to the number of protostellar cores above the same threshold in core masses and for the bins of Fig. 8. However, in the simplest view of an initially set mass reservoir (without strong replenishment during protostellar times, i.e. a core-fed view), the protostellar core masses (also referred as protostellar envelope) are expected to decrease as the inner protostar accretes and ejects material.

Accounting for a constant rate for the decrease of core/envelope mass and constant accretion rate, a protostar is statistically observed at half of its protostellar time which would then correspond to be at half of its initial core mass (i.e. its original mass at the stage of PSC). We have revised Fig. 8 to account for such a possible decrease in protostellar core masses by doubling the present day mass of protostellar cores (as a proxy for their initial core mass). The result of this correction is displayed in Fig. 9. In practice, however, this simple adjustment has to be slightly revised for the protostars which have a significant part of their accretion time appearing as ionising protostars. For all mass bins for which a part of the protostars are expected to be ionising (bins with a contribution of ionising objects displayed as a yellow histogram), we applied an adapted correction. It accounts for this shorter protostellar time as a non ionised protostar to evaluate the shift in average envelope mass to apply when counting only non ionised high-mass protostars. The detailed of this correction calculated using the model of protostellar evolution of Hosokawa & Omukai (2009) and expressed in Duarte-Cabral et al. (2013) are provided in Appendix D. Also in order to properly sample the two first bins below $16 M_{\odot}$ (i.e. below $8 M_{\odot}$ before doubling mass) we had to consider cores down to $4 M_{\odot}$ for PSC/protostellar classification using CO/SiO outflow detections. We find a total of 48 additional protostellar cores associated with an outflow with masses between 4 and $8 M_{\odot}$.

In Fig. 9 we show that compared to the case of a constant core mass which can correspond to a continuous replenishment of the core mass in a clump-fed view, the number of prestellar cores is now always smaller than the number of protostellar cores. A fraction of 0.3 to 0.5 for mass bins without ionising sources is observed, and this fraction decreases to less than 0.25 above an initial core mass of $16 M_{\odot}$ in the more realistic case which includes the expected number of ionising protostars (yellow histogram and blue, black and brown points). We note that the total number of ionising protostars is of 49 objects, and appears as a reasonable value since the total number of possible ionising sources found in Louvet et al. (2024) was 68 objects. As for Fig. 8 we present in the right panel of Fig. 9 the mean PSC lifetime extracted from the left panel with values presented in Tab. 5. In terms of lifetime in this scenario of a progressive decrease of the core mass as the protostars evolve, we obtain a decrease from ~ 150 kyr to ~ 50 kyr from 4 to $\sim 25 M_{\odot}$ final stellar masses.

7.5. Prestellar lifetimes and free fall times

The obtained HM PSC lifetimes of the order of 100 kyr (see above) are therefore clearly lower than the values measured for low-mass star formation, with a best value of 1.2 Myr in Aquila by Könyves et al. (2015). Such 10 times shorter times confirm that the growth of compact mass reservoirs to form high-mass

¹¹ Since they have some weak free-free emission, they cannot be prestellar cores and were then expected to be driving an outflow.

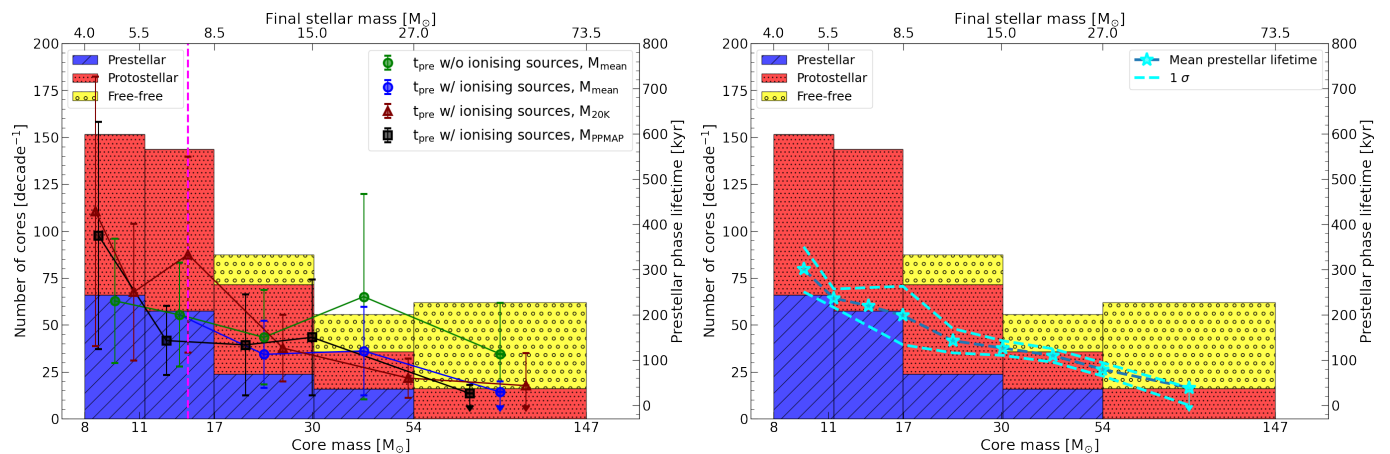


Fig. 8. Left: Weighted histogram of the number of prestellar and protostellar cores per bin and lifetime of the (massive) prestellar phase for each bin (points). The left y-axis indicates the density of number of cores per decade. Prestellar cores are shown in blue bars, protostellar cores in red, and free-free sources in yellow. Bins are built using the average mass adopted in Table 3. Prestellar lifetimes (right y-axis) are presented with green (without ionising sources) and blue (with ionising sources) points for the average mass adopted. We also display with brown and black points the histograms obtained using PSC masses for the lowest and highest dust temperatures respectively we considered in Table 3. The magenta dashed line represents the threshold in mass of the protostar to start ionising its envelope. The upper x axis represent the final stellar mass assuming a core to star efficiency ϵ_{cse} of 50%. **Right:** Same histogram with the mean prestellar lifetime in cyan stars extracted along the range of PSC masses (blue, brown and black points in left panel). Cyan dashed lines represent the one sigma dispersion.

stars has to be faster than that of low-mass stars while having to collect larger amount of material to form high-mass stars. This leads to the need for fast contraction and/or rapid converging flows of gas. Starting from typical densities in dense clumps¹² in the observed protoclusters of $\sim 10^5 \text{ cm}^{-3}$, a $30 M_{\odot}$ sphere has a radius of 0.11 pc, and travelling over 0.11 pc during 10^5 yr leads to a velocity of 1.1 km s^{-1} which is clearly supersonic (at a temperature of 20 K). This velocity of 1.1 km s^{-1} is of the order of magnitude of the observed gas dispersions in the clumps of ALMA-IMF (Cunningham et al. 2023). Moreover, in particular in G353, where we detect one PSC, the previous study by Álvarez-Gutiérrez et al. (2024) shows that this core is located in the kinematically complex convergence point of 3 filaments and near a "V-shape" in position-velocity (PV) space (V-shape "F" in Álvarez-Gutiérrez et al. (2024), see their Table D.1 and Fig. 4). These PV structures are interpreted in this study as cold N_2H^+ inflows onto cores or dense regions in G353. In particular, V-shape F has an associated inflow timescale based on the PV structure of about 63 kyr, broadly consistent with the timescales presented above, and that remains far longer than the t_{ff} estimate for this core (7 kyr, see Tab. 3). This consistency in the contradiction between timescales albeit in one core in G353, derived from completely independent methods, appears remarkable and tends to confirm the results presented here and in Álvarez-Gutiérrez et al. (2024).

The above results are also compatible with the velocities of the so-called converging flows of Csengeri et al. (2011) in Cygnus X for instance (see also Galván-Madrid et al. 2010). At a density of 10^5 cm^{-3} in the clump, the free-fall time is actually ~ 100 kyr which is close to the observed HM PSCs lifetime. In contrast the free-fall times at the scale of the PSCs are much lower than 100 kyr since the average densities have significantly increased. The obtained densities range from $\sim 2 \times 10^6$ to $1.5 \times 10^8 \text{ cm}^{-3}$ leading to free-fall times as low as ~ 3 to 20 kyr (see Table 4). They are more than 10 times lower than the typical observed statistical lifetime we get for these HM PSCs.

¹² Values obtained for the central clumps of for instance G338 or W43-MM2 in Tab.1 of Motte et al. 2022

We have summarized the lifetimes of Fig. 8 and Fig. 9 in several ranges of mass and the corresponding average free-fall times and densities in Table 5.

Table 5. Prestellar phase lifetime.

	Mass range [M_{\odot}]	$\langle n_{\text{H}_2} \rangle^1$ [$\times 10^7 \text{ cm}^{-3}$]	$\langle t_{\text{ff}} \rangle^2$ [kyr]	t_{PSC}^3 [kyr]
Constant protostellar envelope	8 - 16	2.0	7.1	240 [190 - 290]
	16 - 30	3.8	5.1	160 [120 - 200]
	30 - 55	7.0	3.8	100 [80 - 120]
Decreasing protostellar envelope	8 - 16	2.0	7.1	120 [90 - 150]
	16 - 30	3.8	5.1	70 [50 - 90]
	30 - 55	7.0	3.8	50 [40 - 60]

¹ Mean volume density

² Mean free-fall time per bin

³ Mean prestellar lifetime obtained from the right panels of Fig. 8 and 9. The range correspond to the uncertainty obtained from the dispersion of the points.

To further illustrate the relationship between free fall and statistical PSC lifetimes, we have plotted both of them as a function of the core densities in Fig. 10. Each of the green and blue points corresponds to the eight histogram points in the right panels of Fig. 8 and 9. The fourth blue and green points roughly correspond to core mass of $16 M_{\odot}$. The green points are for the clump-fed scenario with a constant core mass over time (continuously refilled by converging flows; Fig. 8 and Sect. 7.2) and suggest very large values of the statistical lifetime over free-fall time ratio with values between 35 and 40 below $16 M_{\odot}$ and between 25 and 30 above $16 M_{\odot}$. The blue points are for the core-fed scenario with a decrease of the core masses along protostellar times (Fig. 9 and Sect. 7.4). They point to lower ratios ranging from 17 to 20 below $16 M_{\odot}$ and between 12 and 15 above $16 M_{\odot}$. We also show with red points the effects of considering a possible decrease of the protostellar lifetime from 300 to 100 kyr for cores masses between 16 and $60 M_{\odot}$ (final stellar masses of 8 to $30 M_{\odot}$) (see Sect. 7.1). This shows that even such a strong

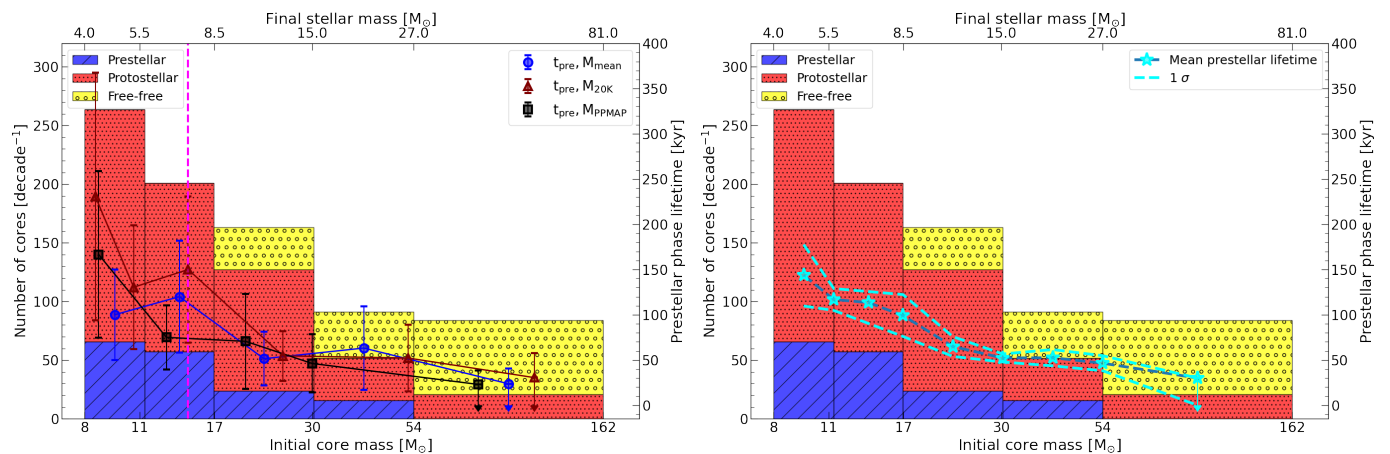


Fig. 9. Left: Weighted histogram of the number of prestellar and protostellar cores per bin (left y-axis) and lifetime of the (massive) prestellar phase (right y-axis) for each bin (points). Prestellar cores are shown in blue bars, protostellar cores in red, and free-free sources in yellow. Bins are constructed using the average mass adopted in Table 3. Protostellar cores masses are corrected assuming a decrease of the core mass envelope over time (see Sect. 7.4), with a constant accretion and a core to star efficiency ϵ_{cse} of 50%. Prestellar lifetimes are presented with blue points for the average mass adopted, black and brown points for the lower and upper mass limits. The magenta dashed line represents the threshold in mass of the protostar to start ionising its envelope. The upper x axis represent the final stellar mass assuming a core to star efficiency ϵ_{cse} of 50%. **Right:** Same histogram with the mean prestellar lifetime in cyan stars extracted from the three hypotheses of left panel. Cyan dashed lines represent the one sigma dispersion.

decrease of the protostellar time would lead to ratios with free-fall times which would still be of the order of 7 to 10.

Altogether with values ranging from 50 to 160 kyr above $16 M_{\odot}$ (last 5 blue and green points) the prestellar lifetimes obtained for high-mass cores are clearly shorter in absolute value than for low mass cores with values of the order of 1 Myr (Andre et al. 2000). In Könyves et al. (2015) the obtained prestellar lifetime of 1.2 Myr at a density of $4 \times 10^4 \text{ cm}^{-3}$ corresponds to a ratio of lifetime over the free-fall time of 8. The prestellar cores in Aquila have however slightly larger sizes (average size of 0.03 pc) than our HM PSC candidates. Assuming a typical linear relationship between the size and the mass of cores, the Aquila value would then shift upward in density by a factor of ~ 5 at a size of 0.013 pc (density scales as size^{-2} when mass scales as size) leading to a ratio of statistical lifetime to free-fall time of ~ 18 very similar to the values we obtain in the high-mass regime.

The ratios of the obtained lifetimes with the free-fall times are therefore surprisingly large with values systematically larger than 10 and reaching values possibly as large as 30. They seem to be relatively similar to what is observed for low-mass PSCs. There is a tendency of a decrease of this ratio for the highest masses above $16 M_{\odot}$ (i.e. $8 M_{\odot}$ for the final stellar mass) but with values which stay above 10. It is only if we would consider that the protostellar lifetime could significantly decrease for the highest masses that we could have values below 10. In order to reach a plausible value of 1 to 2 for the ratio expected for a direct collapse without additional support (see Sect. 7.6 below), one would need to consider a decrease of the protostellar lifetime down to values as low as 20 kyr for the bins of mass we probe here, i.e. for typically $30 M_{\odot}$ final mass star ($60 M_{\odot}$ core mass). This would lead to average accretion rates as large as $1.5 \times 10^{-3} M_{\odot} \text{ yr}^{-1}$ for a $30 M_{\odot}$ star.

7.6. Non thermal supports in dynamical convergent flows

The ratios between the statistical lifetimes and the free-fall times of the cores are surprisingly large. If only thermal support is considered, such compact high-mass cores would collapse roughly

in one or two free-fall times. How can they have a statistical lifetime at least 10 times larger?

If as expected the formation and evolution of the observed prestellar cores have a dynamical origin with converging flows from large scales, one explanation is that the observed cores are dynamical features apparently stable for $\sim 50 - 100$ kyr. They would be collapsing on a free-fall time (typically 5 kyr; see Tab.5) but would be continuously replenished by the large scale flows of infall. In this case one has to understand how we can have a long continuous and strong collapse (typically $30 M_{\odot}$ over each free-fall time of ~ 5 kyr, leads to infall rate of $6 \times 10^{-3} M_{\odot} / \text{yr}$) on such a small scale without having formed yet a single high-mass protostar inside it (then driving a powerful outflow).

Alternatively, the observed HM PSCs have to be significantly regulated and supported by other forces than thermal pressure to keep them that numerous before to further converge/contract or to collapse. In this case, the additional support could also lead to effective Jeans masses large enough to favor high-mass star formation. For instance in the case of turbulent additional support, an effective Jeans mass of $10 M_{\odot}$ would be obtained at all scales from 0.11 down to 0.013 pc (clump to PSC scale) for effective turbulent velocities ranging from 0.7 to 4.5 km s^{-1} respectively. This possible turbulent support can be partly discussed using the line width in DCN(3-2) for some of the detected HM PSCs (see also Cunningham et al. 2023). These line widths are typically ranging from 1 to 2 km s^{-1} . We see that most of these cores have then virial parameter close to 1 or below 1 suggesting turbulence could indeed play a role to support some of the cores (the ones with virial parameters close to or above 1). The complete study of the line widths in different dense gas tracers goes out of the scope of the present work. A forthcoming paper will investigate carefully the complex spectra toward these sources and their surroundings, in different line tracers to draw a complete and reliable view of the possible turbulent support in the cores. Concerning the potential magnetic support, the most recent measurements of B fields intensity in high-mass star forming region tend to point to relatively weak fields not strong enough to prevent collapse (e.g. Sanhueza et al. 2021; Cortés et al. 2021).

On the other hand no measurement could have been done yet on HM PSCs due to the lack of good HM PSC candidates so far. We note however that the ambipolar diffusion time happens to be of the order of 30 times the free-fall time (see [Bergin & Tafalla 2007](#)) i.e. similar to the largest observed lifetimes of the PSCs we discuss here (i.e. in the 8 to 16 M_{\odot} mass regime, see Tab. 5). B-field measurements toward our cores will be invaluable to verify this possibility. We conclude that the tendency to have large statistical lifetimes of HM PSCs suggest that turbulent and magnetic support may act together or alternatively in different cores to statistically indicate a slowing down of or a delay for an immediate collapse. The observed convergent dynamical supersonic flows (e.g. [Schneider et al. 2010](#); [Galván-Madrid et al. 2010](#); [Csengeri et al. 2011](#); [Peretto et al. 2013](#); [Avison et al. 2021](#); [Schneider et al. 2023](#); [Bonne et al. 2023](#)) are expected to concentrate sources of support (magnetic field, rotation and turbulence) leading to some possible stop or braking of the collapse at smaller scales if dispersion/radiation of the related energies/pressures cannot dissipate fast enough. The alternative view of continuously collapsing and replenished cores is more difficult to consider as we would expect a fast formation of at least one high-mass protostars inside the cores which should drive a powerful outflow.

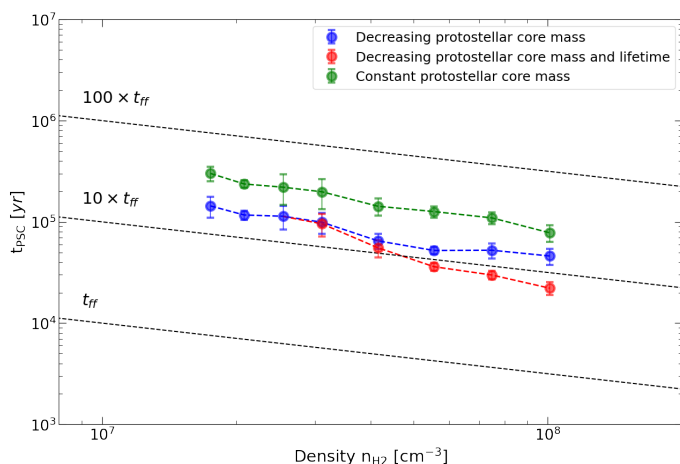


Fig. 10. Statistical lifetime of the prestellar phase as a function of the density. Green points represent the lifetimes and densities extracted from the right panel of Fig. 8, corresponding to the case of a constant protostellar core mass over time (clump-fed). Blue and red points correspond to the case of a decreasing protostellar core mass over time (core-fed). Blue points are extracted from the right panel of Fig. 9, while red points are computed assuming a decreasing protostellar lifetime between 16 M_{\odot} and 60 M_{\odot} , from 300 kyr to 100 kyr. The black dashed lines represent one, ten and a hundred free-fall times.

7.7. Effect of possible sub-fragmentation of the cores

So far in the discussion we assumed that each observed core is the precursor of a single (high-mass) protostar. We only accounted for a certain core to star efficiency ϵ_{cse} (of 50 %) to convert the mass reservoir into a final mass star. Confronted however with the complexity described above of dynamical collapses mediated by turbulence, magnetic field (and some possible angular momentum), one cannot be sure that the observed cores are not fragmenting at lower spatial scales (e.g. [Louvet et al. 2021](#)). The observations of outflows from the high-mass protostars in [Nony et al. \(2020, 2023\)](#) and in the present work mostly point to single outflows coming from the protostellar cores indicating that

the single protostar hypothesis might be mostly correct. On the other hand very recent results of very high resolution ALMA observations of similar high-mass cores have revealed some fragmentation inside the cores with typically 2 to 3 very small scale (typically 500 au) sources which point to a multiplicity of such 2000-3000 au high mass cores ([Budaiev et al. 2024](#); [Li et al. 2024](#); [Olguin et al. 2022](#); [Goddi et al. 2020](#)).

This possible sub-fragmentation of the HM PSCs discussed here does not change our conclusion concerning the prestellar nature of the cores as we defined it in Sect. 5.1. Only the mass will be sub divided into several cores, leading to low-mass prestellar fragments. If some sub-fragments are present inside the cores the non detection of outflows still indicates that there are not yet any strongly accreting objects inside them which would be revealed by a detectable outflow. Concerning the statistical lifetime of the cores the multiplicity would not affect the validity of the number ratios between pre and protostellar cores if the multiplicity level does not change between the two evolutionary stages. This would only move our conclusions lower in final stellar masses (typically from 25 to 12.5 M_{\odot}) obtainable from the present day prestellar mass reservoirs. On the other hand the dynamical fast inflows have no reason to stop to flow, making possible to keep constant the mass reservoirs during the protostellar time (clump-fed scenario corresponding to Sect. 7.3 and Fig. 8). This would allow for increasing the possible final stellar masses. This would also be in line with the protostellar mass evolution proposed to explain evolution of core mass functions in [Nony et al. \(2023\)](#) and [Pouteau et al. \(2023\)](#) (see also [Sanhueza et al. 2019](#)).

7.8. Alternative scenarios

The coincidence of dynamical processes to form the compact cores and of relatively long statistical lifetimes compared to free-fall times appears difficult to explain without the above claim for additional support of magnetic, turbulent or rotational nature. On the other hand our approach relies on the expected strong link between a detectable CO/SiO outflow inside the cores themselves (On-Off criterium) and the expected strong accretion of any high-mass (i.e. highly accreting) protostar in the cores. We can question each of the steps of this link between high accretion and strong CO outflows in the cores. In other words, can our HM PSC candidates hide protostars with large accretion rates?

We list below several alternative scenarios to non-thermal support at the scale of the observed cores:

1. One possibility is that the strong slowing down of the expected collapse does not occur at the presently observed scale of 2700 AU but in smaller fragments similar to those observed in [Budaiev et al. \(2024\)](#) for instance. If at such smaller scale, the fragments stop collapsing due to a strong support of magnetic, turbulent or rotational nature they would not have immediately a strong accretion activity, and would not drive any strong outflows such as the strong outflow observed for instance in a protostellar core of W51-IRS2 in [Goddi et al. \(2020\)](#).
2. A fraction of our HM PSCs could be mis-classified due to a wrong non detection of CO/SiO outflow (false negative outflow detections). A significant fraction of the HM PSC candidates are indeed situated in crowded regions where it is difficult to firmly exclude any outflow driven by a core. This difficulty to firmly reject outflows in crowded regions may however not affect too much statistically our results since at the same time it is difficult to be sure that all protostel-

lar cores we propose are indeed all the driving sources of the observed lobes in the same crowded regions (false positive outflow detections) making them then candidates to be prestellar cores. These false positive outflow detections can compensate, at least partially, for the false negative outflow detections.

3. The direct link between ejection and accretion could also be broken or altered for young high mass protostars. Contrary to what the basic physics of the magneto-centrifugal ejection dictate, this would allow for a high accretion without a strong ejection counterpart. The magneto-centrifugal processes explain the efficient removal of angular momentum, allowing accretion while ejecting material through magnetic mediation. No ejection would then point to no angular momentum to be removed for youngest high-mass protostars. In the here favored dynamical formation processes, the initial angular momentum of dynamically concentrated gas is however certainly larger than in more quasi-static processes which can best evacuate angular momentum during the slow gas concentration for low-mass star formation. Concerning the magnetic field, it is similarly difficult to expect no concentration at all of the magnetic field as the cores form and collapse. Altogether only the existence of so-called dead zones due to non ideal MHD processes or to very low levels of ionisation could be claimed to explain a suppressed magneto-centrifugal ejection/accretion process. But in this case the angular momentum could not be removed and compact rotating cores would then grow rapidly in mass without accretion onto an inner protostar and could then lead to non accreting compact rotating fragments.
4. The expected strong accretion/ejection activity could be variable enough to make that some cores have their CO outflows faded away between two events of accretion to become undetectable. A significant variability of the accretion/ejection is indeed expected. To let a CO outflow disappear between two accretion/ejection events, the time between events has to be large enough. The typical time for a CO outflow to fade away should roughly correspond to the crossing time of the CO gas. Here we typically search for outflows at 6 km s^{-1} for an averaged core radius of $\sim 1350 \text{ au}$. This leads to crossing times of $\sim 1100 \text{ yr}$. This is larger than the typical variability of 500 yr recognized as typical for the CO outflows in W43 by (Nony et al. 2020). This would suggest that strong accretion/ejection has to stop for periods longer than $\sim 1100 \text{ yr}$ at the earliest stages of the high-mass star formation. This is a large value for a stop in accretion for cores which have free-fall times of only $3000 \text{ to } 7000 \text{ yr}$.
5. The expected strong ejection from the hidden high-mass protostars would not interact strongly enough with the compact cores we observed in dust continuum to be detected in CO or SiO at high velocities in the On-Off spectra. This is only possible if the cores are actually mostly empty with the detected dust emission being actually concentrated in even more compact cores. Since most of the high-mass cores we studied are seen as resolved sources with the ALMA beam, this would indicate that they would be made of several such compact cores which would be distant enough from each other to mimic a single resolved core. In this case the strong ejected jets/winds could escape the cores without interacting much with the immediate surroundings.
6. In the case of sub-fragmentation of the cores, the expected large global accretion rate could be spread on several individual low-mass protostars with a reduced global effects of the different outflows driven by these protostars. Since the

rate of momentum carried by outflows is proportional to the accretion rates, the global momentum of the sum of these outflows should be similar to that of a single outflow from a single high-mass protostar. The possible different directions of the outflows could limit the ability to well identify outflows in the maps, but some excess of high-velocity CO gas should be detectable towards the cores in the spectra.

Altogether we therefore see that possible alternative scenarios to a turbulent, magnetic or rotational support at the core scale exist and will need to be further investigated in the future. The main limitation of the present work is related to the still possible misclassification of cores as prestellar due to the difficulty to assure a non-detection of an outflow in the most crowded regions. It would be extremely valuable to further search for protostellar activity from the cores using mid-IR emission at high spatial resolution with the JWST/MIRI to validate their prestellar nature. We will also further study this unique sample of HM PSC candidates using detailed molecular line observations from ALMA-IMF (Vaileille-Manet et al. in prep) and will gather new high spatial resolution ALMA studies both in line and continuum to investigate possible existence and effects of fragmentation of the cores.

8. Conclusions

We used the core catalog of Louvet et al. (2024), extracted from the continuum, combined with CO (J=2–1) and SiO (J=5–4) datacubes of the large program ALMA-IMF to identify a sample of high-mass prestellar cores in 14 protoclusters. Our main results are :

1. We built a new automated method combining spectral information with the comparison of On and Off spectra and spatial information with molecular outflow maps to identify outflowing emission from compact cores. Our method is efficient at detecting outflows from protostellar cores and has proved essential for clarifying the classification of cores in the most clustered regions where outflows overlap, and is particularly adapted to systematic analysis of large CO/SiO data cubes.
2. Using this method, we identified for the first time a significant sample of robust high-mass PSC candidates inside a single survey, with masses reaching up to $50 M_{\odot}$ as a mass reservoir and which may then form stars as massive as $25 M_{\odot}$ (for a core to star mass efficiency of 50 %).
3. From 82 cores above $8 M_{\odot}$, we identify 30 cores that do not have any detectable outflow with the current data and methodology used. Of these 30 cores, 12 are more massive than $16 M_{\odot}$, the most massive core being $54 M_{\odot}$. These 30 PSC candidates range from $1350 \text{ to } 4200 \text{ au}$ in deconvolved FWHM size, and are all high density cores between $\sim 4 \times 10^6 \text{ cm}^{-3}$ and $\sim 1.5 \times 10^8 \text{ cm}^{-3}$.
4. We found that most of the robust HM PSC candidates are located in the central clump regions where most of the mass is most probably dynamically gathered. We propose that it is mostly the difficulty to identify cores without outflows in such highly clustered environments which explains why so few high-mass PSCs could be identified so far.
5. Adopting a high-mass protostellar lifetime of 300 kyr , we could estimate the lifetime of the high-mass prestellar phase in several mass bins. We ended up with a range of most plausible statistical lifetimes between $8 \text{ and } 16 M_{\odot}$ of $150 \text{ to } 250 \text{ kyr}$ with a trend of decrease to $50 \text{ to } 100 \text{ kyr}$ between $16 \text{ and } 40\text{-}50 M_{\odot}$.

6. The surprisingly large ratios (10 to 30) of HM PSC lifetimes with their free-fall times strongly point to the need for non thermal support of the observed cores. Such support can either be turbulent, magnetic, or rotational in nature. Further studies are required to find out what is the best scenario to precisely account for these large timescale ratios.

These results confirm the extreme rarity of HM PSCs with only 12 candidates above $16 M_{\odot}$ found in 14 very active proto-clusters of the Galaxy where hundreds of cores have been recognized, with only four of them more massive than $30 M_{\odot}$.

Acknowledgements. We thank the referee for the careful reading of the manuscript and for providing useful comments. This paper makes use of the following ALMA data: ADS/JAO.ALMA#2017.1.01355.L. ALMA is a partnership of ESO (representing its member states), NSF (USA) and NINS (Japan), together with NRC (Canada), MOST and ASIAA (Taiwan), and KASI (Republic of Korea), in cooperation with the Republic of Chile. The Joint ALMA Observatory is operated by ESO, AUI/NRAO and NAOJ. This work was supported by the Programme National "Physique et Chimie du Milieu Interstellaire" (PCMI) of CNRS/INSU with INC/INP co-funded by CEA and CNES. This work was supported by the "Programme National de Physique Stellaire" (PNPS) of CNRS/INSU co-funded by CEA and CNES. T.Cs. and M.B. acknowledge support from the French State in the framework of the IdEx Université de Bordeaux Investments for the future Program. AS gratefully acknowledges support by the Fondecyt Regular (project code 1220610), and ANID BASAL project FB210003. AG acknowledges support from the NSF under grants AST 2008101 and CAREER 2142300. R.G.M. acknowledges support from UNAM-PAPIIT project IN108822 and from CONACyT Ciencia de Frontera project ID 86372. PS was partially supported by a Grant-in-Aid for Scientific Research (KAKENHI Number JP22H01271 and JP23H01221) of JSPS. R.A. gratefully acknowledges support from ANID Beca Doctorado Nacional 21200897. LB gratefully acknowledges support by ANID Basal project FB210003.

References

- Álvarez-Gutiérrez, R. H., Stutz, A. M., Sandoval-Garrido, N., et al. 2024, *A&A*, 689, A74
- Andre, P., Ward-Thompson, D., & Barsony, M. 1993, *ApJ*, 406, 122
- Andre, P., Ward-Thompson, D., & Barsony, M. 2000, in *Protostars and Planets IV*, ed. V. Mannings, A. P. Boss, & S. S. Russell, 59
- Anglada, G. 1996, in *Astronomical Society of the Pacific Conference Series*, Vol. 93, *Radio Emission from the Stars and the Sun*, ed. A. R. Taylor & J. M. Paredes, 3–14
- Armante, M., Gusdorf, A., Louvet, F., et al. 2024, *A&A*, 686, A122
- Avison, A., Fuller, G. A., Peretto, N., et al. 2021, *A&A*, 645, A142
- Barnes, A. T., Liu, J., Zhang, Q., et al. 2023, *A&A*, 675, A53
- Beichman, C. A., Myers, P. C., Emerson, J. P., et al. 1986, *ApJ*, 307, 337
- Bergin, E. A. & Tafalla, M. 2007, *ARA&A*, 45, 339
- Beuther, H., Schilke, P., Sridharan, T. K., et al. 2002, *A&A*, 383, 892
- Bhandare, A., Kuiper, R., Henning, T., et al. 2018, *A&A*, 618, A95
- Blandford, R. D. & Payne, D. G. 1982, *MNRAS*, 199, 883
- Bonfand, M., Csengeri, T., Bontemps, S., et al. 2024, *A&A*, 687, A163
- Bonne, L., Bontemps, S., Schneider, N., et al. 2023, *ApJ*, 951, 39
- Bonnell, I. A., Bate, M. R., Clarke, C. J., & Pringle, J. E. 2001, *MNRAS*, 323, 785
- Bontemps, S., Andre, P., Terebey, S., & Cabrit, S. 1996, *A&A*, 311, 858
- Bontemps, S., Motte, F., Csengeri, T., & Schneider, N. 2010, *A&A*, 524, A18
- Bouscasse, L., Csengeri, T., Belloche, A., et al. 2022, *A&A*, 662, A32
- Brouillet, N., Despois, D., Molet, J., et al. 2022, *A&A*, 665, A140
- Budaiev, N., Ginsburg, A., Jeff, D., et al. 2024, *ApJ*, 961, 4
- Cabrit, S. & Bertout, C. 1992, *A&A*, 261, 274
- Commerçon, B., González, M., Mignon-Risse, R., Hennebelle, P., & Vaytet, N. 2022, *A&A*, 658, A52
- Contreras, Y., Sanhueza, P., Jackson, J. M., et al. 2018, *ApJ*, 861, 14
- Cortés, P. C., Sanhueza, P., Houde, M., et al. 2021, *ApJ*, 923, 204
- Csengeri, T., Belloche, A., Bontemps, S., et al. 2019, *A&A*, 632, A57
- Csengeri, T., Bontemps, S., Schneider, N., et al. 2011, *ApJ*, 740, L5
- Csengeri, T., Bontemps, S., Wyrowski, F., et al. 2018, *A&A*, 617, A89
- Csengeri, T., Bontemps, S., Wyrowski, F., et al. 2017, *A&A*, 601, A60
- Csengeri, T., Urquhart, J. S., Schuller, F., et al. 2014, *A&A*, 565, A75
- Cunningham, N., Ginsburg, A., Galván-Madrid, R., et al. 2023, *A&A*, 678, A194
- Cunningham, N., Lumsden, S. L., Cyganowski, C. J., Maud, L. T., & Purcell, C. 2016, *MNRAS*, 458, 1742
- Cyganowski, C. J., Brogan, C. L., Hunter, T. R., et al. 2014, *ApJ*, 796, L2
- Cyganowski, C. J., Ilee, J. D., Brogan, C. L., et al. 2022, *ApJ*, 931, L31
- Dell’Ova, P., Motte, F., Gusdorf, A., et al. 2024, *A&A*, 687, A217
- Duarte-Cabral, A., Bontemps, S., Motte, F., et al. 2013, *A&A*, 558, A125
- Ferreira, J., Dougados, C., & Cabrit, S. 2006, *A&A*, 453, 785
- Furlan, E., Fischer, W. J., Ali, B., et al. 2016, *ApJS*, 224, 5
- Galván-Madrid, R., Ginsburg, A., & et al., sub., *A&A*
- Galván-Madrid, R., Zhang, Q., Keto, E., et al. 2010, *ApJ*, 725, 17
- Ginsburg, A., Csengeri, T., Galván-Madrid, R., et al. 2022, *A&A*, 662, A9
- Goddi, C., Ginsburg, A., Maud, L. T., Zhang, Q., & Zapata, L. A. 2020, *ApJ*, 905, 25
- Gusdorf, A., Cabrit, S., Flower, D. R., & Pineau Des Forêts, G. 2008, *A&A*, 482, 809
- Gutermuth, R. A., Megeath, S. T., Myers, P. C., et al. 2009, *ApJS*, 184, 18
- Hosokawa, T. & Omukai, K. 2009, *ApJ*, 691, 823
- Jessop, N. E. & Ward-Thompson, D. 2000, *MNRAS*, 311, 63
- Jorsater, S. & van Moorsel, G. A. 1995, *AJ*, 110, 2037
- Keto, E. 2007, *ApJ*, 666, 976
- Kölligan, A. & Kuiper, R. 2018, *A&A*, 620, A182
- Kong, S., Tan, J. C., Caselli, P., et al. 2017, *ApJ*, 834, 193
- Könyves, V., André, P., Men’shchikov, A., et al. 2015, *A&A*, 584, A91
- Krumholz, M. R., Klein, R. I., & McKee, C. F. 2007, *ApJ*, 656, 959
- Lada, C. J. & Adams, F. C. 1992, *ApJ*, 393, 278
- Launhardt, R., Stutz, A. M., Schmiedeke, A., et al. 2013, *A&A*, 551, A98
- Li, S., Sanhueza, P., Beuther, H., et al. 2024, *Nature Astronomy*, 8, 472
- Li, S., Sanhueza, P., Zhang, Q., et al. 2020, *ApJ*, 903, 119
- Louvet, F., Hennebelle, P., Men’shchikov, A., et al. 2021, *A&A*, 653, A157
- Louvet, F., Neupane, S., Garay, G., et al. 2019, *A&A*, 622, A99
- Louvet, F., Sanhueza, P., Stutz, A., et al. 2024, *A&A*, 690, A33
- Mai, X., Liu, T., Liu, X., et al. 2024, *ApJ*, 961, L35
- Matsushita, Y., Machida, M. N., Sakurai, Y., & Hosokawa, T. 2017, *MNRAS*, 470, 1026
- Maud, L. T., Moore, T. J. T., Lumsden, S. L., et al. 2015, *MNRAS*, 453, 645
- McKee, C. F. & Tan, J. C. 2003, *ApJ*, 585, 850
- Men’shchikov, A. 2021, *A&A*, 649, A89
- Mignon-Risse, R., González, M., & Commerçon, B. 2021, *A&A*, 656, A85
- Molet, J., Brouillet, N., Nony, T., et al. 2019, *A&A*, 626, A132
- Morii, K., Sanhueza, P., Nakamura, F., et al. 2023, *ApJ*, 950, 148
- Motte, F., Andre, P., & Neri, R. 1998, *A&A*, 336, 150
- Motte, F., Bontemps, S., Csengeri, T., et al. 2022, *A&A*, 662, A8
- Motte, F., Bontemps, S., & Louvet, F. 2018a, *ARA&A*, 56, 41
- Motte, F., Bontemps, S., Schilke, P., et al. 2007, *A&A*, 476, 1243
- Motte, F., Nony, T., Louvet, F., et al. 2018b, *Nature Astronomy*, 2, 478
- Motte, F., Zavagno, A., Bontemps, S., et al. 2010, *A&A*, 518, L77
- Mottram, J. C., Hoare, M. G., Davies, B., et al. 2011, *ApJ*, 730, L33
- Myers, P. C., Linke, R. A., & Benson, P. J. 1983, *ApJ*, 264, 517
- Nguyen-Luong, Q., Anderson, L. D., Motte, F., et al. 2017, *ApJ*, 844, L25
- Nony, T., Galván-Madrid, R., Brouillet, N., et al. 2024, *A&A*, 687, A84
- Nony, T., Galván-Madrid, R., Motte, F., et al. 2023, *A&A*, 674, A75
- Nony, T., Louvet, F., Motte, F., et al. 2018, *A&A*, 618, L5
- Nony, T., Motte, F., Louvet, F., et al. 2020, *A&A*, 636, A38
- Olguin, F. A., Sanhueza, P., Chen, H.-R. V., et al. 2023, *ApJ*, 959, L31
- Olguin, F. A., Sanhueza, P., Ginsburg, A., et al. 2022, *ApJ*, 929, 68
- Ossenkopf, V. & Henning, T. 1994, *A&A*, 291, 943
- Padoan, P. & Nordlund, Å. 2002, *ApJ*, 576, 870
- Peretto, N., Fuller, G. A., Duarte-Cabral, A., et al. 2013, *A&A*, 555, A112
- Peretto, N., Rigby, A., André, P., et al. 2020, *MNRAS*, 496, 3482
- Peters, T., Banerjee, R., Klessen, R. S., et al. 2010, *ApJ*, 711, 1017
- Pouteau, Y., Motte, F., Nony, T., et al. 2022, *A&A*, 664, A26
- Pouteau, Y., Motte, F., Nony, T., et al. 2023, *A&A*, 674, A76
- Redaelli, E., Bovino, S., Sanhueza, P., et al. 2022, *ApJ*, 936, 169
- Sánchez-Monge, Á., Schilke, P., Ginsburg, A., Cesaroni, R., & Schmiedeke, A. 2018, *A&A*, 609, A101
- Sanhueza, P., Contreras, Y., Wu, B., et al. 2019, *ApJ*, 886, 102
- Sanhueza, P., Girart, J. M., Padovani, M., et al. 2021, *ApJ*, 915, L10
- Sanhueza, P., Jackson, J. M., Zhang, Q., et al. 2017, *ApJ*, 841, 97
- Schneider, N., Bonne, L., Bontemps, S., et al. 2023, *Nature Astronomy*, 7, 546
- Schneider, N., Csengeri, T., Bontemps, S., et al. 2010, *A&A*, 520, A49
- Stutz, A. M. & Gould, A. 2016, *A&A*, 590, A2
- Tan, J., Beltrán, M. T., & Caselli, P. e. a. 2014, 149
- Tan, J. C., Kong, S., Butler, M. J., Caselli, P., & Fontani, F. 2013, *ApJ*, 779, 96
- Tan, J. C., Kong, S., Zhang, Y., et al. 2016, *ApJ*, 821, L3
- Tanaka, K. E. I., Tan, J. C., & Zhang, Y. 2016, *ApJ*, 818, 52
- Tigé, J., Motte, F., Russeil, D., et al. 2017, *A&A*, 602, A77
- Towner, A. P. M., Ginsburg, A., Dell’Ova, P., et al. 2024, *ApJ*, 960, 48
- Wang, K., Zhang, Q., Testi, L., et al. 2014, *MNRAS*, 439, 3275
- Xu, F., Wang, K., Liu, T., et al. 2024, *ApJS*, 270, 9
- Yorke, H. W. & Sonnhalter, C. 2002, *ApJ*, 569, 846

-
- ¹ Laboratoire d'astrophysique de Bordeaux, Univ. Bordeaux, CNRS, B18N, allée Geoffroy Saint-Hilaire, 33615 Pessac, France
 - ² Instituto de Radioastronomía y Astrofísica, Universidad Nacional Autónoma de México, Morelia, Michoacán 58089, México
 - ³ INAF-Osservatorio Astrofisico di Arcetri, Largo E. Fermi 5, I-50125 Firenze, Italy
 - ⁴ Univ. Grenoble Alpes, CNRS, IPAG, 38000 Grenoble, France
 - ⁵ Departamento de Astronomía, Universidad de Concepción, Casilla 160-C, 4030000 Concepción, Chile
 - ⁶ Laboratoire de Physique de l'École Normale Supérieure, ENS, Université PSL, CNRS, Sorbonne Université, Université de Paris, Paris, France
 - ⁷ Observatoire de Paris, PSL University, Sorbonne Université, LERMA, 75014, Paris, France
 - ⁸ Department of Astronomy, University of Florida, PO Box 112055, USA
 - ⁹ Departments of Astronomy and Chemistry, University of Virginia, Charlottesville, VA 22904, USA
 - ¹⁰ SKA Observatory, Jodrell Bank, Lower Withington, Macclesfield SK11 9FT, United Kingdom
 - ¹¹ Instituto Argentino de Radioastronomía (CCT-La Plata, CONICET; CICPBA), C.C. No. 5, 1894, Villa Elisa, Buenos Aires, Argentina
 - ¹² Department of Astronomical Science, SOKENDAI (The Graduate University for Advanced Studies), 2-21-1 Osawa, Mitaka, Tokyo 181-8588, Japan
 - ¹³ The Graduate University for Advanced Studies (SOKENDAI), 2-21-1 Osawa, Mitaka, Tokyo 181-0015, Japan
 - ¹⁴ Joint Alma Observatory (JAO), Alonso de Córdova 3107, Vitacura, Santiago, Chile
 - ¹⁵ Max Planck Institute for Radio Astronomy, Auf dem Hügel 69, 53121 Bonn, Germany
 - ¹⁶ Department of Astronomy, Universidad de Chile, Camino El Observatorio 1515, Santiago, Chile.
 - ¹⁷ Franco-Chilean Laboratory for Astronomy, IRL 3386, CNRS and Universidad de Chile, Santiago, Chile.

Appendix A: On and Off spectra computation method

Figure A.1 shows the two different cases for On and Off spectra computation. Top panel presents the continuum cores #2 and #3 of G353.41 overlaid on the 1.3mm continuum map in grey scale, and the computation of the On and Off spectra in the ellipses and annulus of the cores are presented in the middle and bottom panels. Core #2 has another source crossing its annulus causing the pixels overlapping to be subtracted from the background annulus.

Figure A.2 presents the obtained SiO (5–4) spectra for cores #3 and #30 of the W43-MM2 region, which are presented in Fig. 1.

Appendix B: Noise estimation

Figure B.1 presents an example of the method used to estimate the noise in the ALMA-IMF datacubes. Figure B.2 presents the derived mean and standard deviation of the noise levels of the CO and SiO/DCN datacubes (i.e. over all velocities of the spectral windows), in the 14 ALMA-IMF regions.

Appendix C: List of protostellar core candidates

Here we present the 100 cores of Louvet et al. (2024) with $M > 4M_{\odot}$ classified as protostellar core candidates due to an association with an outflow. They are listed in Table C.1 with their host region, number, coordinates (ICRS), mass, temperature and size. To compute their masses the same PPMAP temperatures as in Louvet et al. (2024) were used. The error on the masses are computed by taking into account only the uncertainties on the integrated and peak fluxes.

Appendix D: Correction of the masses of the protostellar cores using ionising models

Here we present the correction applied to the observed protostellar cores masses in order to estimate their initial prestellar mass reservoir. We assume a constant accretion and a core to star efficiency (ϵ_{cse}) of 50%. As we work on core catalogs with ionising protostars removed, we can assume that on average we observe protostellar cores at half of their non-ionising part life (i.e. while the protostar is accreting to reach the mass ionising threshold). Using the models from Hosokawa & Omukai (2009) as in Duarte-Cabral et al. (2013), we can infer the fraction of time each protostellar core is going to pass in the ionising phase in function of the final mass of the protostar. Then we correct from half of the mass lost during the non-ionising accretion time to obtain the initial mass reservoir of the protostellar core. In practice this correction doubles the mass of protostellar cores with protostars not massive enough to ionise their envelope, while the correction factor is lower than two for protostars that will be ionising for part of their protostellar lifetime. In Fig. D.1 we present the fraction of the non-ionising protostellar lifetime as function of the final stellar mass, and the non-ionising protostellar lifetime as function of the initial prestellar mass reservoir.

Appendix E: Massive prestellar core candidates figures

In this section we present the CO and SiO spectra and the individual molecular outflows maps of every candidate of the survey

used to classify them as prestellar. The On and On-Off DCN spectra are also presented with the fit adopted to estimate the V_{LSR} of each candidate.

Appendix F: Location of the prestellar candidates in the ALMA-IMF regions

Figure F.1 presents the fourteen ALMA-IMF fields with the prestellar cores candidates highlighted in blue with their number. The red and orange cores are all the high-mass and intermediate mass cores above which have been studied and have been associated to an outflow (i.e. protostellar cores). The green cores remaining are all the cores which have not been classified.

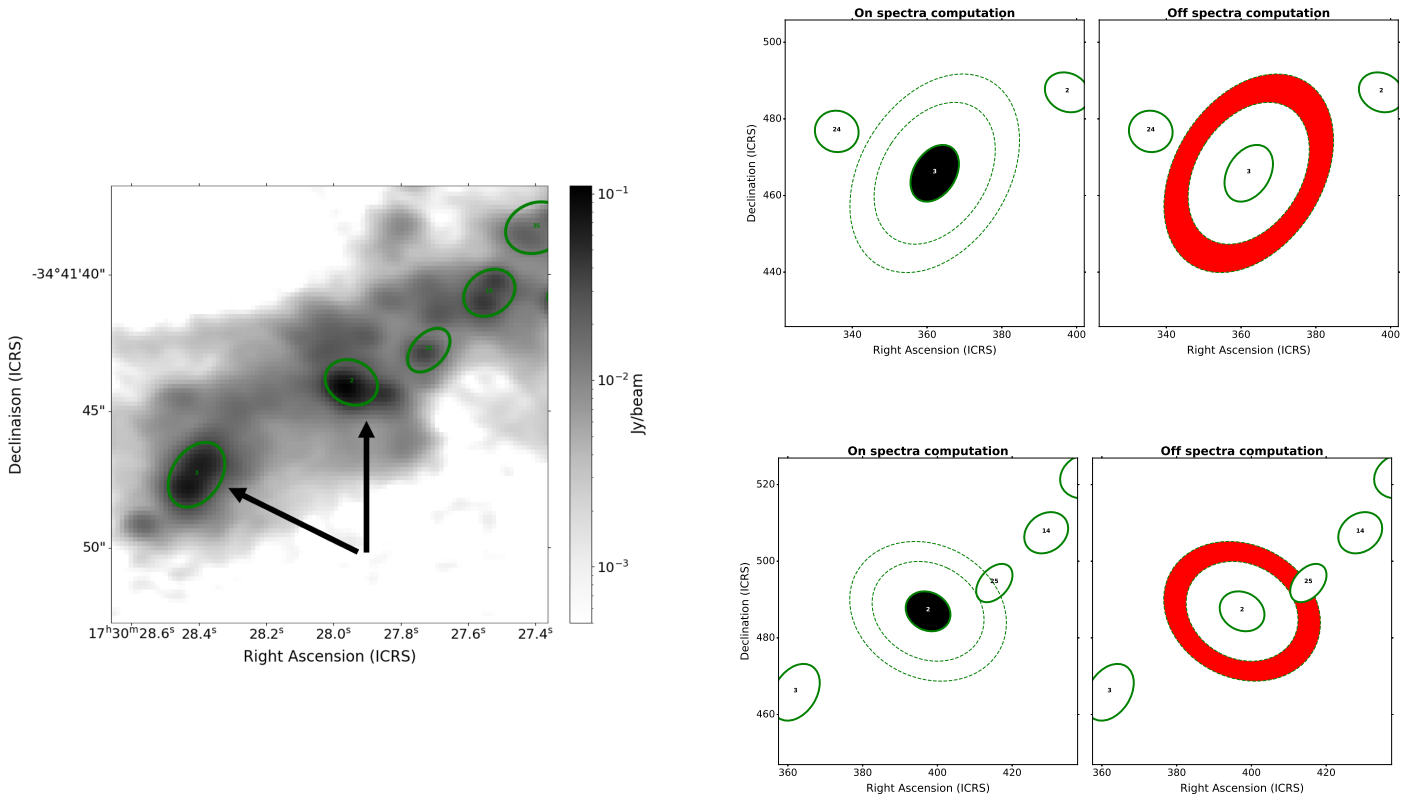


Fig. A.1. **Left:** Zoom on the continuum core #2 (top right) and #3 (bottom left) overlaid on the 1.3mm continuum map of G353.41 (in gray scale). The green ellipses represent 1 time the FWHM of the continuum core. **Right:** Example of the On (black ellipse) and Off (red annulus) spectra computation for each core, used to estimate the core-averaged background-subtracted spectra. Core #3 (top) is the simplest case where no other core overlaps with its annulus (computed between 2.5 and 3.5 times the FWHM of the continuum core). Core #2 (bottom) has another core overlapping its annulus. The overlapping pixels are subtracted from the background estimation.

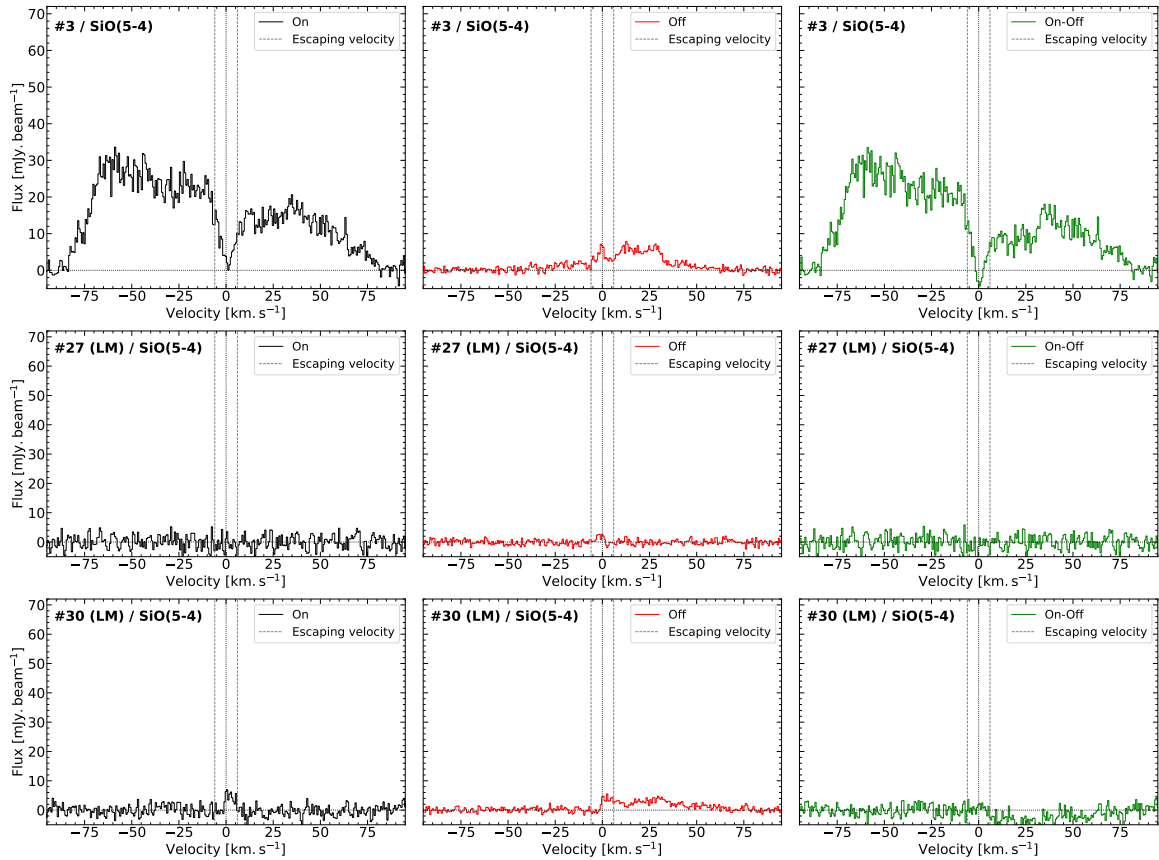


Fig. A.2. Resulting SiO(5-4) spectra for cores #3, #27 and #30 of the W43-MM2 region, presented in Fig. 1.

Table C.1. List and properties of the sample of protostellar core candidates with $M > 4M_{\odot}$.

Region	Source	RA [deg]	DEC [deg]	Mass ¹ [M_{\odot}]	Temperature ² [K]	FWHM ^{dec} [au]
G008.67	#3	271.5796091	-21.6250348	8.5 ± 0.7	35	1340
G008.67	#5	271.5785345	-21.6222306	4.9 ± 0.2	25	2000
G010.62	#8	272.6185252	-19.9301787	8.0 ± 1.0	44	1360
G010.62	#14	272.6213499	-19.9296433	7.0 ± 0.6	40	2970
G010.62	#16	272.6207417	-19.929286	4.7 ± 0.6	41	1630
G010.62	#24	272.6222764	-19.930054	4.9 ± 0.5	36	3040
G012.80	#1	273.5493292	-17.9256817	6.1 ± 0.1	100	1850
G012.80	#3	273.5573504	-17.9225106	5.3 ± 0.1	100	2960
G012.80	#6	273.5531484	-17.9208183	4.4 ± 0.1	33	1680
G012.80	#8A*	273.5487793	-17.9261916	6.8 ± 0.3	31	2120
G012.80	#8B*	273.5484473	-17.9261587	6.4 ± 0.2	31	1910
G012.80	#11	273.5547682	-17.9278997	9.8 ± 1.4	42	2590
G327.29	#1	238.282335	-54.618403	49.6 ± 0.2	300	4550
G327.29	#2A*	238.2893669	-54.6167726	15.2 ± 0.3	32	2040
G327.29	#2B*	238.2895574	-54.616967	9.2 ± 0.2	32	1270
G327.29	#3	238.280656	-54.6186811	9.5 ± 0.3	42	2760
G327.29	#5	238.2955904	-54.6128047	11.7 ± 0.3	28	2850
G327.29	#6	238.2938644	-54.6110507	4.9 ± 0.2	28	1390
G327.29	#7	238.2961992	-54.6133521	8.5 ± 0.4	26	2610
G327.29	#8	238.2983074	-54.6069915	4.3 ± 0.3	27	1590
G327.29	#9	238.2858254	-54.6172552	4.0 ± 0.4	36	1590
G328.25	#1	239.4991778	-53.9668493	11.3 ± 0.1	100	2240
G333.60	#2	245.5356169	-50.104813	12.7 ± 0.3	41	2290
G333.60	#3	245.528392	-50.1050657	5.8 ± 0.3	36	2080
G333.60	#4	245.5460571	-50.0990531	4.7 ± 0.3	100	1500
G333.60	#5	245.5285258	-50.1045541	4.7 ± 0.4	36	1420
G333.60	#7	245.5370048	-50.1027976	16.8 ± 0.7	46	3840
G333.60	#11	245.5357042	-50.1033887	5.2 ± 0.3	100	4390
G333.60	#62	245.5358049	-50.1009901	7.7 ± 1.4	45	3660
G337.92	#1	250.2935548	-47.1342727	23.0 ± 0.4	100	2670
G337.92	#2	250.2936172	-47.133748	19.6 ± 0.7	48	3140
G337.92	#8	250.2927529	-47.1352673	4.4 ± 0.6	39	2360
G337.92	#9	250.294383	-47.1348356	4.3 ± 0.8	40	2890
G338.93	#1	250.1422011	-45.6934028	12.9 ± 0.1	100	1870
G338.93	#2	250.1427268	-45.6936217	12.4 ± 0.1	100	1880
G338.93	#3	250.1417044	-45.7020244	7.6 ± 0.1	100	1750
G338.93	#4	250.1397543	-45.6936984	6.2 ± 0.1	100	1870
G338.93	#6	250.1419183	-45.7022799	15.5 ± 0.4	40	2400
G338.93	#8	250.1433977	-45.6938542	11.8 ± 0.3	27	3420
G353.41	#2	262.6165032	-34.6955865	12.3 ± 0.7	29	2300
G353.41	#8	262.6039531	-34.6936374	4.6 ± 0.2	26	2630
W43-MM1	#1	281.9459334	-1.9074736	72.4 ± 0.6	100	2470
W43-MM1	#2	281.9451648	-1.9081343	28.7 ± 0.7	100	1770
W43-MM1	#3	281.9432069	-1.9092736	20.3 ± 0.3	100	2550
W43-MM1	#4	281.945748	-1.9073463	35.4 ± 0.5	100	3460
W43-MM1	#5	281.9469228	-1.908243	24.4 ± 0.3	26	1550
W43-MM1	#7	281.9438998	-1.9064175	7.4 ± 0.2	100	1910
W43-MM1	#9	281.9448606	-1.9086666	6.3 ± 0.3	100	1860

Bold font is used to present protostellar core candidates with $M > 16M_{\odot}$.

¹ Mass of the protostellar core candidates obtained with the PPMAP $70\mu\text{m}$ corrected dust temperatures (see Dell'Ova et al. 2024).

² PPMAP $70\mu\text{m}$ corrected dust temperatures (see Dell'Ova et al. 2024).

* These sources were found to be multiple using the GExt2D second derivative map. The sizes and masses are computed using the ellipses parameters and fluxes of the GExt2D catalogs.

Table C.1. Continued.

Region	Source	RA [deg]	DEC [deg]	Mass [M_{\odot}]	Temperature [K]	FWHM ^{dec} [au]
W43-MM1	#13	281.9427046	-1.9092745	10.7 ± 0.6	26	2060
W43-MM1	#16	281.9372707	-1.9118969	5.0 ± 0.3	25	1890
W43-MM1	#20	281.9456983	-1.9036124	8.4 ± 0.4	24	4840
W43-MM1	#24	281.9440629	-1.9089	12.3 ± 1.4	26	1760
W43-MM1	#29	281.9460739	-1.9089351	4.6 ± 0.9	25	1350
W43-MM1	#37	281.9454183	-1.9067383	6.3 ± 1.1	28	1590
W43-MM1	#40	281.9440532	-1.9057986	4.5 ± 0.5	26	3060
W43-MM1	#42	281.9455026	-1.9079514	4.9 ± 1.3	31	1350
W43-MM2	#1	281.9033208	-2.0150752	40.9 ± 0.3	100	3000
W43-MM2	#3	281.9004197	-2.0210949	18.4 ± 0.3	25	3460
W43-MM2	#5	281.9011837	-2.0141012	8.1 ± 0.2	27	1940
W43-MM2	#6	281.9031379	-2.0149264	24.3 ± 0.5	37	3180
W43-MM2	#8	281.8962619	-2.0191026	4.6 ± 0.1	23	1820
W43-MM2	#10	281.9135971	-2.0078124	21.3 ± 0.6	29	3250
W43-MM2	#13	281.9028491	-2.0133518	6.0 ± 0.2	28	2120
W43-MM2	#26	281.9038579	-2.0152273	4.1 ± 0.3	31	3720
W43-MM3	#1	281.9238036	-2.0079434	7.3 ± 0.2	100	1570
W43-MM3	#4	281.9238914	-2.0076105	8.2 ± 0.5	33	1350
W43-MM3	#6	281.9234345	-2.007048	5.4 ± 0.5	32	2130
W43-MM3	#10	281.924284	-2.008162	4.2 ± 0.5	31	2840
W51-E	#2	290.9331854	14.5095896	87.9 ± 0.6	300	3740
W51-E	#4	290.9329076	14.5078281	147.0 ± 6.7	100	3280
W51-E	#5[†]	290.9328333	14.5099861	86.4 ± 3.1	59	3910
W51-E	#8	290.9330369	14.5101522	55.8 ± 3.3	54	3840
W51-E	#9[†]	290.9426667	14.4964278	27.8 ± 2.2	24	3240
W51-E	#12	290.933288	14.5091267	16.0 ± 1.5	49	3730
W51-E	#13	290.9324479	14.5054808	17.1 ± 3.4	32	2830
W51-E	#15	290.9315055	14.5099588	10.9 ± 0.8	29	3770
W51-E	#16	290.9327544	14.5073581	12.5 ± 5.5	53	2340
W51-E	#19	290.9327315	14.5112086	6.0 ± 1.0	27	1350
W51-E	#22	290.9277814	14.500986	4.1 ± 0.4	23	2970
W51-E	#29	290.9296394	14.5149377	7.5 ± 0.9	24	4520
W51-E	#34	290.9325349	14.5131101	6.6 ± 0.6	23	4730
W51-IRS2	#1	290.9168699	14.5181896	57.8 ± 0.7	300	2550
W51-IRS2	#2	290.9164704	14.5181596	50.4 ± 1.4	100	1870
W51-IRS2	#4	290.9107235	14.5116053	16.9 ± 0.2	100	2410
W51-IRS2	#5[†]	290.9159167	14.5180806	67.6 ± 2.9	60	2480
W51-IRS2	#6	290.916647	14.5182923	49.5 ± 1.4	100	2730
W51-IRS2	#7	290.9156148	14.5181323	18.6 ± 1.1	100	2020
W51-IRS2	#10	290.9111836	14.5126596	8.0 ± 0.3	31	1510
W51-IRS2	#13	290.9059966	14.5052314	21.8 ± 0.6	20	2220
W51-IRS2	#14	290.9091924	14.5092115	6.1 ± 0.4	31	1770
W51-IRS2	#15	290.9100189	14.510189	11.4 ± 0.5	31	3720
W51-IRS2	#27	290.9083688	14.5198952	4.2 ± 0.1	28	5390
W51-IRS2	#33	290.9235087	14.5171682	4.7 ± 0.3	34	3150
W51-IRS2	#41	290.9161814	14.5181418	13.3 ± 1.9	62	2720
W51-IRS2	#49	290.9114383	14.5127072	4.3 ± 0.3	31	3370
W51-IRS2	#60	290.911816	14.5117357	5.9 ± 0.5	30	4860
W51-IRS2	#68	290.9149185	14.5178211	4.1 ± 0.7	45	2980
W51-IRS2	#76	290.9074011	14.506935	4.5 ± 0.5	27	2020
W51-IRS2	#81	290.9082835	14.5082754	5.4 ± 0.3	27	5180

[†] These sources were initially considered as free-free sources by Louvet et al. (2024), but were added here to the protostellar sample due to their spectral index close to two and their association to an outflow.

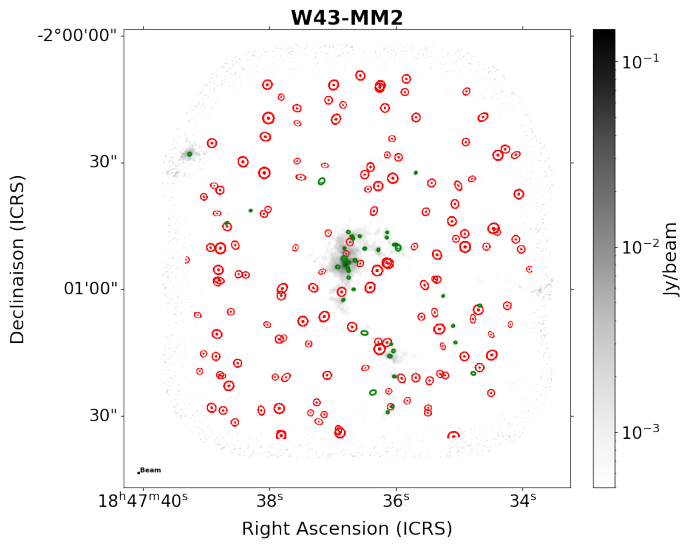


Fig. B.1. W43-MM2 field with in green ellipses the ALMA-IMF cores, and in red the 150 On and Off random selections. The grey background represents the 1.3mm dust continuum.

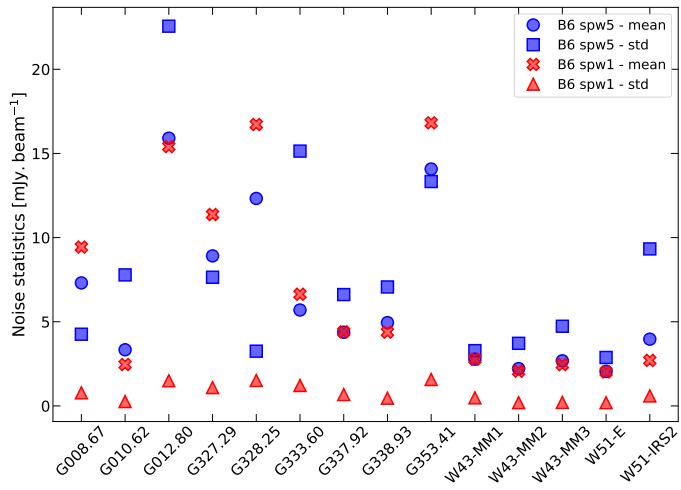


Fig. B.2. Mean and standard deviation of the derived rms noise levels in B6 spw1 and B6 spw5, for the 14 ALMA-IMF fields.

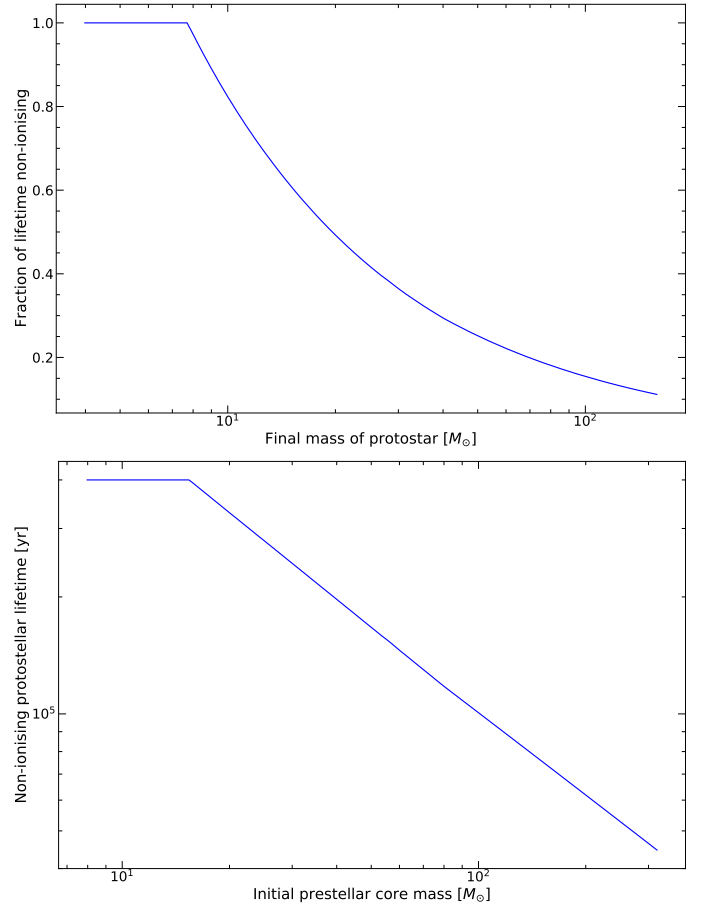


Fig. D.1. **Top:** Fraction of the non-ionising protostellar lifetime as function of the final stellar mass. **Bottom:** Non-Ionising protostellar lifetime as function of the initial prestellar mass reservoir.

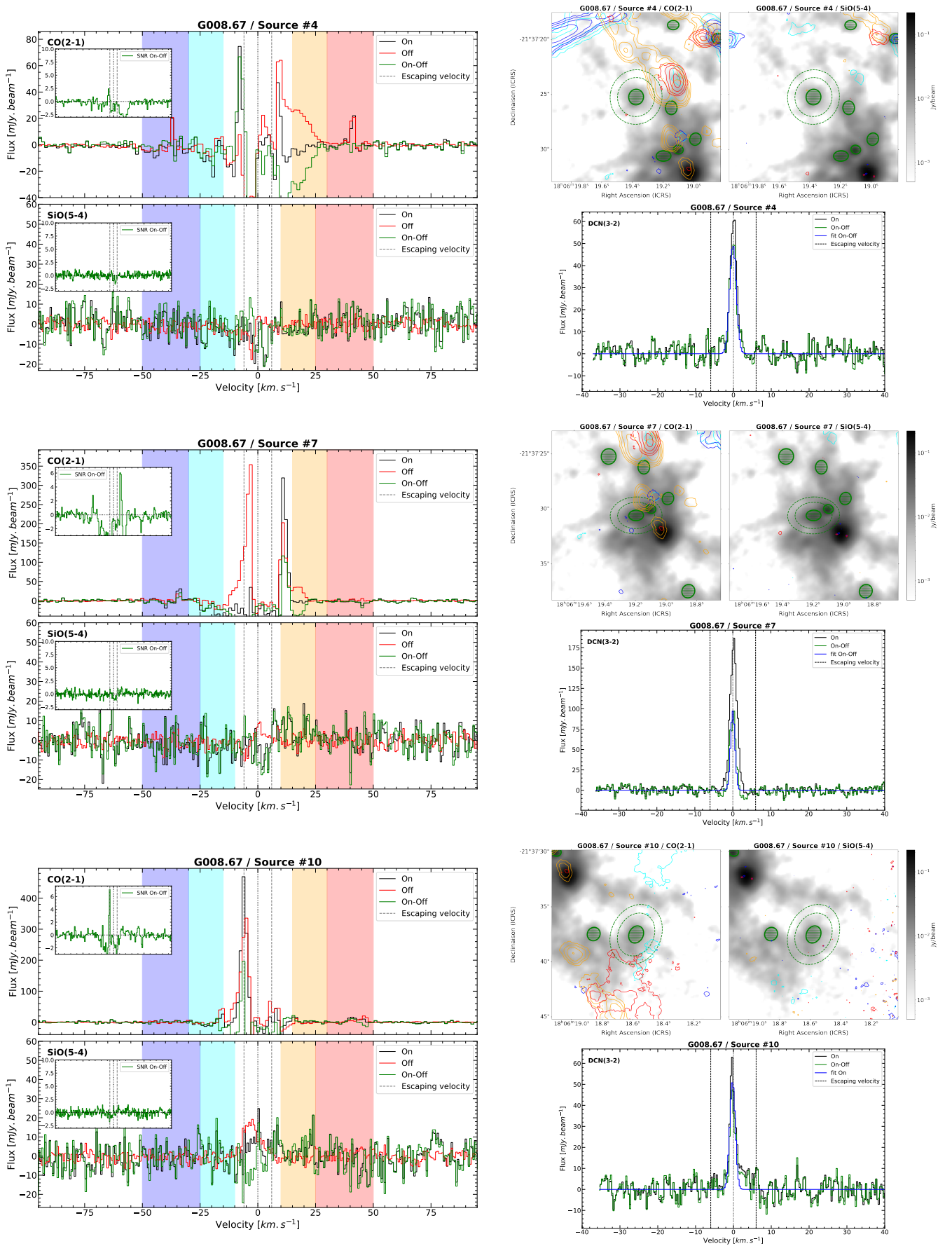


Fig. E.1. CO and SiO spectra (left) and molecular outflow maps (top right) of the high-mass PSC candidates of the G008.67 region. CO contours are 5, 10, 20, and 40 in units of σ , with $\sigma = 39.4, 37.5, 35.0, 38.0$ mJy beam $^{-1}$ km s $^{-1}$ for cyan, blue, orange and red contours respectively. SiO contours are 5, 10, 20, and 40 in units of σ , with $\sigma = 21.7, 27.7, 21.5, 27.3$ mJy beam $^{-1}$ km s $^{-1}$ for cyan, blue, orange and red contours respectively. DCN spectra and fit (bottom right) of the high-mass PSC candidates of the G008.67 region.

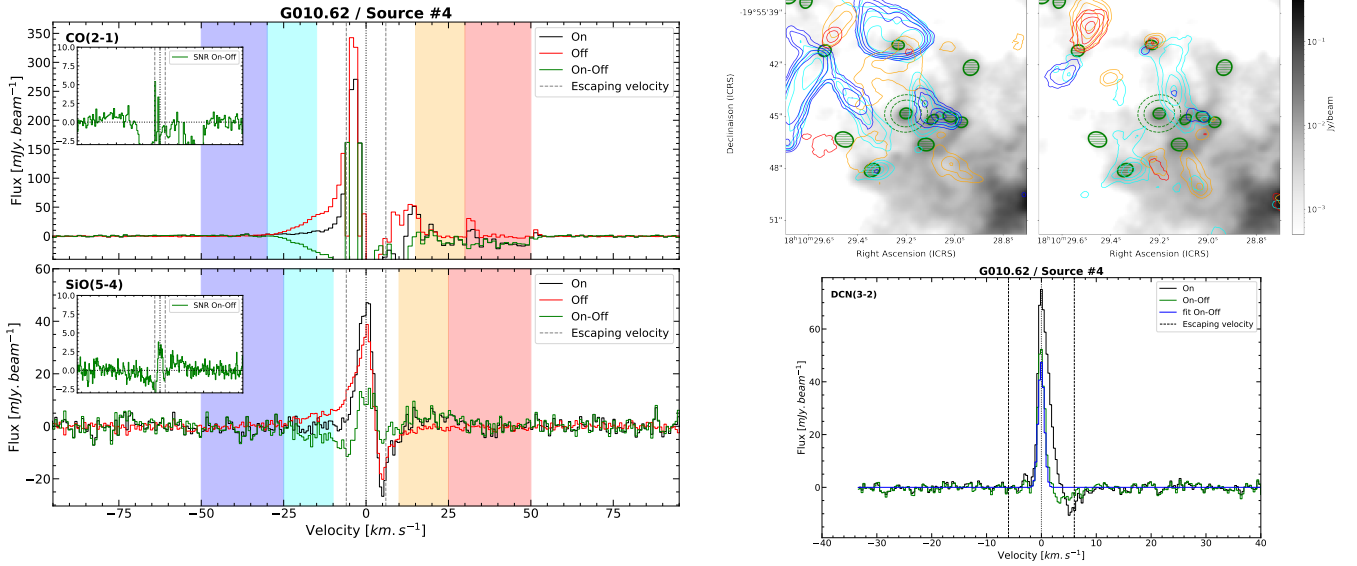


Fig. E.2. CO and SiO spectra and molecular outflow maps of the high-mass PSC candidate of the G010.62 region. CO contours are 10, 20, 40, and 80 in units of σ , with $\sigma = 27.6, 8.6, 20.6, 15.4$ mJy beam $^{-1}$ km s $^{-1}$ for cyan, blue, orange and red contours respectively. SiO contours are 10, 20, 40, and 80 in units of σ , with $\sigma = 5.6, 7.5, 5.4, 7.2$ mJy beam $^{-1}$ km s $^{-1}$ for cyan, blue, orange and red contours respectively. DCN spectra (bottom right) of the high-mass PSC candidate of the G010.62 region.

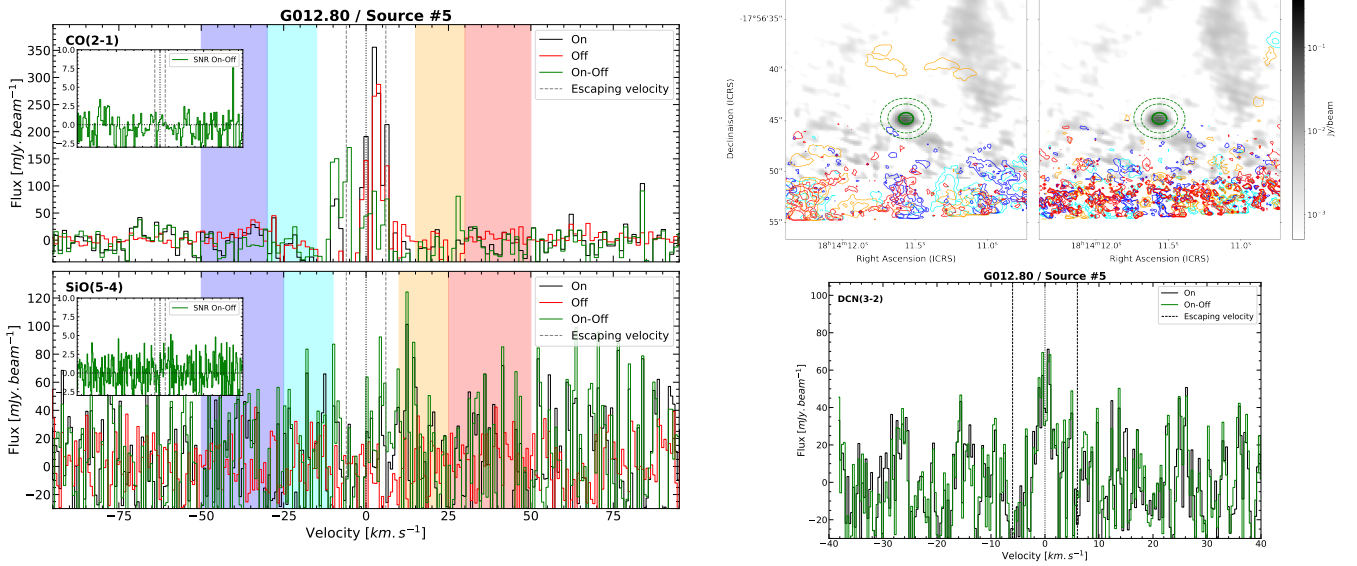


Fig. E.3. CO and SiO spectra and molecular outflow maps of the high-mass PSC candidate of the G012.80 region. CO contours are 10, 20, 40, and 80 in units of σ , with $\sigma = 112.3, 64.1, 126.2, 72.8$ mJy beam $^{-1}$ km s $^{-1}$ for cyan, blue, orange and red contours respectively. SiO contours are 10, 20, 40, and 80 in units of σ , with $\sigma = 26.5, 34.0, 26.2, 33.1$ mJy beam $^{-1}$ km s $^{-1}$ for cyan, blue, orange and red contours respectively. DCN spectra (bottom right) of the high-mass PSC candidate of the G012.80 region.

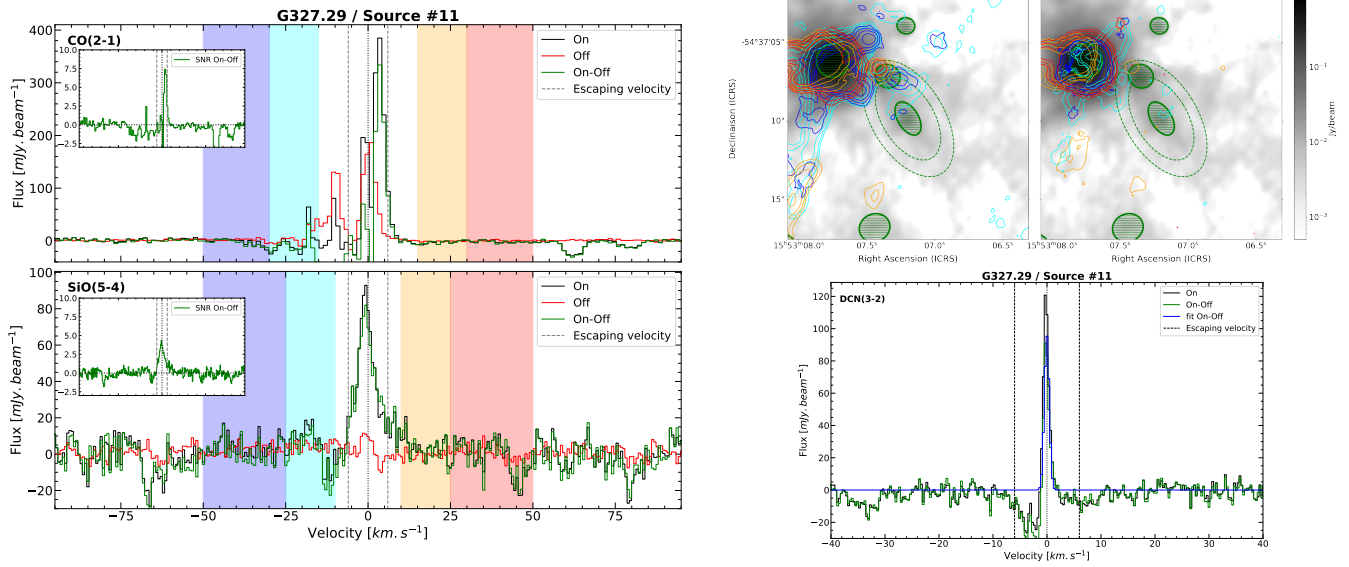


Fig. E.4. CO and SiO spectra (left) and molecular outflow maps (top right) of the high-mass PSC candidates of the G327.29 region. CO contours are 5, 10, 20, and 40 in units of σ , with $\sigma = 48.2, 39.3, 56.1, 37.8$ mJy beam⁻¹ km s⁻¹ for cyan, blue, orange and red contours respectively. SiO contours are 5, 10, 20, and 40 in units of σ , with $\sigma = 35.5, 44.7, 35.7, 45.5$ mJy beam⁻¹ km s⁻¹ for cyan, blue, orange and red contours respectively. DCN spectra and fit (bottom right) of the high-mass PSC candidate of the G327.29 region.

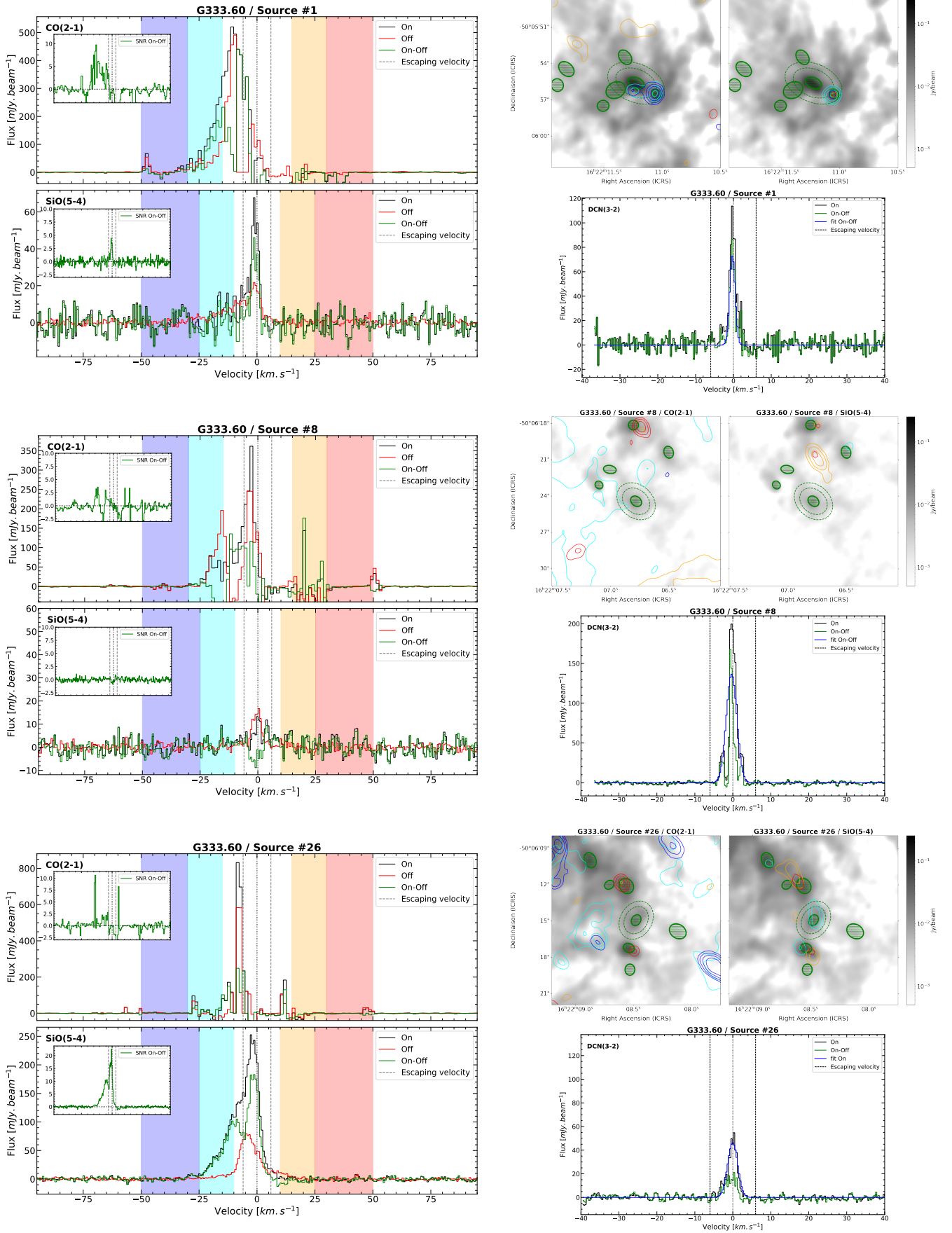


Fig. E.5. CO and SiO spectra (left) and molecular outflow maps (top right) of the high-mass PSC candidates of the G333.60 region. CO contours are 10, 20, 40 and 80 in units of σ , with $\sigma = 110.8, 17.0, 98.6, 20.3$ mJy beam $^{-1}$ km s $^{-1}$ for cyan, blue, orange and red contours respectively. SiO contours are 10, 20, 40 and 80 in units of σ , with $\sigma = 15.8, 20.1, 16.1, 19.8$ mJy beam $^{-1}$ km s $^{-1}$ for cyan, blue, orange and red contours respectively. DCN spectra and fits (bottom right) of the high-mass PSC candidates of the G333.60 region.

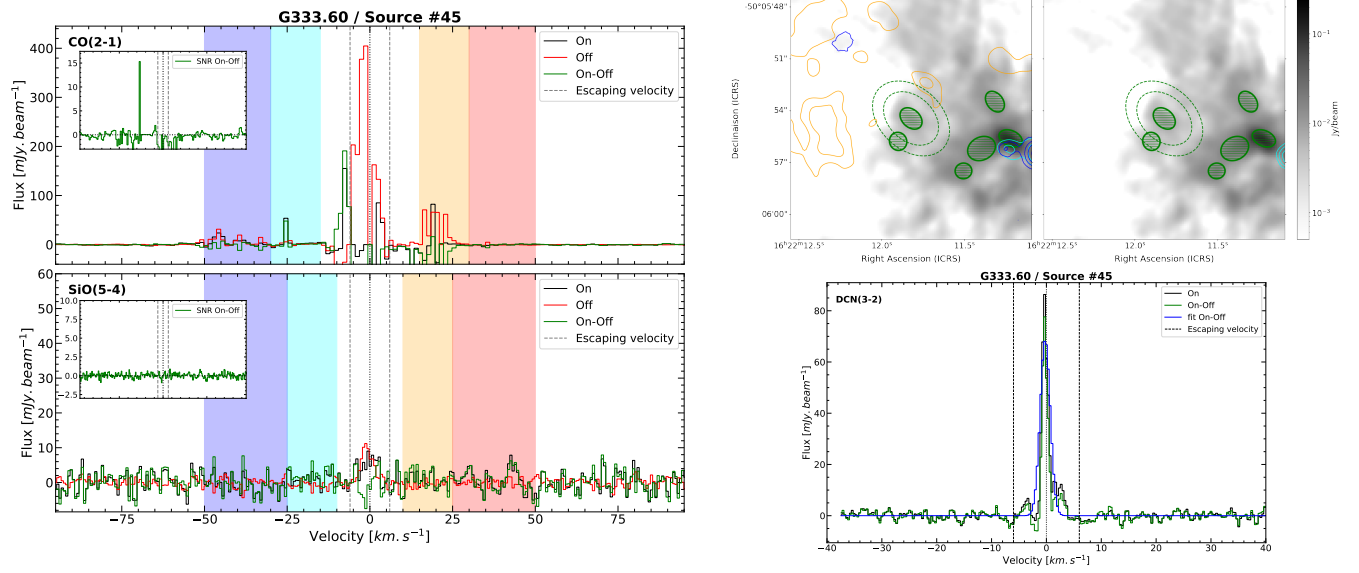


Fig. E.5. continued.

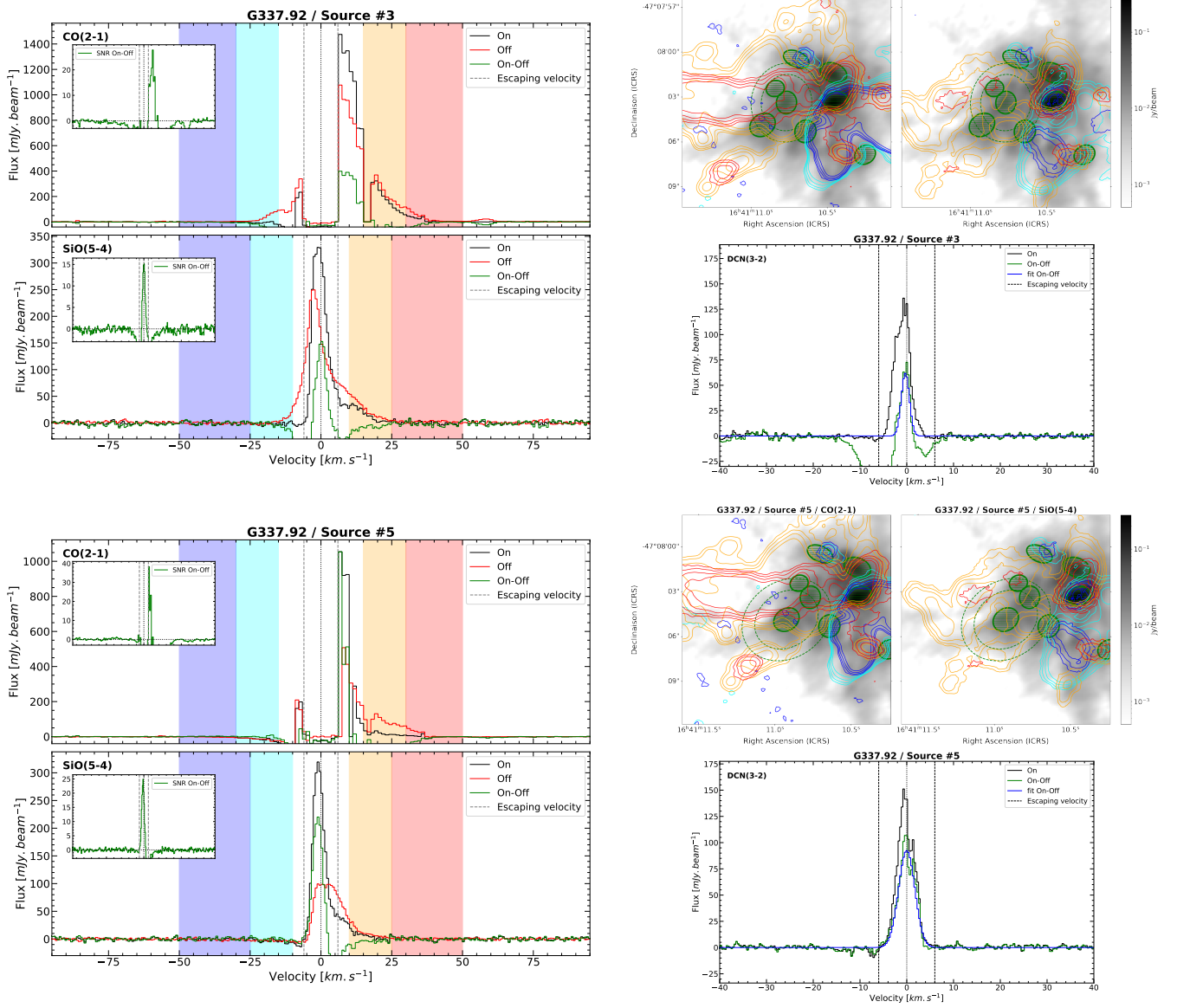


Fig. E.6. CO and SiO spectra (left) and molecular outflow maps (top right) of the high-mass PSC candidates of the G337.92 region. CO contours are 5, 10, 20, and 40 in units of σ , with $\sigma = 38.8, 16.6, 40.3, 24.4$ mJy beam $^{-1}$ km s $^{-1}$ for cyan, blue, orange and red contours respectively. SiO contours are 5, 10, 20, and 40 in units of σ , with $\sigma = 9.4, 12.5, 10.2, 12.2$ mJy beam $^{-1}$ km s $^{-1}$ for cyan, blue, orange and red contours respectively. DCN spectra and fits (bottom right) of the high-mass PSC candidates of the G337.92 region.

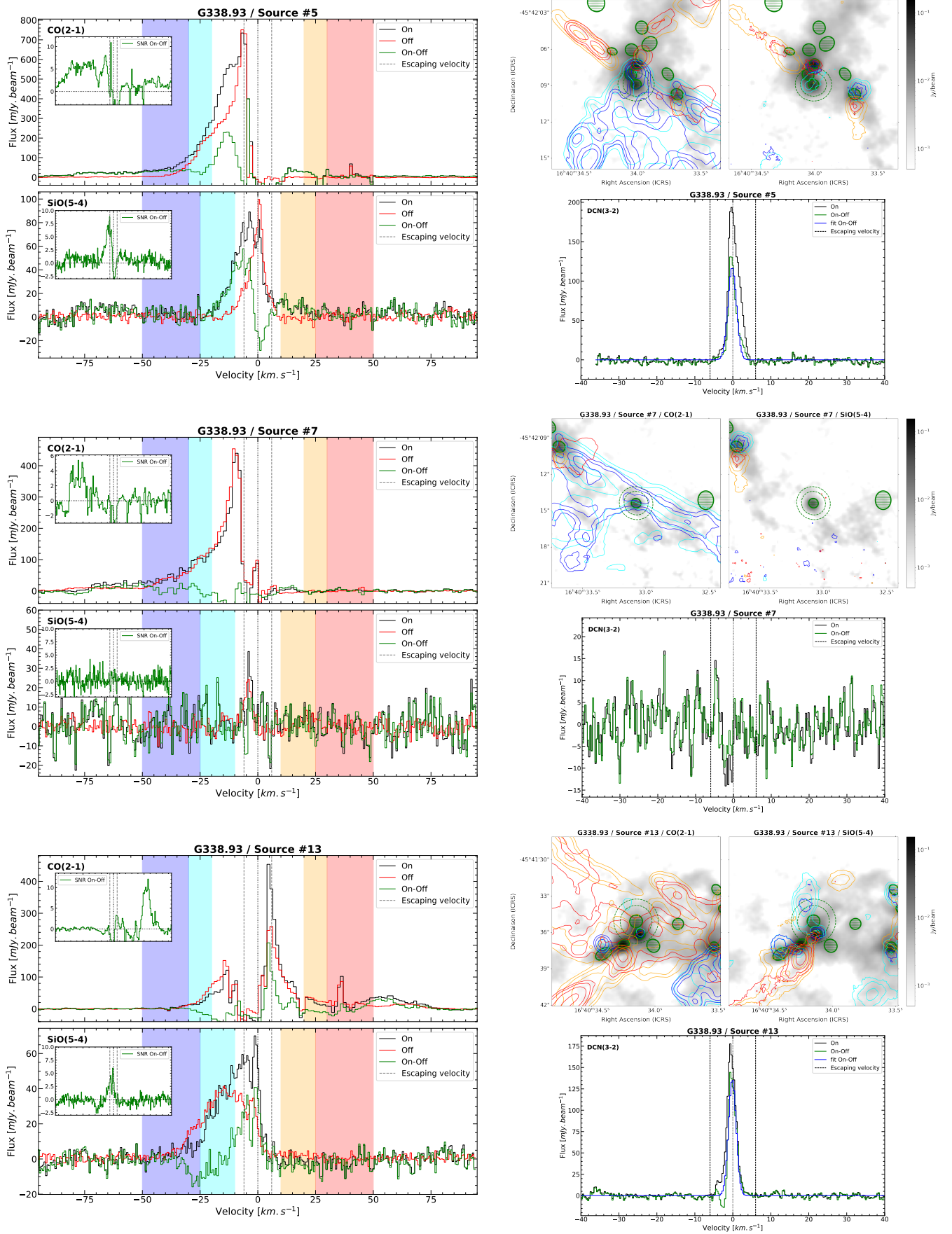


Fig. E.7. CO and SiO spectra (left) and molecular outflow maps (top right) of the high-mass PSC candidates of the G338.93 region. CO contours are 10, 20, 40, and 80 in units of σ , with $\sigma = 69.1, 27.1, 70.0, 27.3$ mJy beam $^{-1}$ km s $^{-1}$ for cyan, blue, orange and red contours respectively. SiO contours are 10, 20, 40, and 80 in units of σ , with $\sigma = 10.3, 12.7, 11.0, 12.5$ mJy beam $^{-1}$ km s $^{-1}$ for cyan, blue, orange and red contours respectively. DCN spectra and fits (bottom right) of the high-mass PSC candidates of the G338.93 region.

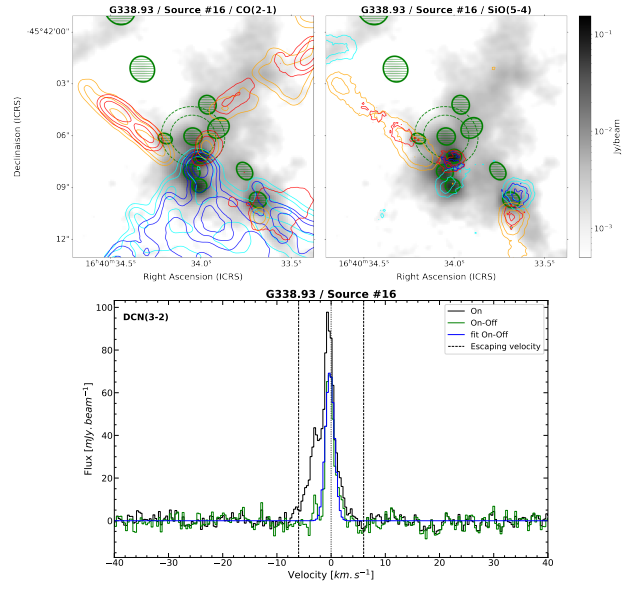
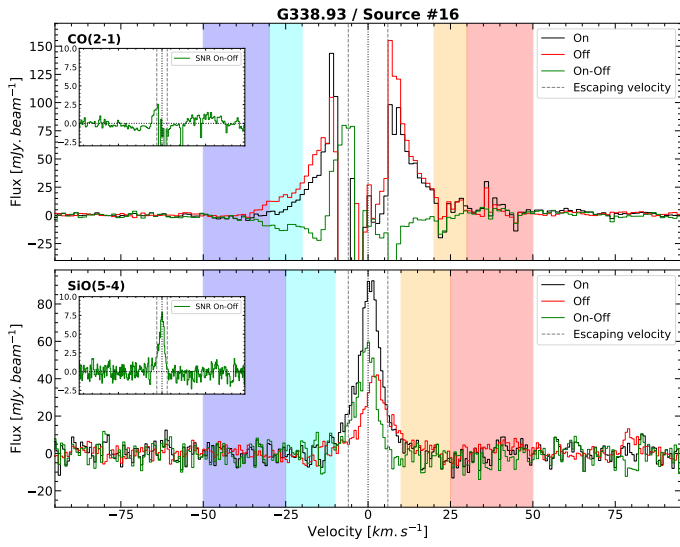


Fig. E.7. continued.

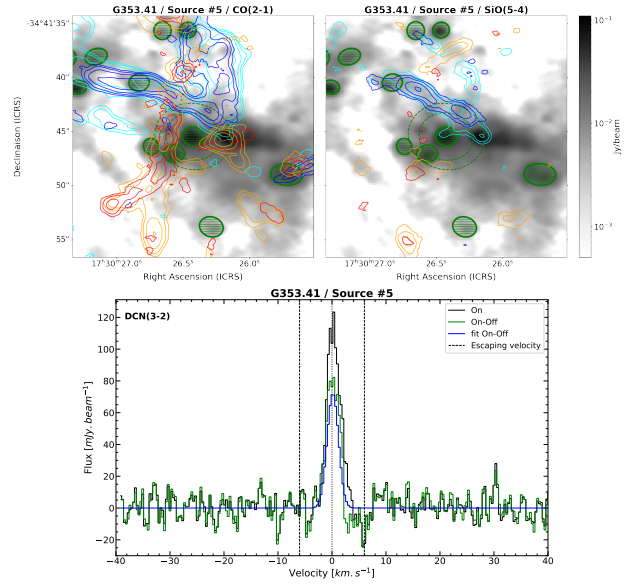
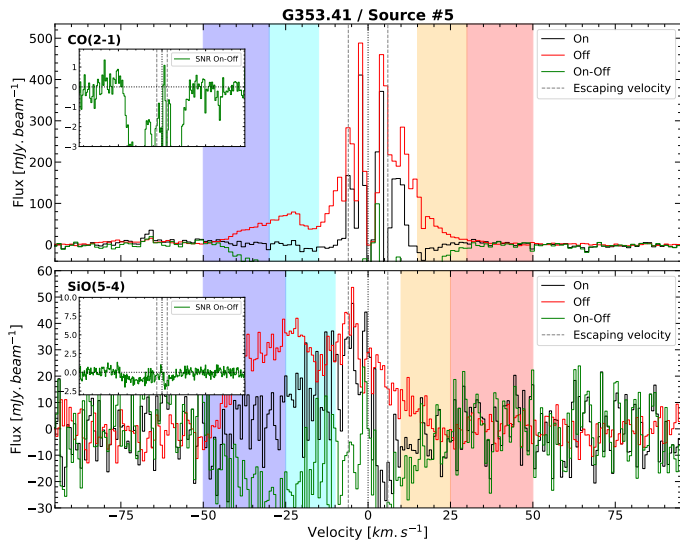


Fig. E.8. CO and SiO spectra (left) and molecular outflow maps (top right) of the high-mass PSC candidate of the G353.41 region. CO contours are 5, 10, 20, and 40 in units of σ , with $\sigma = 95.3, 66.0, 62.9, 64.1$ mJy beam $^{-1}$ km s $^{-1}$ for cyan, blue, orange and red contours respectively. SiO contours are 5, 10, 20, and 40 in units of σ , with $\sigma = 38.5, 49.8, 38.8, 49.1$ mJy beam $^{-1}$ km s $^{-1}$ for cyan, blue, orange and red contours respectively. DCN spectra and fit (bottom right) of the high-mass PSC candidate of the G353.41 region.

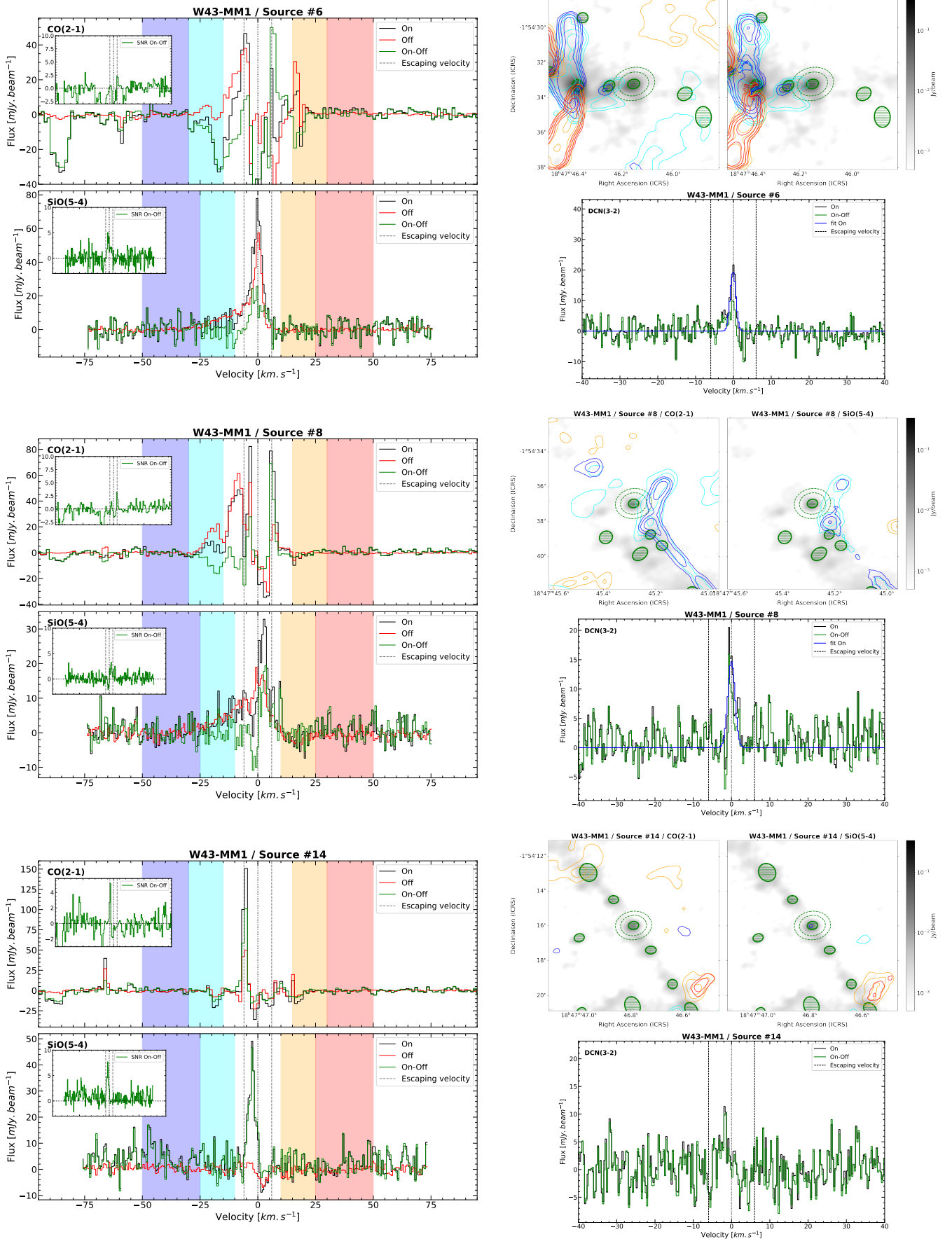


Fig. E.9. CO and SiO spectra (left) and molecular outflow maps (top right) of the high-mass PSC candidates of the W43-MM1 region. CO contours are 10, 20, 40, and 80 in units of σ , with $\sigma = 32.6, 18.6, 49.5, 15.3 \text{ mJy beam}^{-1} \text{ km s}^{-1}$ for cyan, blue, orange and red contours respectively. SiO contours are 10, 20, 40, and 80 in units of σ , with $\sigma = 6.4, 7.4, 7.3, 7.2 \text{ mJy beam}^{-1} \text{ km s}^{-1}$ for cyan, blue, orange and red contours respectively. DCN spectra and fits (bottom right) of the high-mass PSC candidates of the W43-MM1 region.

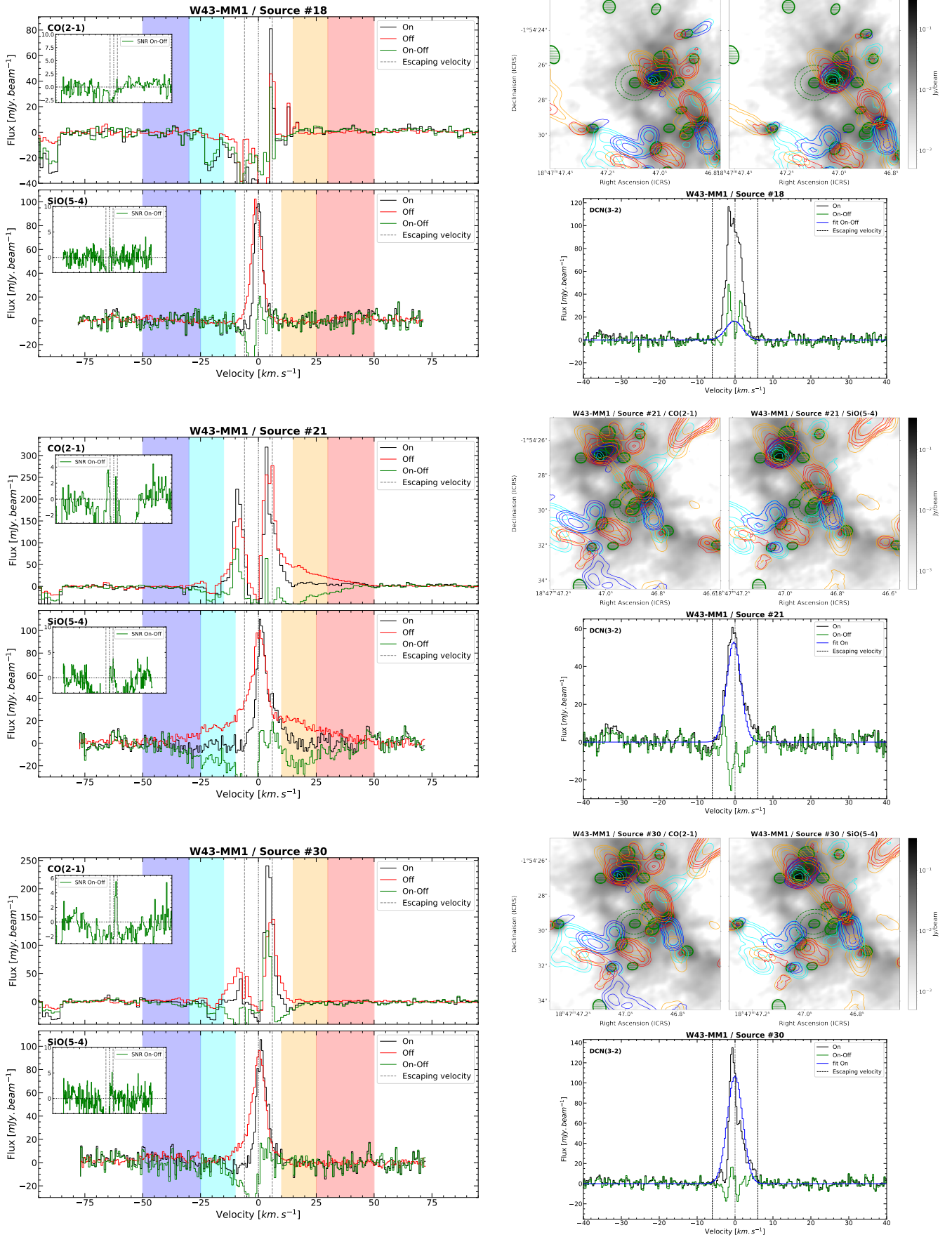


Fig. E.9. continued.

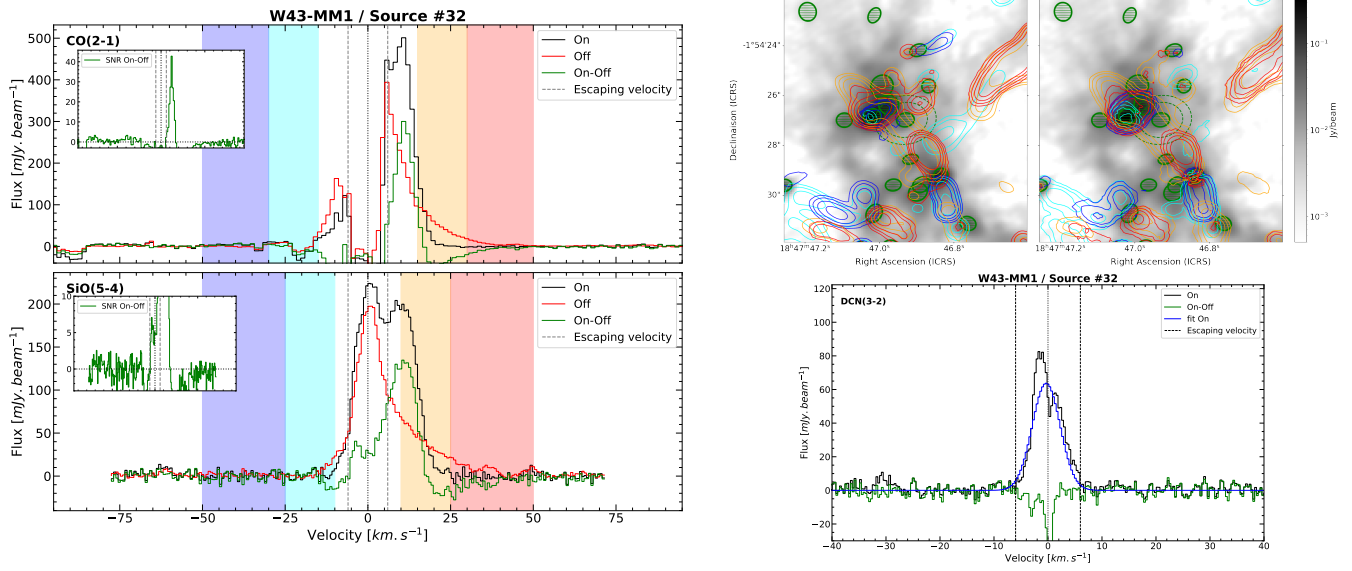


Fig. E.9. continued.

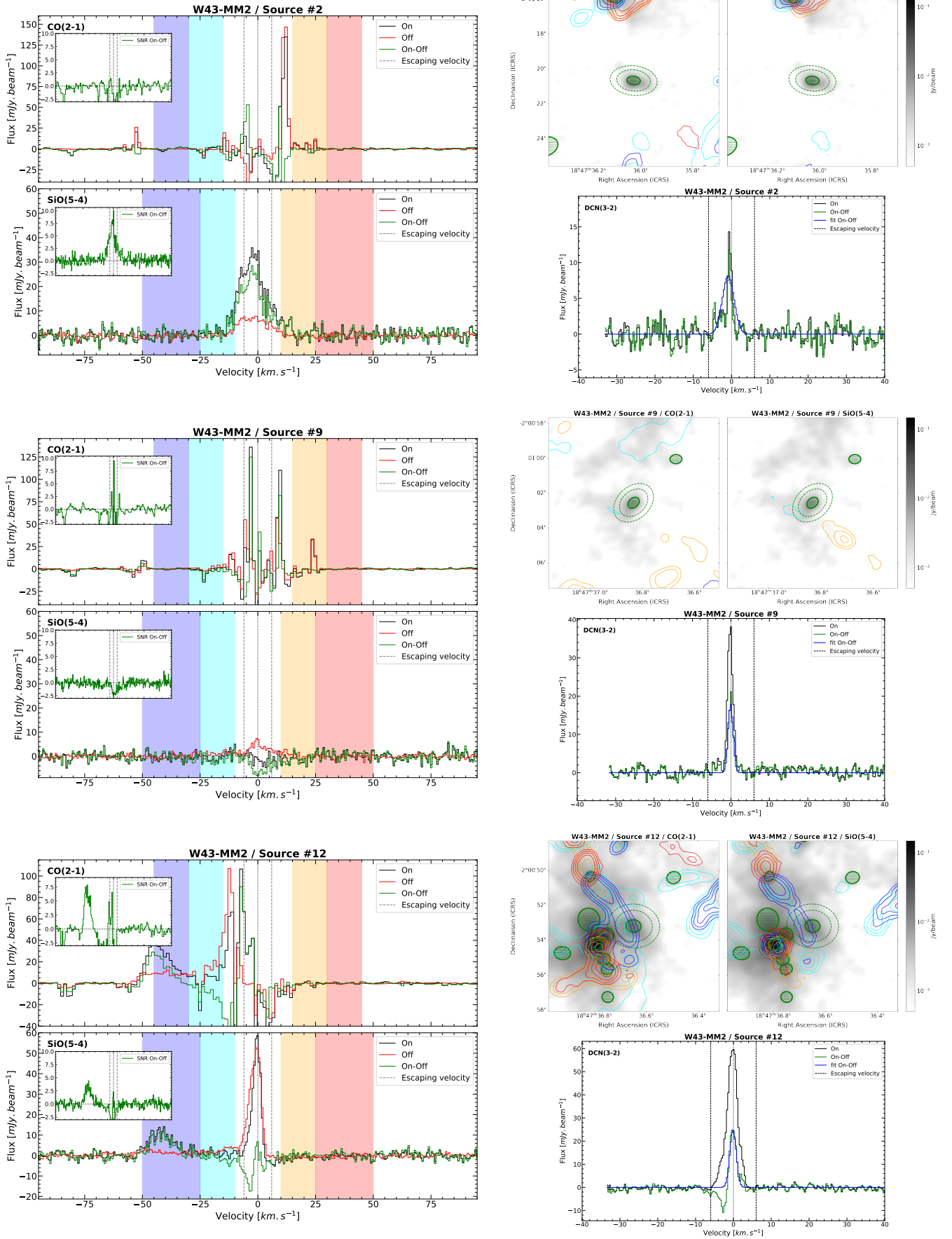


Fig. E.10. CO and SiO spectra (left) and molecular outflow maps (top right) of the high-mass PSC candidates of the W43-MM2 region. CO contours are 10, 20, 40, and 80 in units of σ , with $\sigma = 18.9, 11.0, 6.4$ mJy beam⁻¹ km s⁻¹ for cyan, blue, orange and red contours respectively. SiO contours are 10, 20, 40, and 80 in units of σ , with $\sigma = 4.4, 5.7, 4.5, 5.7$ mJy beam⁻¹ km s⁻¹ for cyan, blue, orange and red contours respectively. DCM spectra and fits (bottom right) of the high-mass PSC candidates of the W43-MM2 region.

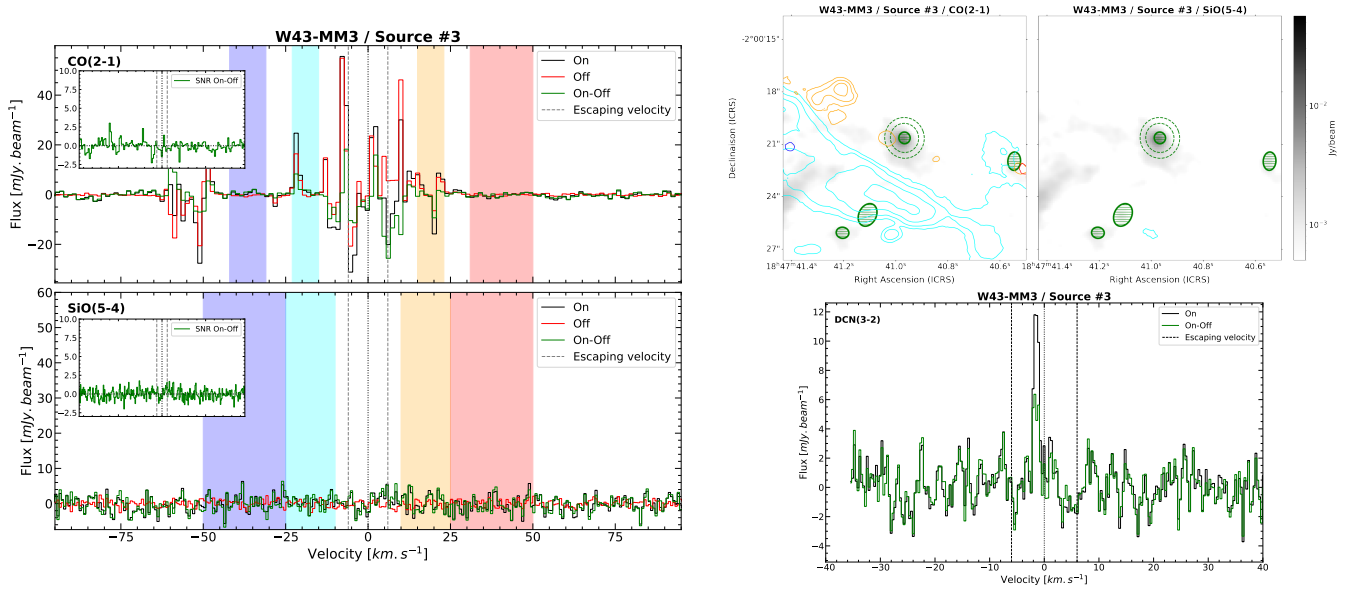


Fig. E.11. CO and SiO spectra (left) and molecular outflow maps (top right) of the high-mass PSC candidate of the W43-MM3 region. CO contours are 5, 10, 20, and 40 in units of σ , with $\sigma = 14.3, 12.6, 10.8, 9.0$ mJy beam $^{-1}$ km s $^{-1}$ for cyan, blue, orange and red contours respectively. SiO contours are 5, 10, 20, and 40 in units of σ , with $\sigma = 5.7, 7.2, 5.5, 7.2$ mJy beam $^{-1}$ km s $^{-1}$ for cyan, blue, orange and red contours respectively. DCN spectra and fit (bottom right) of the high-mass PSC candidate of the W43-MM3 region.

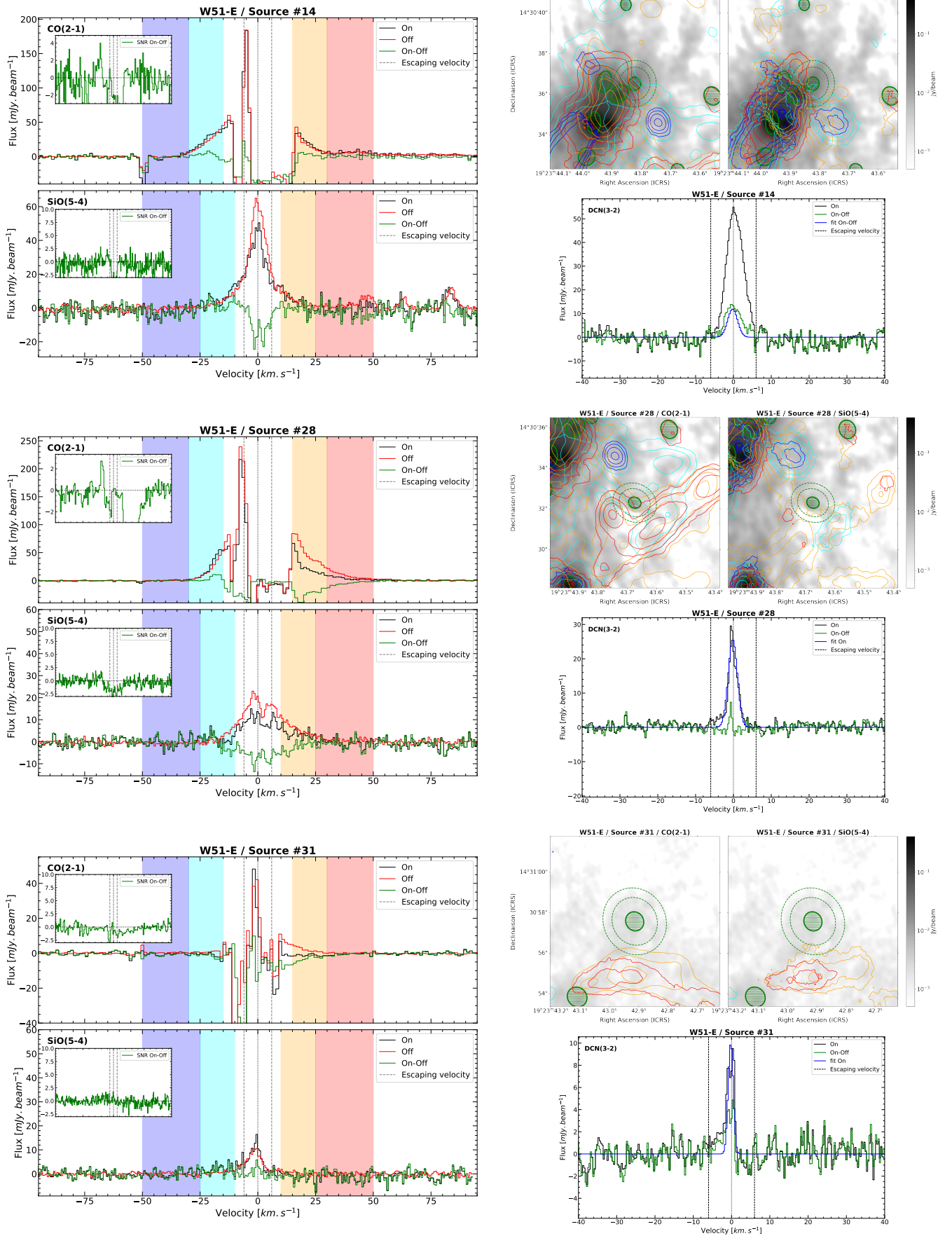


Fig. E.12. CO and SiO spectra (left) and molecular outflow maps (top right) of the high-mass PSC candidates of the W51-E region. CO contours are 10, 20, 40 and 80 in units of σ , with $\sigma = 13.3, 7.5, 25.7, 10.2 \text{ mJy beam}^{-1} \text{ km s}^{-1}$ for cyan, blue, orange and red contours respectively. SiO contours are 10, 20, 40 and 80 in units of σ , with $\sigma = 4.7, 6.1, 4.6, 6.0 \text{ mJy beam}^{-1} \text{ km s}^{-1}$ for cyan, blue, orange and red contours respectively. DCN spectra and fits (bottom right) of the high-mass PSC candidates of the W51-IRS2 region.

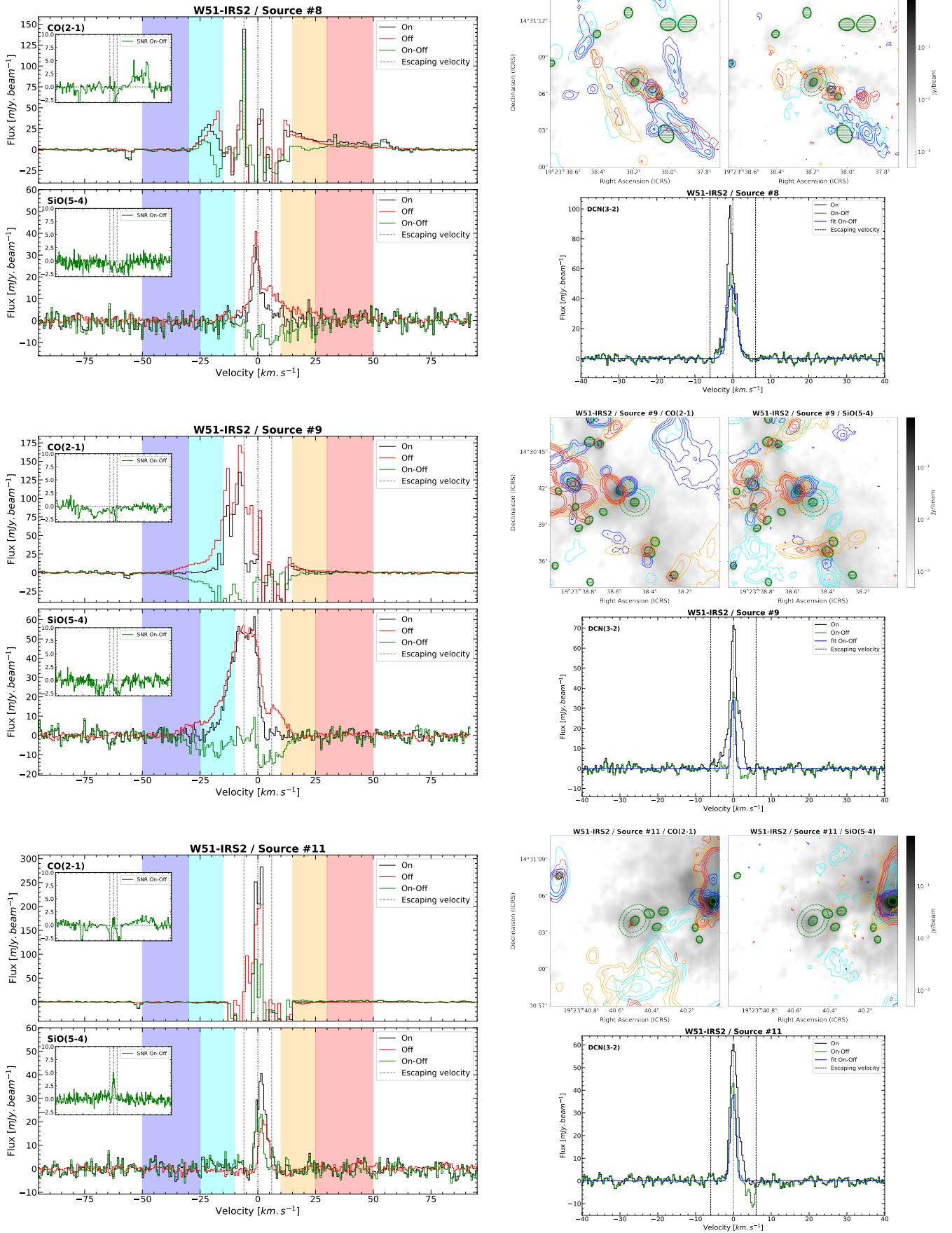


Fig. E.13. CO and SiO spectra (left) and molecular outflow maps (top right) of the high-mass PSC candidates of the W51-IRS2 region. CO contours are 5, 10, 20, and 40 in units of σ , with $\sigma = 105.5, 13.8, 44.8, 13.2$ mJy beam⁻¹ km s⁻¹ for cyan, blue, orange and red contours respectively. SiO contours are 5, 10, 20, and 40 in units of σ , with $\sigma = 5.9, 7.4, 6.2, 7.5$ mJy beam⁻¹ km s⁻¹ for cyan, blue, orange and red contours respectively. DCN spectra and fits (bottom right) of the high-mass PSC candidates of the W51-IRS2 region.

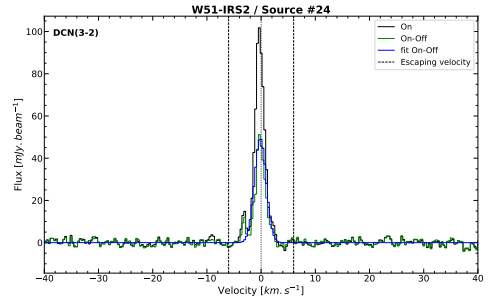
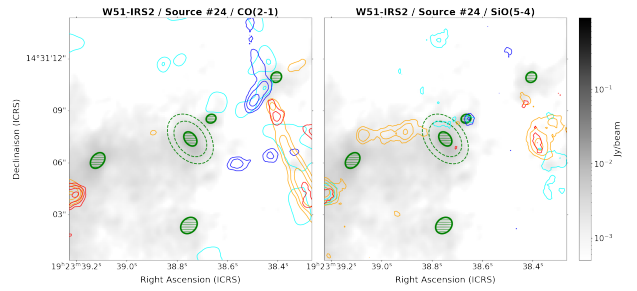
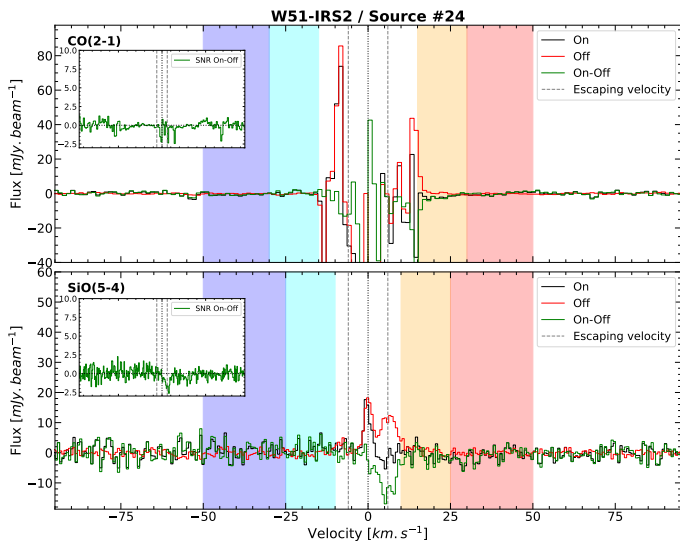
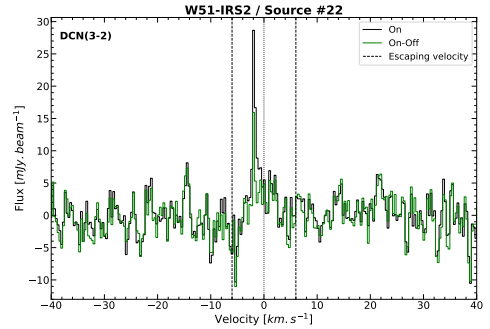
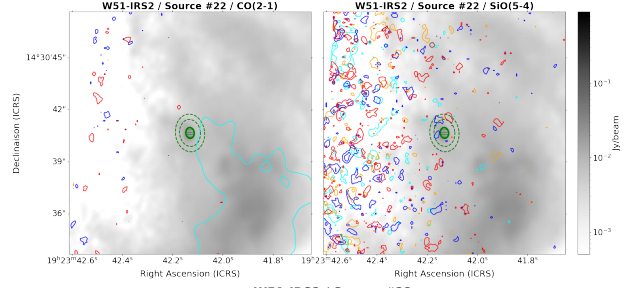
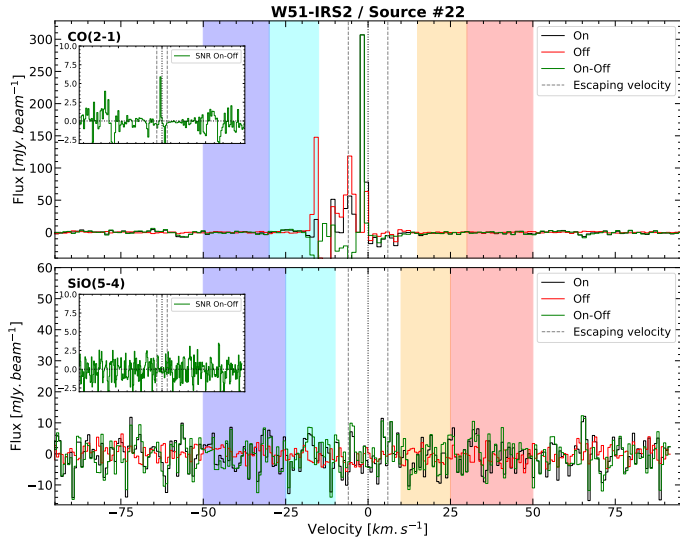
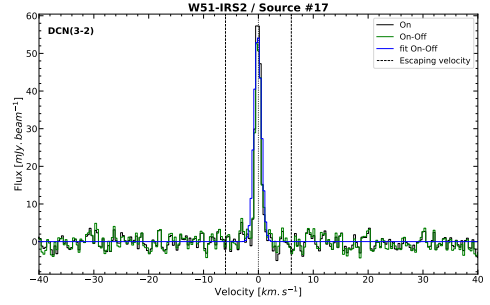
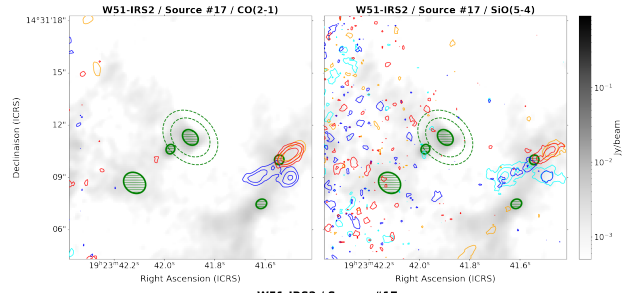
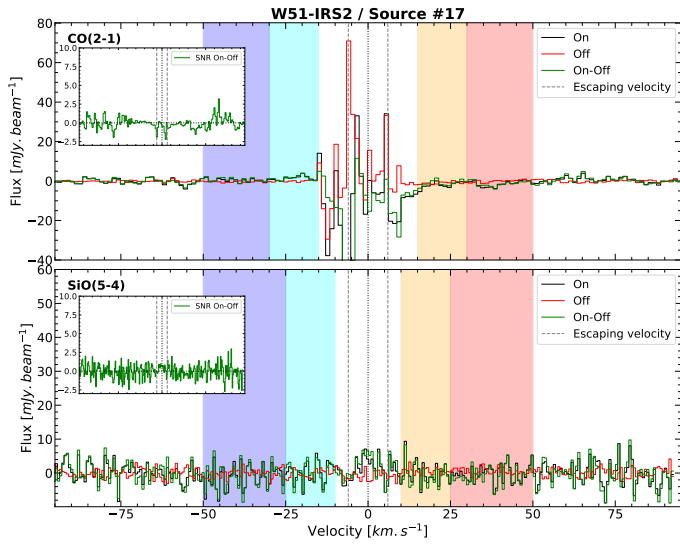


Fig. E.13. continued.

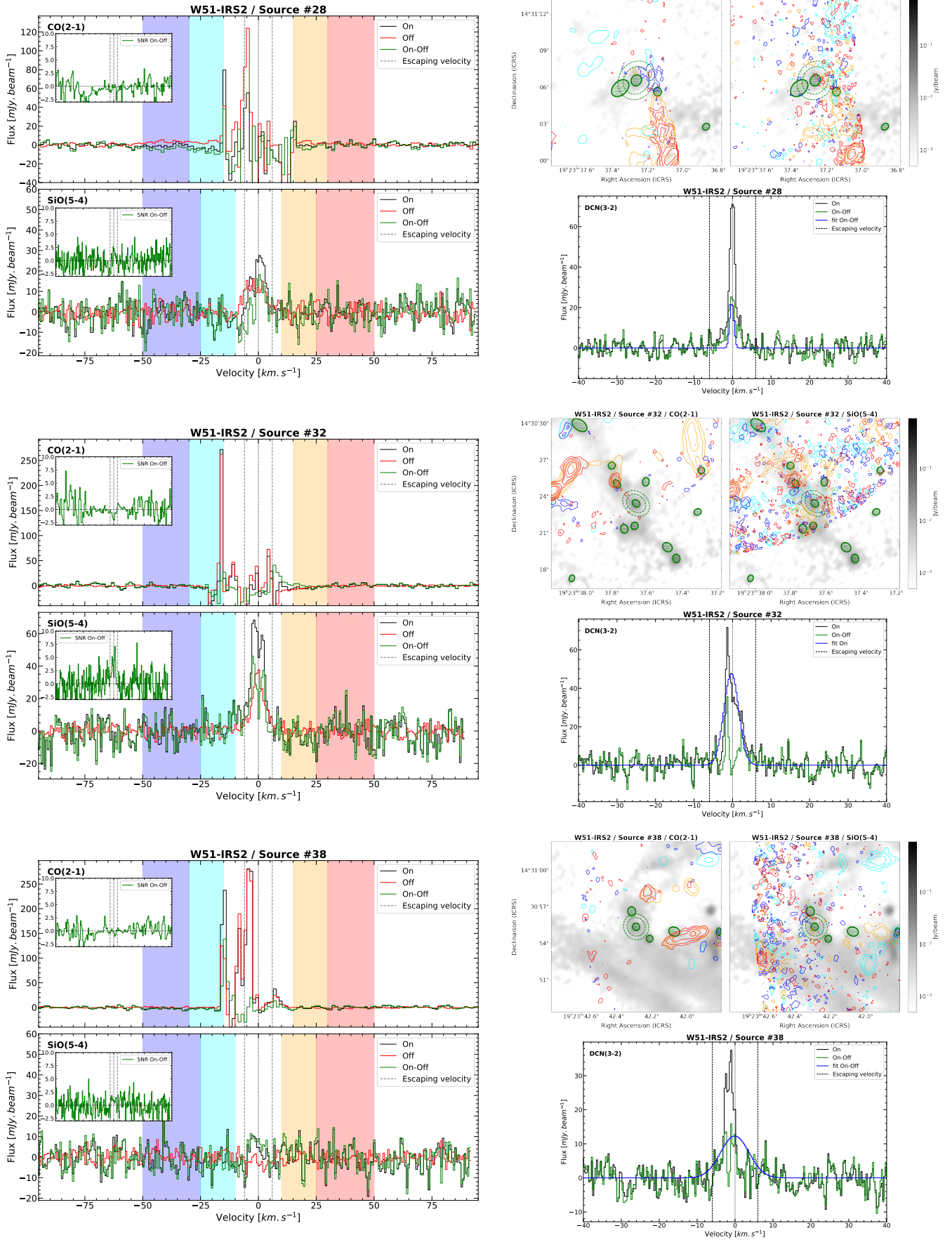


Fig. E.13. continued.

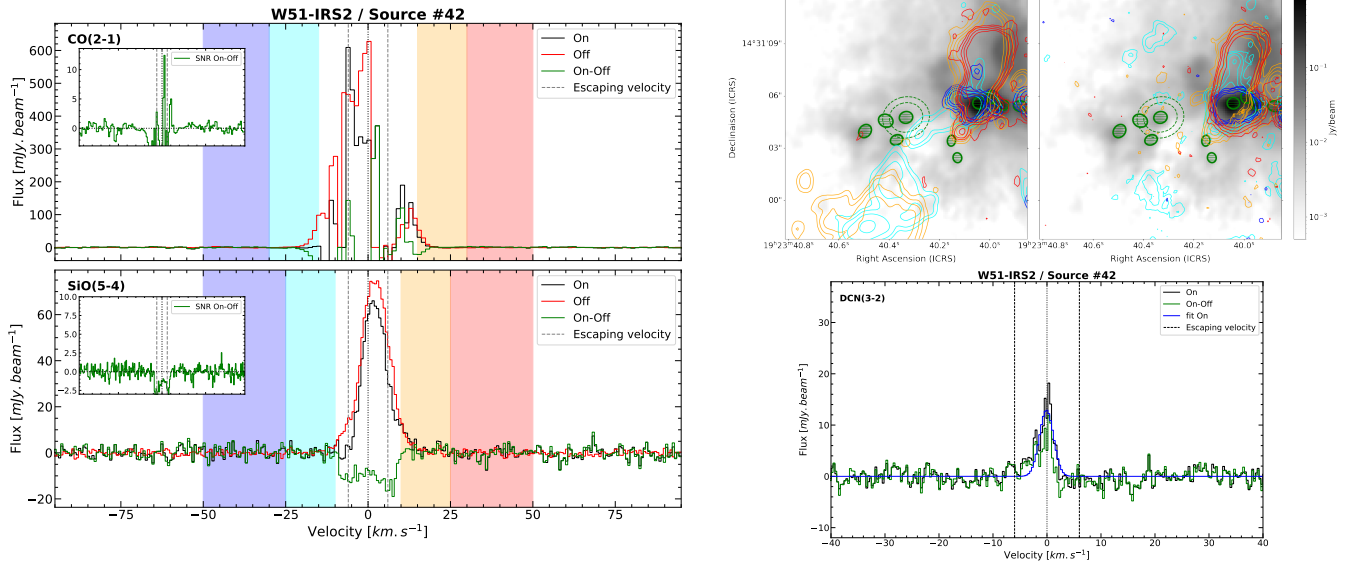


Fig. E.13. continued.

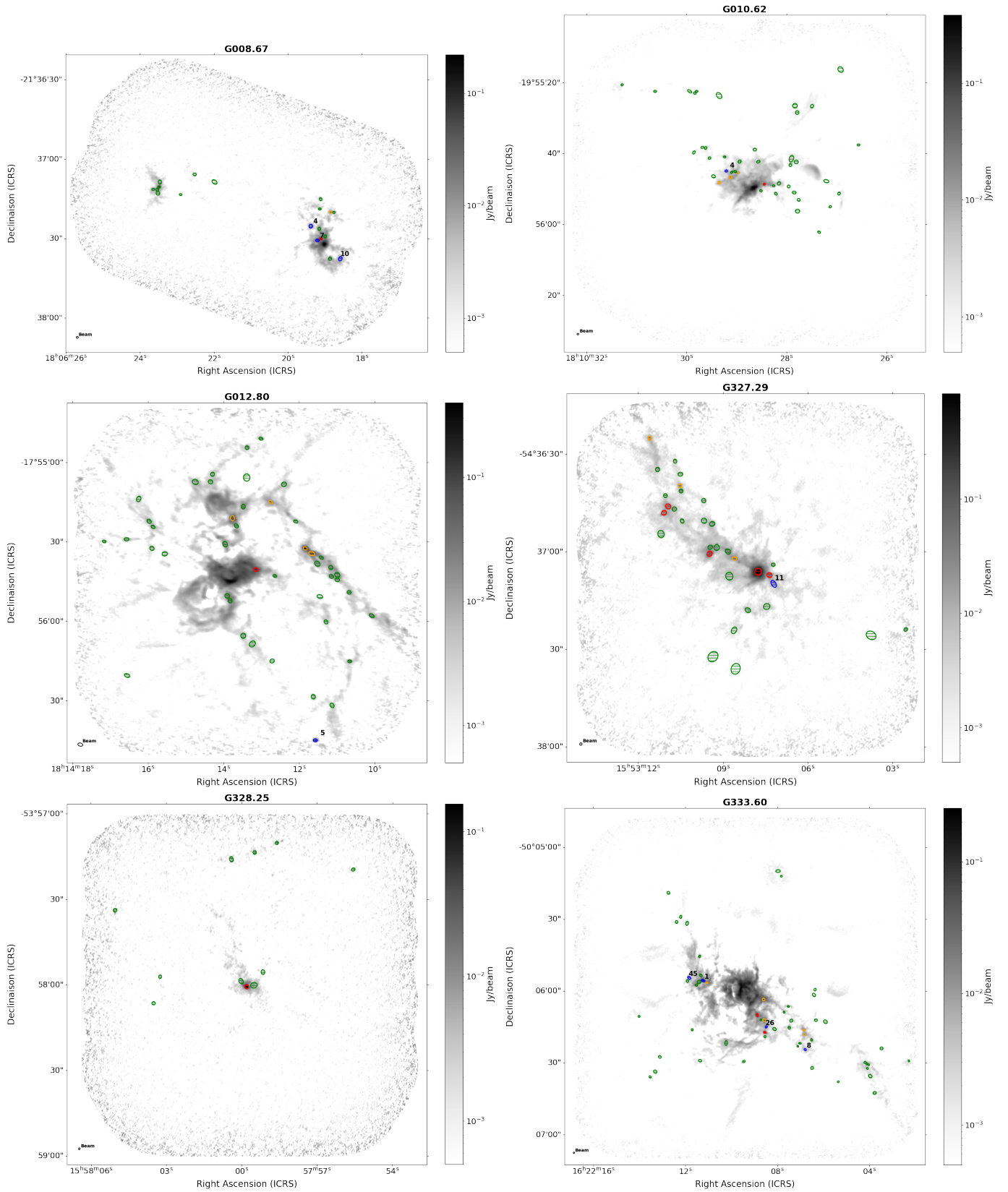


Fig. F.1. Locations of the high-mass PSC candidates in the ALMA-IMF regions. The candidates are the blue ellipses annotated with their number. The red cores are the high-mass protostellar cores ($M > 8 M_{\odot}$) and the orange ones are the intermediate mass protostellar cores ($4 M_{\odot} < M < 8 M_{\odot}$). The other cores are the green ellipses which are non studied cores.

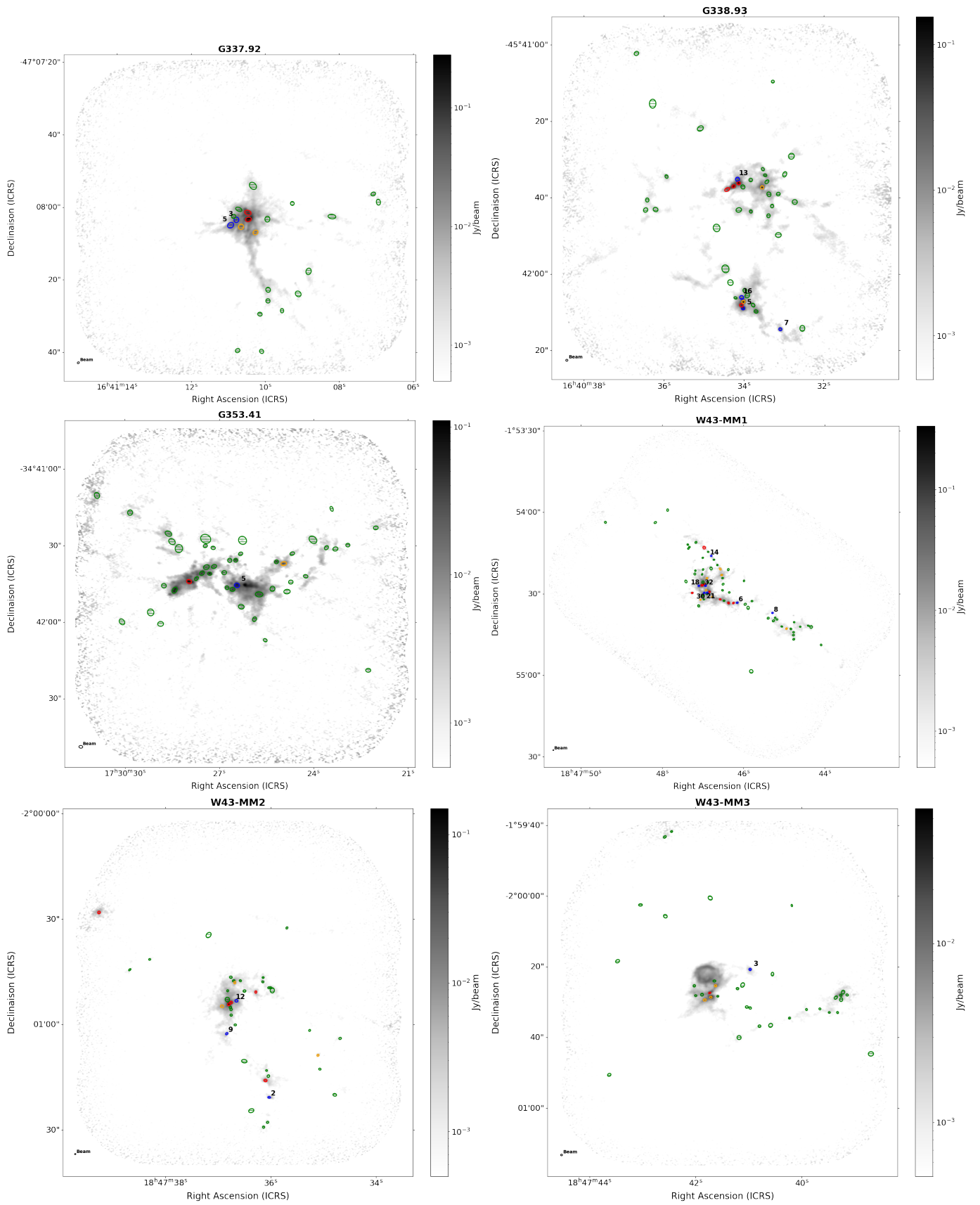


Fig. F.1. continued.

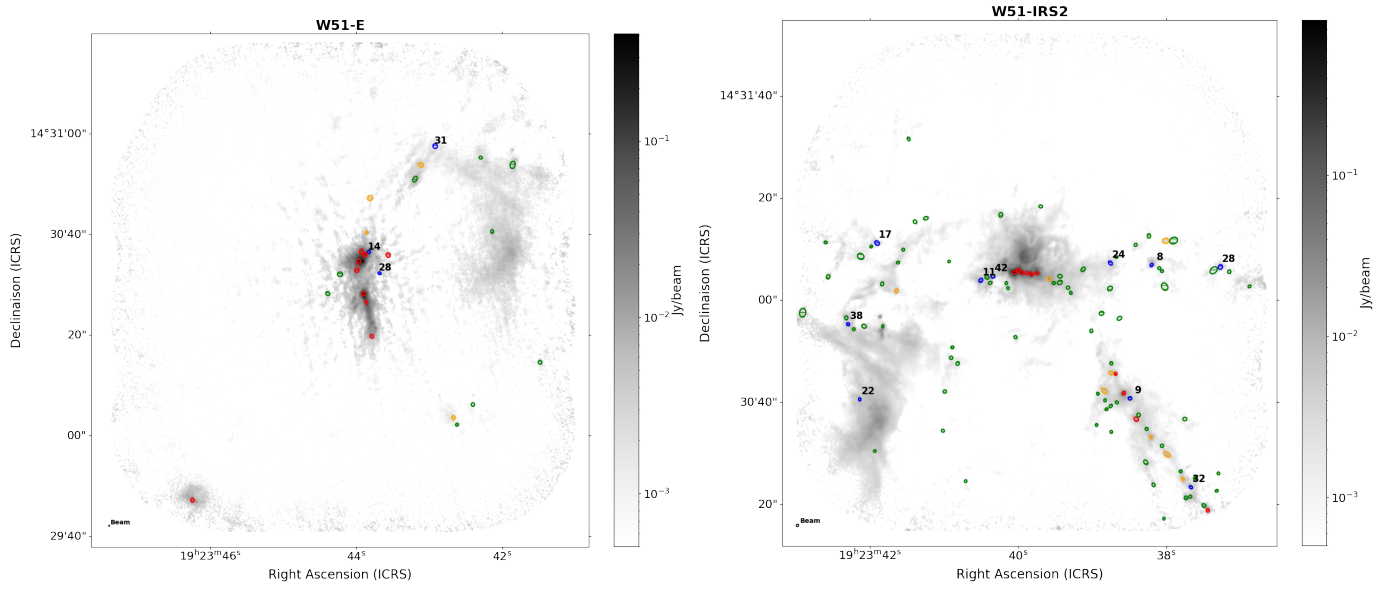


Fig. F.1. continued.